

8-1-2003

DENSE WAVELENGTH DIVISION MULTIPLEXING/DEMULTIPLEXING BY THE METHOD OF IRREGULARLY SAMPLED ZERO CROSSINGS

Ying Lu

Okan K. Ersoy

Follow this and additional works at: <http://docs.lib.purdue.edu/ecetr>

Lu, Ying and Ersoy, Okan K., "DENSE WAVELENGTH DIVISION MULTIPLEXING/DEMULTIPLEXING BY THE METHOD OF IRREGULARLY SAMPLED ZERO CROSSINGS" (2003). *ECE Technical Reports*. Paper 154.
<http://docs.lib.purdue.edu/ecetr/154>

This document has been made available through Purdue e-Pubs, a service of the Purdue University Libraries. Please contact epubs@purdue.edu for additional information.

DENSE WAVELENGTH DIVISION
MULTIPLEXING / DEMULTIPLEXING
BY THE METHOD OF IRREGULARLY
SAMPLED ZERO CROSSING

YING LU
OKAN ERSOY

TR-ECE 03-12
AUGUST 2003

PURDUE

UNIVERSITY

SCHOOL OF ELECTRICAL
AND COMPUTER ENGINEERING
PURDUE UNIVERSITY
WEST LAFAYETTE, IN 47907-2035

**DENSE WAVELENGTH DIVISION
MULTIPLEXING/DEMULTIPLEXING BY THE
METHOD OF IRREGULARLY SAMPLED ZERO
CROSSINGS**

Ying Lu

Okan Ersoy

Purdue University

School of Electrical and Computer Engineering

August 2003

TABLE OF CONTENTS

	Page
LIST OF TABLES.....	iv
LIST OF FIGURES.....	v
ABSTRACT.....	x
1 LITERATURE REVIEW.....	1
1.1 Background in WDM Communication Networks.....	1
1.2 Wavelength Demultiplexing In WDM Networks.....	1
1.3 Implementation of Wavelength Demultiplexers.....	2
1.4 Wavelength Demultiplexing Using MISZC	6
1.4.1 A brief description of the method of Irregularly Sampled Zero Crossings.....	6
1.4.2 Applying MISZC to AWG structure.....	7
1.5 Orgnization of the Dissertation	7
2 WAVE OPTICS MODELING OF AWE DEVICES.....	11
2.1 Introduction to Operation of Regular AWG.....	11
2.2 Scalar Wave Based AWG Simulation.....	17
2.2.1 Linear system formulation.....	18
2.2.2 Application to ISZC AWG simulation.....	21
2.2.3 Simulaiton results.....	22
2.3 Discussion.....	24
3 METHOD OF IRREGULARLY SAMPLED ZERO CROSSINGS FOR WAVELENGTH DEMULTIPLEXING.....	35
3.1 Holography Basics.....	36
3.2 One-Image-Only Holography.....	37
3.3 The Dispersion Relation for Zero Crossing Phased Array Wavelength Demultiplexing.....	39
3.4 A Practical Algorithm for the Irregularly Sampled Zero Crossing Phased Array Wavelength Demultiplexing.....	44
2.4.1 Design algorithm.....	44

2.4.2 Calculation of the coordinates for sampling points.....	45
2.5 Elimination of High Order Harmonic Diffractions.....	46
2.5.1 Eliminating high order diffractions by zero crossing sampling.....	47

	Page
2.5.2 Eliminating high order diffractions by irregular sampling.....	48
2.6 Simulation Results.....	53
2.6.1 Image formation.....	53
2.6.2 Zero crossing dispersion relation.....	54
2.6.3 Output intensity in harmonics for irregular spaced phased array.....	54
4 IMPLEMENTATION OF ISZC PHASED ARRAY USING BEAMPROP AWG UTILITY BY RSOFT.....	66
4.1 Waveguide Implementation of ISZC Phased Array Wavelength Demultiplexing.....	66
4.1.1 Overview and motivation for waveguide implementation.....	66
4.1.2 The modification of regular AWG.....	68
4.2 ISZC Modified AWG Layout and Simulation Using BeamPROP.....	70
4.2.1 Overview of regular and ISZC modified AWG layout and simulation	70
4.2.2 Layout design for regular AWG.....	72
4.2.3 Adopting regular AWG layout design to ISZC based AWG.....	73
4.2.4 A Note on PHASCORE.EXE.....	74
4.3 Discussion of BPM Methods.....	75
4.3.1 General BPM.....	76
4.3.2 Finite difference based BPM.....	78
4.3.3 Wide angle extension to FD-BPM.....	79
4.3.4 Vectorial extension of FD-BPM.....	81
4.4 Simulation Results.....	82
4.4.1 Interpretation of simulation results.....	82
4.4.2 Simulation results for 200 channel ISZC AWG.....	83
4.4.3 Conclusions.....	85
5 ISZC AWG NOISE AND CHANNEL CAPACITY CONSIDERATIONS.....	104
5.1 Noise Considerations.....	105
5.2 Channel Capacity Consideration.....	111
5.3 Conclusions.....	113

6 CONCLUSIONS AND FUTURE RESEAECH.....	123
6.1 The Need for Large Channel Count Wavelength Demultiplexers.....	123
6.2 Research Summary.....	124
6.3 Future Research.....	126

REFERENCES.....	128
APPENDIX AN EXAMPLE OF AN ISZC AWG LAYOUT.....	133

LIST OF TABLES

Table	Page
3.1: Percentage difference of x-axis focal point deviation at selected wavelengths	61
3.2: Intensity variation between designed focal point and simulation results	61
3.3: Comparison of dispersion factor :simulation vs. theory for fixed θ and fixed z_0	66
4.1: An example of Design Info File used to correct PHASCORE.EXE	76
4.2: The first few terms of Pade expansion [12]	81

LIST OF FIGURES

Figure	Page
1.1: Evolution of optical networks.....	9
1.2: Essentials of an AWG demultiplexer.....	10
1.3: System theory interpretation of the AWG structure.....	10
2.1.a: An illustration of the AWG demultiplexer.....	27
2.1.b: Illustration of AWG demultiplexer parameters [11].....	27
2.1.c: Enlarged view of the output coupler [8].....	28
2.2: FSR of a regular AWG: the output coupler is shown with $D=20\text{ }\mu\text{m}$, $\Delta=1.6\text{nm}$	29
2.3.a: A diagram of input coupler and arrayed waveguides.....	30
2.3.b: The output coupler input-output diagram.....	30
2.4.a: Obtaining the transmission spectrum of an AWG.....	31
2.4.b: An example of an AWG transmission spectrum [38].....	31
2.5: The AWG output dispersion as a function of wavelength separation ($m=100$)..	32
2.6: The AWG output dispersion as a function of wavelength separation ($m=60$)..	32
2.7: The transmission spectrum of a 36-channel-0.5nm spacing regular AWG...	33
2.8.a: The transmission spectrum of a 48-channel-0.4nm spacing ISZC AWG...	33
2.8.b: The transmission spectrum of a 72-channel-0.2nm spacing ISZC AWG...	34

2.8.c: The transmission spectrum of a 96-channel-0.2nm spacing ISZC AWG...	34
--	----

2.9: Diagram of the confocal geometry.....	35
--	----

Figure	Page
--------	------

2.10: Spatial and frequency domain conversion in the output coupler.....	35
--	----

3.1: Geometry of one-image-only digital holography with spherical reference wave	57
---	----

3.2.a: Zero crossing phased array wavelength demultiplexing.....	57
--	----

3.2.b: Zero crossing phased array wavelength demultiplexing with virtue spherical reference wave implemented in waveguides.....	58
--	----

3.2.c: Corresponding phase terms implemented in the i th arrayed waveguide.....	58
---	----

3.3.a: The uniform grid.....	59
------------------------------	----

3.3.b: Initial estimate for zero crossings.....	59
---	----

3.3.c: Zero crossing determined.....	59
--------------------------------------	----

3.4: Illustration of the irregular phased array on a circular arc.....	60
--	----

3.5: Geometry of $r_n(y)$	60
---------------------------------	----

3.6: Focal point deviation in the near field.....	62
---	----

3.7: Focal point deviation in the far field.....	62
--	----

3.8: Near field focal point (1mm).....	63
--	----

3.9.a: Near field focal point (10mm).....	63
---	----

3.9.b: Midfield focal point (20mm).....	64
---	----

3.10: Dispersion relation for selected image planes.....	65
--	----

3.11: Dispersion relation for selected $_$ values.....	65
---	----

3.12: Monte Carlo simulation of 1 st and 2 nd harmonic peak intensity vs. random measure.....	66
---	----

4.1: Implementing a virtual spherical modulation in the arrayed waveguide.....	87
--	----

4.2: Setting up for random points.....	87
--	----

4.3: Section of ISZC modified arrayed waveguide lengths.....	88
--	----

Figure	Page
--------	------

4.4: Layout options for AWG device [45].....	88
--	----

4.5: Length constraint for array design of full layout [45].....	89
--	----

4.6: Vertical constraint for array design of full layout [45].....	90
--	----

4.7: Domain of BPM calculation.....	91
-------------------------------------	----

4.8: Geometry for calculating initial phase in the arrayed waveguides.....	91
--	----

4.9: The input window for WDM Router Description File Generator.....	92
--	----

4.10: Crank-Nicholson method (CN).....	92
--	----

4.11: Illustration of diffraction order for AWG output (the dashed lines represent wavelengths outside of FSR).....	93
---	----

4.12: Full layout of a 24-channel 100 AW regular AWG (m=40).....	94
--	----

4.13: The input coupler of the 24-channel regular AWG.....	94
--	----

4.14: The output coupler of the 24-channel regular AWG.....	95
---	----

4.15: Full layout of the ISZC AWG based on the 24-channel regular AWG.....	96
--	----

4.16: The input coupler of the ISZC AWG.....	96
--	----

4.17: A close-up view of the AW section of the regular AWG.....	97
---	----

4.18: A close-up view of the AW section of the ISZC AWG.....	97
4.19: The transmission spectrum of the 24-channel regular AWG scanned for 28 channels.....	98
4.20: Transmission spectrum of the ISZC AWG with 24 output ports.....	98
viii	
4.21: Transmission spectrum of the ISZC AWG with 28 output ports.....	99
4.22: 180-channel-0.3nm-spacing regular AWG transmission spectrum.....	100
4.23: A close-up view of the 180-channel regular AWG transmission spectrum..	100
4.24: ISZC AWG based on 180-channel regular AWG with 180 ports (200 channels scanned).....	101
Figure	Page
4.25: The transmission spectrum of the first 100 channels of the ISZC AWG (180 output ports, 200 channels scanned).....	101
4.26: The spectrum rest of the 80 channels for the ISZC AWG.....	102
4.27: A close-up view of the 200 channel ISZC AWG with 180 output ports.....	102
4.28: ISZC AWG based on 180-channel regular AWG with 200 ports (200 channels scanned).....	103
4.29: The transmission spectrum of the first 100 channels of the ISZC AWG(200 output ports, 200 channels scanned).....	103
4.30: The spectrum of the second 100 channels for the ISZC AWG.....	104
4.31: A close-up view of the 200-channel ISZC AWG with 200 output ports.....	104
5.1: The output coupler input-output diagram.....	116
5.2: Dispersion in single-mode optical waveguide as a function of wavelength....	116
5.3: Random locations of xi's on the x-axis.....	117

5.4: Probability density function of z.....	117
5.5.a: Noise spectrum with 500 points on x-axis $x=20$ μ m.....	118
5.5.b: Noise spectrum with 1000 points, $x=10$ μ m.....	118
5.5.c: Noise spectrum with 2000 points, $x=4$ μ m.....	119

ix

5.6.a: Crosstalk noise and wavelength channel width of ISZC AWG's for fixed channel count (200).....	119
5.6.b: Crosstalk noise and wavelength channel width for ISZC AWG's with fixed waveguide spacing (15 μ m).....	120
5.6.c: Crosstalk noise and channel bandwidth for ISZC AWG's with fixed overall aperture size (3mm).....	120
5.7.a: 1024-channel ISZC AWG with 300 AW's (OAS=4.5mm).....	121
5.7.b: A close-up view of a 256-channel ISZC AWG with 200 AW's (OAS=1mm).....	121

Figure	Page
5.7.c: A close-up view of a 512-channel ISZC AWG with 500 AW's (OAS=3mm).....	122
5.8: The coordinate systems for Gaussian beam diffraction analysis.....	122
5.9: The overall Gaussian intensity profile at the OC output.....	123
5.10: The bandwidth of individual channels.....	123
A.1: Same as 4.4.....	134
A.2: Same as 4.5.....	135
A.3: Same as 4.6.....	136

ABSTRACT

Lu, Ying Ph.D., Purdue University, August 2003. Dense Wavelength Division Multiplexing/Demultiplexing by the Method of Irregularly Sampled Zero Crossings. Major Professor: Okan K. Ersoy.

The tremendous growth of Internet traffic has created increasing demand on high capacity optical communications networks. Dense wavelength division multiplexing (DWDM) networks has emerged as a very attractive option. Systems for optical wavelength demultiplexing have generated much interest in research and development. Since its first appearance, the Arrayed Waveguide Grating (AWG) has become the mainstay for the high channel count demultiplexing applications. In classical AWG design, the number of wavelength channels to be resolved is directly limited by the Free Spectral Range (FSR), and ultimately the channel count of an AWG is limited by the number of arrayed waveguides that could be fit on the substrate on which the AWG is fabricated. The harmonic images generated outside the FSR limit additional channels beyond FSR. In this work, a novel array waveguide grating (AWG) design method is proposed to achieve large channel count in a single stage. The Method of Irregularly Sampled Zero Crossings (MISZC) with a spherical wave applies non-periodic/irregular placement of apertures of the grating structure combined with holographic techniques based on zero crossings with a virtual spherical reference wave. As a result, the

restriction of free spectral range (FSR) for the regular AWG is eliminated. Thus, high channel count (>500) can be achieved in a single stage with reasonable noise level. Theoretical derivation and analysis of MISZC is presented. Detailed simulations using BeamPROP™ and Matlab™ tools are reported to show good agreement with the theory and analysis.

1. LITERATURE REVIEW

1.1 Background in WDM Communication Networks

In recent years, the tremendous growths in Internet activities such as multimedia communications and networking have created an ever-increasing demand on network capacity. The wavelength division multiplexing/dense wavelength division multiplexing (WDM/DWDM) based networks have emerged as a very attractive option to gradually upgrade network transport capacity without huge investment in laying new optical cables. In the WDM/DWDM scheme, the existing fiber cables are used to carry increasing number of wavelengths instead of single wavelength carried by the fiber cables in the early 1990's. Originally started at 4 wavelength channels per fiber in the mid 1990's, current systems transporting up to 128 wavelength channels in a single fiber are commercially available (for example DWDM systems by Cisco). However, more commonly deployed systems support 32 to 64 channels. Aggregate system capacity has reached Tera bits/second milestone in system demonstrations by major vendors in 1998 [1-3]. Wavelength multiplexing and demultiplexing is seen as one of the enabling technologies to implement a WDM network. It provides functions for components such as optical amplifiers, wavelength converters, and optical cross-connects that are crucial to the performance of an entire system. Figure 1.1 shows the evolution of optical networks and functions of various components.

1.2 Wavelength Demultiplexing In WDM Networks

As a result of intensive research and development effort, the WDM technology is advancing at a brisk pace. In terms of laser source and transmission technology, the current industry record is set in a system which generated 1,022 channels using a single laser, and transmitted all 1,022 wavelength channels on a single fiber [4]. Future systems that can generate and transmit 10,000 channels in one fiber are envisioned. Noteworthy is

the channel wavelength spacing in the Lucent demonstration which shrank from common DWDM standard of 50GHz to 10GHz with the goal of below 5GHz for future experiments [4]. The current trend is to pack more channels on a single fiber, with the long term objective of creating a revolutionary all optical and more intelligent network providing benefits of improved network efficiency and quality of service (QoS) in addition to a quantum leap in system capacity. These developments have created a large demand for high performance and flexible devices such as Wavelength Add/Drop Multiplexer (WADM) and Optical Cross-Connect (OCC), which are able to manipulate data paths through wavelength channels by optical means. One of the core functions repeatedly used in these devices is wavelength multiplexing and demultiplexing. It is not surprising that research to develop high performance wavelength demultiplexers with low channel cross talk, flat transmission characteristics, polarization independence, high channel count, and the ability to integrate with active components such as detectors, modulators, optical amplifiers has attracted strong interest in both academia and industry. The objective of these efforts is to produce a wavelength demultiplexer with 1) very high channel count, 2) good filter characteristics for each channel such as low cross talk, flat passing band, low signal to noise ratio, and so on, 3) ability for miniaturization and monolithic fabrication with active devices.

1.3 Implementations of Wavelength Demultiplexers

Wavelength multiplexers and demultiplexers other than arrayed waveguide gratings (AWG), which will be discussed separately, have been realized in a number of technologies, such as liquid crystals, fiber Bragg gratings, thin-film, and conventional concave gratings among others. While these devices have performed well in particular experiments and some of them are currently deployed in practical systems, they all suffer from various limitations; such as their limited potential for very high channel count (>64) and inability for monolithic integration with other active devices. Furthermore, liquid crystal based devices are free space devices; they use liquid crystal pixels as voltage controlled diffractive phase elements to modulate the output wave phase front and to demultiplex the input signal. Due to the limitation of available phase levels in these

materials, a large number of pixels have to be used to bring a satisfying control of the output phase front to achieve large channel count, which requires a complex driving circuitry, resulting in a relatively large overall size while providing limited number of channels. The thin-film wavelength filters are interference devices, using alternating layers of high and low refraction index materials to produce a Fabry-Perot like resonant cavity. They are thermally stable and easy to construct. However they tend to have wide channel spacing, and a major obstacle is their inability to scale up the channel count. A single device can provide usually no more than 32 channels [5]. In order to increase channel count, these filters need to be cascaded. Then, insertion loss (loss occurs between successive optical components) may be unsustainable. Fiber Bragg-grating filters are made of fibers having chirped or periodically varying index of refraction along the longitudinal direction. When the Bragg diffraction condition is met, as a result of the variation of index of reflection, each of these individual reflection planes can cause partial backward reflection of a particular frequency that is propagating forward along the fiber, and they will add up in phase. This induces a strong reverse propagation of a particular frequency component of the forward propagating input signal. As wavelength demultiplexers, they are constructed as bandstop filters to reflect different wavelength channels. Tunable fiber Bragg gratings are reported [6]; they can be used in N to 1 wavelength demultiplexing applications. Nevertheless, due to the two terminal nature of the fiber, N×N wavelength demultiplexing is difficult to construct [7]. A moderate channel count (32 channels) already requires a large number of filters to be cascaded in addition to auxiliary couplers and optical circulators to provide the demultiplexing function. Furthermore, the fiber grating based wavelength demultiplexers cannot function as multiplexers as Arrayed Waveguide Grating (AWG) based devices do when the input and output are reversed.

1.4 Wavelength Demultiplexing Using Arrayed Waveguide Gratings (AWG)

Here we give a brief description of the conventional AWG demultiplexer. Different names such as *phased arrays* (PHASAR), *arrayed waveguide gratings* (AWG), and *waveguide grating router* (WGR) all have been applied to this type of wavelength

demultiplexer. In open literature, the name of arrayed waveguide gratings (AWG) is most frequently used, and we follow this convention in this thesis.

The Arrayed Waveguide Grating (AWG) based demultiplexers are actually phase-modulating gratings arranged to bring sampling and synthesis functions together. An AWG demultiplexer essentially comprises of two usually identical Free-Propagation Ranges (FPR)/Focusing Slabs/Star Couplers, and an array of waveguides that connect the two focusing couplers as shown in Figure 1.2. The input coupler samples the diffracted input wave phase front at the apertures connected to the arrayed waveguides. Disregarding the effects of the arrayed waveguide, we assume that the sampled phase front is transferred to the apertures connected to the arrayed waveguides in the output coupler, and then the diffraction of these samples in the output coupler can be used to reverse the diffraction process having occurred in the input coupler. The original input image to the input coupler is reproduced at the output end of the output coupler. So the two couplers function to sample and synthesize the input image, noting that such periodic sampling and synthesis do generate multiple harmonics at the output end of the output coupler. With proper choice of geometry such as the confocal geometry [12], the diffraction process resembles an approximate Fourier transform relationship. The arrayed waveguides between the input and output couplers provide wavelength dependent linear phase shift for the input wavefront to the output coupler so that different wavelength inputs can be separated at the output. The linear wavelength-dependent phase shift is achieved by increasing the lengths of arrayed waveguides linearly in spatial order. Thus a linear displacement of focusing points with respect to their wavelengths is obtained. Figure 1.3 presents a one-to-one comparison of the AWG demultiplexer with its system theory interpretation.

Major advantages of AWG demultiplexers over other currently available implementations are their compactness in size and their potential to offer very high channel count. Furthermore, the insertion loss of an AWG does not increase linearly with channel counts as it does for the thin-film and fiber Bragg gratings. InP-based AWG devices with 16 channels have the typical device size of 4.0 mm \times 5.3 mm [15]. Silica-based AWG devices with cascaded stages have achieved channel count as high as 320

and 480 [16, 17]. The AWG demultiplexers are the most promising to meet the need of the future ultra-dense WDM systems (>1000 channels).

The original Arrayed Waveguide Grating was proposed by Smit [11] in 1988. Since then, it has remained an active research area for more than a decade. First wavelength demultiplexer design of arrayed waveguide grating was accomplished with optical lens arrangement and glass waveguide with 0.63 nm resolution [14]. The AWG as we see now was reported in 1991 [12, 13], which integrated the optical lens function on the same silicon substrate with the arrayed waveguide gratings by star coupler arrangements to provide the focusing function. In 1993, InP AWG demultiplexer was demonstrated, which paved way for further miniaturization and integration with active components [18]. Currently, AWG demultiplexers are implemented on both Silicon and InP substrates. The silicon-based AWGs utilize more mature processing techniques, and coupled with their larger size, they offer better cross talk performance characteristics. As a result, the silicon based AWGs provide high channel count. In comparison to the silicon based AWG's, the InP based AWGs tend to have lower channel count. Only 64-channel devices have been reported thus far, due partially to high cross talk margin [19]. Nevertheless, because of their reduced size and their potential for larger scale integration, the InP based AWGs are posed to gain ground in the future. The typical size of InP based AWGs is two orders of magnitude smaller than already highly integrated silicon based AWGs, for example from several cm^2 to several mm^2 [15]. Furthermore, the InP based AWGs are capable of integrating with a large number of active GaAs based optoelectronic components, which can be grown on the InP substrate as a result of InP and GaAs lattice structure match, whereas integration of large number of GaAs components on silicon substrate is limited. While silicon-based AWGs up to 40 channels are commercially available now, and higher channel count silicon based AWGs are in the pipeline, more attention has been given to develop the InP based AWGs for communications applications. In order to achieve high channel count for the InP based AWGs, gains need to be made to improve cross talk margin, flatness of pass band, channel gain variation, and polarization dependency. Some of the difficulties lie in the fact that the fabrication process of InP AWGs is extremely stringent due to small device

dimensions [18]. The typical InGaAsP raised strip waveguide grown on an InP substrate has a cross section dimension of $2.60\mu\text{m} \times 1.90\mu\text{m}$ [20]. As we see previously, in order to increase the channel count, the sampling rate has to be increased. The size and fabrication condition of InP based AWGs limit the number of waveguides available on the devices. Once the number of waveguides is fixed, the size of Free Spectral Range (FSR), which is linearly proportional to the number of waveguides, is limited [32]. Due to the diffraction of the limited extent of the arrayed waveguide coverage at the interface of the arrayed waveguides and the output coupler, each wavelength channel has a finite width, i.e., the number of wavelength channels is limited given the fixed FSR. Adding more wavelength channels only generates interference patterns. It will be helpful if there is a way to reduce higher order harmonics and extend the FSR of a grating structure. Then, more wavelength channels can be added.

1.4 Wavelength Demultiplexing Using MISZC

In this work, a novel wavelength-demultiplexing scheme is proposed and investigated in detail. This scheme is based on the Method of Irregularly Sampled Zero Crossings (MISZC), which can be used to suppress higher harmonic order diffractions when used in grating structures. The application of this method in grating structures for wavelength demultiplexing can in theory extend the Free Spectral Range of such gratings to infinity. This design is used to improve conventional arrayed waveguide gratings (AWG), which is currently the popular wavelength demultiplexer implementation. The results show MISZC can extend advantage of high channel count provided by conventional AWG, at the cost of increased but tolerable floor noise.

1.4.1 A Brief Description of the Method of Irregularly Sampled Zero Crossings

The proposed method of AWG design takes advantage of irregular and zero-crossing sampling techniques [1]. In the Fraunhofer region, through the diffraction process, the relationship between the field originated from a grating structure to the field on object/focal plane can be closely expressed as a Fourier Transform relation. The output wavefront generated at the focal plane is the Fourier Transform of the wavefront

originated at the grating output. So the multiple orders of diffraction output pattern at the focal plane can be viewed as a result of the periodic sampling of light waves by the grating structure. In addition, quantization of phase leads to other harmonic images. Contrary to periodic sampling of wavefront by grating structures, MISZC is a non-periodic sampling method. It samples the output wave phasefront at irregularly placed zero crossings. In this way, fields of higher diffraction orders are turned into background noise. The algorithm involves two major steps: 1) Generate randomized points preferably based on a uniformly spaced grid, 2) For each point, find the closest zero crossing point to the sampling point. By adjusting the randomness measure, the power in the higher order diffractions/harmonics can be reduced to noise. This algorithm is used to modify the existing AWG demultiplexer.

1.4.2 Applying MISZC to AWG Structure

To apply MISZC to the regular AWG structure, modulation by an additional reference wave is useful, a spherical reference wave in our case. One consequence of spherical phase modulation is to generate rapid phase variation and to make extremely large number and closely spaced zero crossing points available on the phasefront. Therefore, once a randomized point is generated; a closeby zero-crossing point can be easily determined. The spherical reference wave or a similar wave, for example, with parabolic phase variation, is also necessary for the removal of harmonics due to nonlinear encoding of phase. The wavelength demultiplexing function originally provided by uniformly spaced and linearly increasing arrayed waveguide lengths is replaced by an irregularly spaced and probably still incorporating linearly increasing arrayed waveguide lengths, in addition to the length changes due to the spherical reference wave. The effectiveness of the method is shown through a rigorous derivation and numerical simulation using both Matlab and industry standard software (Rsoft *BeamPROP*TM). The BeamProp simulation clearly shows the potential of this technique to extend Free Spectral Range (FSR) of a conventional AWG.

1.5 Organization of the Dissertation

The following is an outline of the contents of the thesis. In Chapter 2, Wavelength demultiplexing using the method of irregularly sampled zero crossings (MISZC) is covered. Theories of zero crossing sampling and irregular sampling are derived separately. The theories show both zero crossing and irregular sampling methods are effective in removing high harmonic focal points. Matlab simulation results based on derivation of both zero crossing sampling and irregular sampling are presented and compared with theoretical predictions. In Chapter 3, simulation of AWG using Matlab tools is described. An in-depth discussion of general AWG simulation utility is presented, which can be used to simulate MISZC enhanced AWG structures. It is fast and accommodates high channel count capabilities that is provided in MISZC enhanced AWG device. Chapter 4 covers Implementation of MISZC using Rsoft *BeamPROP*TM AWG layout software and simulation results as well as discussion on the Beam Propagation Method (BPM) used for simulation; Chapter 5, a discussion of noise effect of ISZC based AWGs and channel capacity are given; Chapter 6 provides conclusions and future research.

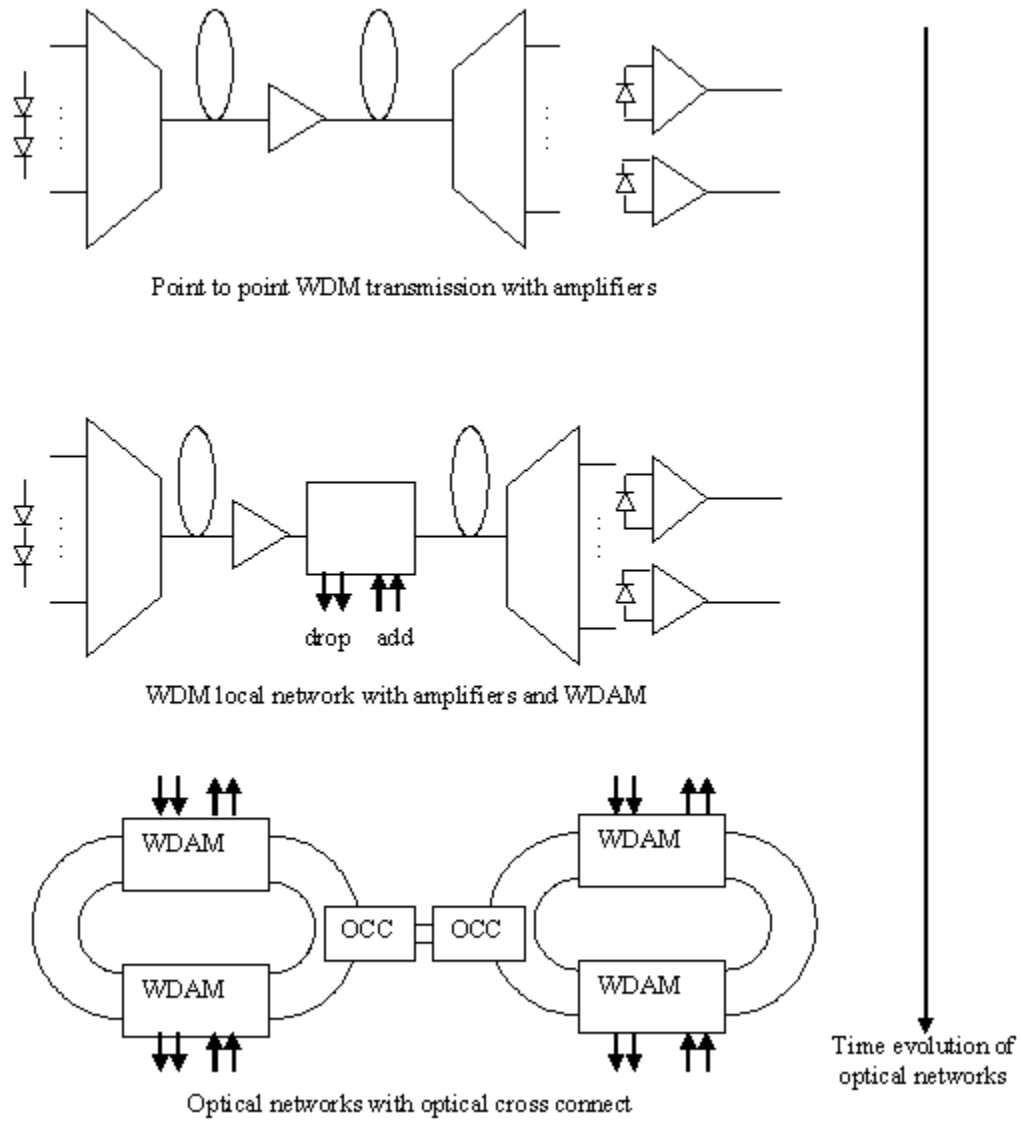


Figure 1.1 Evolution of optical networks

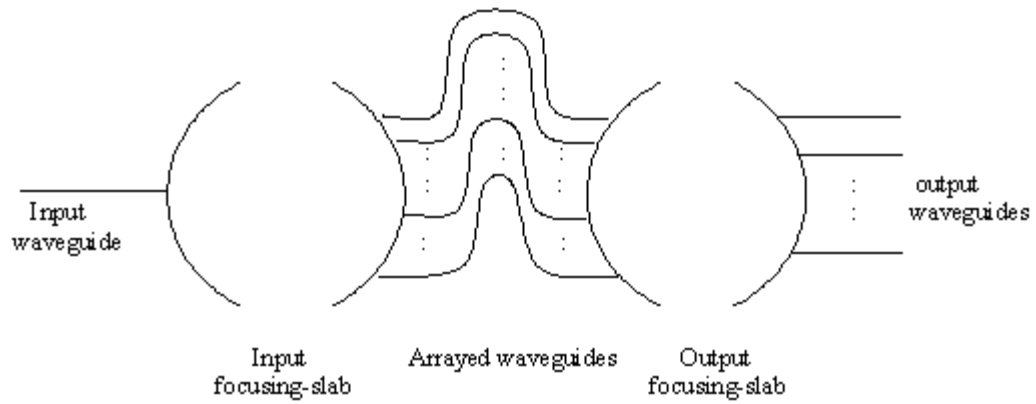


Figure 1.2. Essentials of an AWG demultiplexer

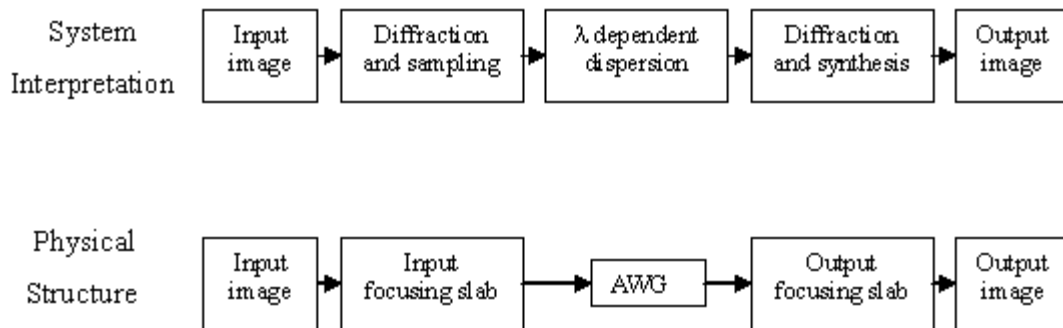


Figure 1.3. System theory interpretation of the AWG structure

2. WAVE OPTICS MODELING OF AWG DEVICES

In this chapter, an introduction to the operation of regular AWG's is provided. Based on the discussion of AWG, a scalar wave model of an AWG is constructed. Simulation results of this model have shown good agreement with the commercial software package introduced in later chapters. The motivation is to create an in-house tool for fast trial runs. It also provides flexibility to implement design features that are difficult to deal with in most commercial software that are based on assumptions of regular AWG. The simulations for irregularly spaced zero crossing (ISZC) AWG design were developed based on this model. The framework of our model leaves room for more accurate waveguide computing routines using BPM and FDTD techniques to further improve accuracy. Before going any further, an introduction to the operation principles of regular AWG device is in order.

2.1 Introduction to the Operation of Regular AWG

The AWG demultiplexers are wavelength varying imaging devices. As shown in Figure 2.1.a, an AWG device is built on semiconductor substrate; it consists of three major parts: an input coupler (IC), an output coupler (OC), and an array of waveguides (AW) connecting the two couplers. There are also input and output waveguides (IW/OW) that couple the input and output light to and from the AWG demultiplexer. In general, the input/output couplers could be filled with either air or dielectric [32]. The input/output couplers are identical and designed using either the Rowland or the confocal geometry. For a multi-wavelength input, wavelength demultiplexing is achieved by forming separate focal points for every wavelength presented at the end of OC. The demultiplexed signal is then coupled to the output transmission waveguides. The major steps in achieving wavelength demultiplexing are the diffraction, which occurs in both couplers, and the wavelength induced linear phase dispersion, which occurs in AW's. These steps are discussed in detail in the following before deriving key equations.

Through a single mode waveguide, the multi-wavelength input signal enters and diffracts in IC. A diffraction pattern is formed at the end of the input coupler region. The light wave is then coupled into the AW's at the interface of IC and AW (IC/AW). Due to the path length difference arranged in the AW's, such that linear phase dispersion is generated among different wavelength components of the multi-wavelength input signal as the light wave travels through the arrayed waveguides. In this way, the AW's provide wavelength dependent linear phase dispersion much like a conventional grating. At the AW/OC interface, the light wave is launched to the output coupler and diffracted. Given that the interfaces of IC/AW and AW/OC are mirror images of each other, the diffraction process in OC mirrors that in IC, except the phase front at AW/OC is altered by the AW. In fact, AW's provide wavelength induced phase dispersion and IC/OC provide the focusing function.

To illustrate the wavelength demultiplexing mechanism of regular AWG, we first examine the path-lengths of the arrayed waveguides. These lengths of individual waveguide and the constant path length difference ΔL between adjacent waveguides are chosen in such a way that the phase retardation for the light wave of the center wavelength is $2m\pi$. So the phase front of the light wave coupled to the AW's from the IC is reproduced exactly at the AW/OC interface for the center wavelength, assuming all AW's are de-coupled. As the light wave propagates through the OC region, at least one focal point can be formed at the end of the OC, given the center wavelength is applied.

For the light waves of other wavelengths propagating through the AW's, due to the chromatic dispersion in the AW's, the phase-fronts of different wavelengths are tilted by wavelength dependent linear phase dispersion as the light wave reaches the AW/OC. As a result, the focal points of different wavelengths will be dispersed linearly at the end of OC. By controlling the path difference ΔL , i.e. the order of diffraction, the focal point of each wavelength component can be determined.

The analysis of the AWG demultiplexers consists of the analysis of the three major components of the device, the two focusing couplers and the AW's. The waveguides are standard single mode waveguides, which are pretty well understood. An accurate description of the diffraction processes in the two focusing couplers is much

more complicated. There are different proposals for the focusing-coupler geometry [32-34]. The classical Rowland geometry is used in early AWG structures [32], later the confocal geometry is used [33], and multiple Rowland geometry is also proposed [34]. The classical Rowland geometry was first used in concave gratings for spectroscopy [40]. It was invented by Rowland in a reflection concave grating design in 1882. The spherical concave gratings using Rowland geometry provide the advantage of combined focusing and dispersion function over the planar gratings. Early designs of AWG's adopted this geometry. The confocal geometry is most easily analyzed and provides the same function. It consists of two spheres of same radius with centers on the surface of each other. In the Fraunhofer diffraction region, the paraxial approximation can be applied. The diffraction process, which relates the original image and the diffracted image on the two spherical surfaces, can be accurately modeled by a spatial Fourier transform [23]. This greatly facilitates the analysis of focusing couplers of the AWG devices. Most current AWG designs use the confocal geometry [12-14, 32, and 36-39]. Differing from classical gratings, for AWG demultiplexers, the dispersion function is provided by the arrayed waveguides, and the coupler geometry needs only to provide the focusing function. So in this work, the confocal geometry is investigated.

Similar analyses of the AWG demultiplexers have been put forth in literature [32, 35, and 36]. They assume that the interfaces at the ends of the couplers with the arrayed waveguides are planar. It is a good approximation; usually the ends of the couplers are arcs of small radial angle and large radius compared to the arcs. The following is a first-order analysis of the AWG demultiplexer adopted from a paper by Okamoto [32]. It gives accurate focusing and dispersion properties of the demultiplexing operation, which is then used to test the simulation results of the scalar wave model.

Consider Figure 2.1b. In the IC region, the spacing between the ends of adjacent input transmission waveguides on the IC is D_1 , the separation of AW's at the IC/AW interface is d_1 , and distance measured from the center of the input side of the IC is x_1 . The radius of the IC/AW interface is f_1 . In the OC region, the spacing between the ends of adjacent waveguides connected to the array waveguides is d . The spacing between the ends of adjacent output transmission waveguides is D . And the radius of the AW/OC

interface is f . As mentioned earlier, the path differences between two adjacent AW's is ΔL and the phase retardation is $2m\pi$ with respect to the center wavelength for ΔL and all AW's. In Figure 2.1.c, the OC is illustrated. The AW's are located at the lower portion of the diagram; the upper portion of the diagram shows the output transmission waveguides. Light wave propagates from the bottom to the top of the diagram. Let us consider the light beams passing through the i^{th} and $(i-1)^{\text{th}}$ array waveguide shown in the lower portion of the diagram. In order for the two light beams to interfere constructively at the output of the OC, their phase difference should be multiples of 2π as they reach the output end of the focusing coupler region. So the condition for constructive interference is,

$$\begin{aligned} & k_s(\lambda_0) \left(f_1 - \frac{d_1 x_1}{2f_1} \right) + k_c(\lambda_0) [L_c + (i-1)\Delta L] + k_s(\lambda_0) \left(f + \frac{dx}{2f} \right) \\ &= k_s(\lambda_0) \left(f_1 + \frac{d_1 x_1}{2f_1} \right) + k_c(\lambda_0) [L_c + i\Delta L] + k_s(\lambda_0) \left(f - \frac{dx}{2f} \right) - 2m\pi \end{aligned} \quad (2.1)$$

where k_s and k_c denote the propagation constants in coupler region and array waveguide, m is an integer, λ_0 the center wavelength of the multiple wavelength input and L_c the minimum array waveguide length. Subtracting common terms from Equation (2.1), we obtain

$$k_s(\lambda_0) \frac{d_1 x_1}{f_1} - k_s(\lambda_0) \frac{dx}{f} + k_c(\lambda_0) \Delta L = 2m\pi \quad (2.2)$$

When the condition $k_c(\lambda_0) \Delta L = 2m\pi$ or

$$\lambda_0 = \frac{n_c \Delta L}{m} \quad (2.3)$$

is satisfied for λ_0 , the light input position x_1 and the output position x should satisfy the condition

$$\frac{d_1 x_1}{f_1} = \frac{dx}{f} \quad (2.4)$$

In Equation (2.3), n_c is the effective index of the array waveguide ($n_c = k_c/\gamma$, γ : wave number in vacuum), and m is called the diffraction order. The above equation determines the output position x , given that light is coupled to the IC at input position x_1 . Usually the waveguide parameters in the input and output coupler regions are the same. So input and

output distances are equal as $x_1=x$. Thus for the center wavelength, output is the mirror image of the input. Since the AW's gives only integer multiples of 2π phase shifts, the IC and OC essentially functions as a lens. For demultiplexing purpose, the input transmission waveguide is located at the center of the input of the IC. Given the symmetry, the center wavelength is located at the center of the end of the OC. For a general wavelength λ , the dispersion of the focal position x from the focus of the center wavelength for the fixed light input position x_1 is given by differentiating Equation (2.2) with respect to λ as

$$\left| \frac{\Delta x}{\Delta \lambda} \right| = \frac{N_c f \cdot \Delta L}{n_s d \lambda_0} \quad (2.5)$$

where n_s is the effective index in the coupler region, and N_c is the group index of the effective index n_c of the array waveguide ($N_c = n_c - \lambda dn_c/d\lambda$), respectively. The dispersion of the input side position x_1 with respect to the wavelength λ for the fixed light output position x is given by

$$\frac{\Delta x_1}{\Delta \lambda} = \frac{N_c f_1 \cdot \Delta L}{n_s d_1 \lambda_0} \quad (2.6)$$

The input and output waveguide separations are $|\Delta x_1| = D_1$ and $|\Delta x| = D$, respectively when $\Delta \lambda$ is the channel spacing of the WDM signal. Putting these relations into Equations (2.5) and (2.6), the wavelength spacing in the output side for the fixed light input position x_1 is given by

$$\Delta \lambda_{\text{out}} = \frac{n_s d D \lambda_0}{N_c f \Delta L} \quad (2.7)$$

And the wavelength spacing in the input side for the fixed light output position x is given by

$$\Delta \lambda_{\text{in}} = \frac{n_s d_1 D_1 \lambda_0}{N_c f_1 \Delta L} \quad (2.8)$$

Given $D_1 = D$, $d_1 = d$ and $f_1 = f$, the channel spacing are same as $\Delta \lambda_{\text{in}} = \Delta \lambda_{\text{out}} \equiv \Delta \lambda$. The path length difference ΔL is obtained from Equation (2.7) or (2.8) as

$$\Delta L = \frac{n_s d D \lambda_0}{N_c f \Delta \lambda} \quad (2.9.a)$$

Comparing to Equation (2.3), we get

$$m = \frac{n_e n_s d D}{\Delta\lambda \cdot N_c f} \quad (2.9.b)$$

In Equation (2.9.b), all the parameters on the right side are typically given, as they are either mostly related to waveguide fabrication process or specification for a given design. m , the grating order of the AWG device, can be determined by this equation. The spatial separation of the p^{th} and $(p+1)^{\text{th}}$ focused beams for the same wavelength is given from Equation (2.2) as

$$X_{\text{FSR}} = x_p - x_{p+1} = \frac{\lambda_0 f}{n_s d} \quad (2.10)$$

X_{FSR} represents the spatial free spectral range of the AWG. The number of available wavelength channels N_{ch} is given by dividing X_{FSR} with the output waveguide separation D as

$$N_{\text{ch}} = \frac{X_{\text{FSR}}}{D} = \frac{\lambda_0 f}{n_s d D} \quad (2.11)$$

Examining Equation (2.11), for a given AWG device to achieve high channel count, d and D need to be small. Nevertheless, d and D cannot be infinitely small; they are limited by the waveguide fabrication process, and are usually taken as constants. Therefore, given the requirements of a given N_{ch} , the input and output coupler curvature radius, f , can be determined. Then using Equation (2.9.b), the AWG grating order can be found. After that, L is determined from Equation (2.3). Thus, the basic AWG parameters are calculated. Based on these parameters and through a few more rounds of iterative processes through simulations, all AWG device parameters can be determined and used in layout design. More details on layout design are included in Chapter 4.

The diagram in Figure 2.2 illustrates the definition of the Free Spectral Range (FSR) and spatial free spectral range (X_{FSR}) for AWG devices. At the output end of the OC, the primary order of the output is located at the center of the output arc of the OC. The higher order harmonics are the spatially shifted version of the primary order output. The dashed intensity profiles in red and violet showing the extra wavelength channels added at the input. One can see from the diagram that there is overlapping between the

primary order and higher order outputs, when additional wavelength channels are applied. In order to increase the wavelength channel, the higher harmonic order outputs should be eliminated. The cause of the higher harmonic orders is related to the geometry of the output coupler and the placement of the arrayed waveguides at AW/OC interface. Note that the mapping of temporal and spatial wavelengths on the same set of outputs. The wavelength span that covers the repeated spatial harmonic order is called FSR.

2.2 Scalar Wave Based AWG Simulation

In this section, we discuss a scalar wave based model for AWG simulation. The scalar wave AWG formulation is based on a two-step process. First, consider a single mode waveguide guiding the input light source into the input coupler. Since the single mode waveguide supports only LP_{01} mode, as input wave field propagates and expands in the IC, the field reaching the end of the IC can be modeled accurately as Gaussian. Then, this wave front is coupled into the AW's. The coupling is determined by the overlapping integral between the illuminating field and the waveguide modes. Due to the size of the couplers, far field diffraction appears in both input and output couplers, so the illumination can be considered constant over the width of the modal field of a single arrayed waveguide [39]. The amplitude and phase of the sampled field at the IC/AW interface can be determined by computing the distance from the end of the input waveguide to each AW. Then these sampled fields go through individual AW of different path lengths. As a result, at the end of the AW's, i.e. at the AW/OC interface, the aggregate field is a phase-shifted and amplitude-reduced (due to losses) version of the original Gaussian wavefront sampled at the IC/AW interface. In the second step, these fields are then launched into the output coupler. At the end of the output coupler region, a diffraction pattern is formed, and individual wavelengths are demultiplexed and coupled to the output transmission waveguides. The following formulation is based on this two-step process. The light field emanating out of the input transmission waveguide, before being launched in to the input coupler region, is modeled as input. The output coupler region diffraction process is modeled as a linear transform system. The image formed at the output arc of the output coupler region is considered as output.

2.2.1 The linear system formulation of AWG

As discussed previously, the light that travels through the input coupler can be modeled as a Gaussian beam for each wavelength. The input to the arrayed waveguide is ordered from 1 to M as in the geometry shown in Figure 2.3.a. Given wavelength λ and propagation constant k , for a Gaussian beam, the field amplitude and phase that are coupled in to the AW's are defined as the following [40]:

$$E_{in}(z_{in}, r_{in}) = E_0 \varepsilon_{in}(z_{in}, r_{in}) \quad (2.12)$$

$$\varepsilon_{in}(z_{in}, r_{in}) = \left\{ \frac{w_0}{w(z_{in})} \exp\left[-\frac{r_{in}^2}{w^2(z_{in})}\right] \right\} \exp\left\{-j\left[kz_{in} - \tan^{-1}\left(\frac{z_{in}}{z_0}\right)\right]\right\} \exp\left[-j\frac{kr_{in}^2}{2R(z_{in})}\right] \quad (2.13)$$

Where E_{in} is the wavefront that impinges on the IC/AW interface, ε_{in} represents the Gaussian beam, the rest of the parameters are given as

$$w^2(z_{in}) = w_0^2 \left(1 + \left(\frac{z_{in}}{z_0} \right)^2 \right) \quad (2.14.a)$$

$$r_{in}^2 = (R \sin \theta_{in})^2 \quad (2.14.b)$$

$$z_{in} = R \cos \theta_{in} \quad (2.14.c)$$

$$\theta_{in} = \frac{d}{R} \left(\frac{M+1}{2} - m \right), m = 1, 2, \dots, M \quad (2.14.d)$$

$$R(z_{in}) = z_{in} \left[1 + \left(\frac{z_0}{z_{in}} \right)^2 \right] \quad (2.14.e)$$

$$z_0 = \frac{\pi n_s w_0^2}{\lambda_0} \quad (2.14.f)$$

$$w_0 = \frac{W_{WG}}{\sqrt{2\pi}} \left(0.5 + \frac{1}{V - 0.6} \right) \quad (2.14.g)$$

W_{WG} is the width of the waveguide; the waist size of the Gaussian beam w_0 is taken as the effective width of the waveguide; V is the normalized frequency for the single mode waveguide ($2 < V < 4$) [41]; n_s is the refractive index for the coupling slab material; M is the number of arms of the AWG, θ_{in} is the angular variable, the symmetry of the confocal

configuration is the zero reference as shown in Figure 2.3.a. z_{in} is positive above the reference, and negative below the reference.

As the light wave propagates through the m^{th} arrayed waveguide and emerges at its end, we have

$$E_1(m) = f(m)E_{in}(r_{in}(m), z_{in}(m)) \quad m = 1 \text{L} M \quad (2.15.a)$$

$$f(m) = a_m \exp(j\psi_m) \quad (2.15.b)$$

$$\psi_m = k_c(\lambda)(L_c + m\Delta L) \quad (2.15.c)$$

where $E_1(m)$ is the output field at the end of the m^{th} arrayed waveguide; $f(m)$ is the overall amplitude and phase modulation factor induced by each arrayed waveguide, in addition to the coupling effect from the slab region into the arrayed waveguides; ϕ_m is the wavelength dependent phase dispersion, and a_m is the amplitude and phase factor accounting for coupling and waveguide loss. In our model, since the waveguide loss is not considered, and due to the constant irradiation of the input wave, coupling factor is a constant for all waveguides. Therefore, a_m is taken as unity. k_c is the propagation constant in the arrayed waveguide.

We next consider the output coupler shown in Figure 2.3.b. $E_1(m)$ gives the initial phase and amplitude of the Gaussian field to be launched from the m^{th} arrayed waveguide into the output coupler; ϕ_1 is the angular variable representing the arc on the right. There are N output ports on the right arc as shown in the diagram, and the entire right arc is sampled by P points. So ϕ_1 is discretized and presented as a vector with P elements. Again, we note that P is the number of sampling points at the end of the output coupler, and $P > N$ is satisfied, N being the number of the output wavelength channels. $E_2(m)$ is the field that is originated from the m^{th} waveguide, and has reached the right arc of the OC. The total field at the right arc of the OC is a scalar summation of all Gaussian field launched from every arrayed waveguide. The total field at point p is expressed as,

$$E_{out}(p) = \sum_m E_2(m) \quad (2.16.a)$$

$$E_2(m) = \varepsilon_m(p)E_1(m) \quad (2.16.b)$$

ε_m represents a diffracted Gaussian field launched from the m^{th} aperture of width W_{WG} on the AW/OC interface, is given as

$$\varepsilon_m(p) = jk \frac{W_{WG}^2}{2R} \exp\left[-\frac{(kW_{WG} \sin(\theta_1 - \theta_{1m}))^2}{4}\right] \exp(-jkR), \quad p = 1, 2, \dots, P \quad (2.17.a)$$

$$\theta_{1m} = \frac{\left(\frac{M+1}{2} - m\right)d}{R}, \quad m = 1, 2, 3, \dots, M \quad (2.17.b)$$

$$\theta_1 = [\theta_1(1) : \theta_1(2) : \dots : \theta_1(P)]^t \quad (2.17.c)$$

We can write,

$$E_{out} = GE_1 \quad (2.18.a)$$

given

$$E_{out} = [E_{out}(1) \dots E_{out}(P)] \quad (2.18.b)$$

$$E_1 = [E_1(1) \dots E_1(m)] \quad (2.18.c)$$

$$\varepsilon_m = [\varepsilon_m(1) : \varepsilon_m(2) : \dots : \varepsilon_m(P)] \quad (2.18.d)$$

$$G = [\varepsilon_1 : \varepsilon_2 : \dots : \varepsilon_M] \\ = \begin{bmatrix} \varepsilon_1(1) & \varepsilon_2(1) & \dots & \varepsilon_M(1) \\ \varepsilon_1(2) & \vdots & \vdots & \varepsilon_M(2) \\ \vdots & \vdots & \vdots & \vdots \\ \varepsilon_1(P) & \varepsilon_2(P) & \vdots & \varepsilon_M(P) \end{bmatrix} \quad (2.18.e)$$

E_1 in matrix form can be expressed as,

$$E_1 = E_0 \cdot \Psi \cdot \Sigma \quad (2.19.a)$$

given

$$\Sigma = [\varepsilon_{in}(1) : \varepsilon_{in}(2) : \dots : \varepsilon_{in}(M)] \quad (2.19.b)$$

$$\Psi = \begin{bmatrix} f(1) & 0 & \dots & 0 \\ 0 & f(2) & 0 & 0 \\ \vdots & 0 & \dots & \vdots \\ 0 & \dots & 0 & f(M) \end{bmatrix} \quad (2.19.c)$$

Electric field E_I can be regarded as the input to the linear system, i.e. the OC. The output of the linear system is E_{out} impinging on the right arc of the OC, so the system model is given as

$$E_{out} = E_0 \cdot G \cdot \Psi \cdot \Sigma \quad (2.20)$$

where E_0 is a constant related to the initial magnitude and phase of the Gaussian profile emanating from the input transmission waveguide. $\underline{\Sigma}$ is a 1 x M vector representing the phase accumulated over free propagation of Gaussian beam in the IC before the wavefront is coupled into M arms of the AW's. $\underline{\Psi}$ is a diagonal matrix of dimension M x M, the main diagonal representing the phase and amplitude change occurring in each of the arrayed waveguide. All other elements of $\underline{\Psi}$ are zero, since all AW's are decoupled. G is the linear transformation describing the OC which is an M x P matrix. P is the number of discrete sampling points used representing the right arc of the OC. We note that the matrix formulation simulates one wavelength at a time. E_{out} as shown in the formulation presents the spatial output of the AWG. When wavelength scan is applied at the input, by recording the output power at each one of the N output ports on the right arc of the OC, the transmission spectrum of individual output port is obtained. The transmission spectrum of AWG is obtained by plotting transmission spectrum of all output ports in same wavelength range. Figure 2.4.a shows how the transmission spectrum is obtained, noting Figure 2.4.b is shown as an example of loss spectrum which gives the decibel ratio of input to output power, is equivalent to transmission spectrum with the sign of the vertical axis reversed.

Simulation results are shown in the following section. Nevertheless, if a mask is need for AWG fabrication, the device layout should to be obtained. This can be accomplished in one of the standard commercial software package *BeamPROP*TM in the following chapter.

2.2.2 Application to ISZC AWG Simulation

Implementing the ISZC AWG is very convenient in our model, ψ_{in} and ψ_{1m} can be defined using parameters calculated in Chapter 3 for irregular AW placement on the IC/AW and AW/OC interfaces; $f(m)$ can also be substituted using calculated values obtained in Chapter 3. The major difference between the regular AWG and ISZC AWG design is the irregularly spaced arrayed waveguides and nonlinear increment of arrayed waveguide lengths. When the position and length increments of each arrayed waveguide is determined, given the flexibility of our model, the application to ISZC AWG simulation is straightforward. Chapter 3 has shown the details of determining x_i , the initial value of x_i is a random guess, using Equations (3.31) to (3.33), the correction Δ can be found to determine the exact x_i location. As it is shown in Figure 3.3, once x_i 's determine the vertical coordinates of a circular curvature, the location of each waveguide is obtained. In the scalar wave model, the spatial information of arrayed waveguides are contained in $\psi_{in}(m)$ and ψ_{1m} , which can be obtained through a simple transformation between vertical coordinates and radial angle from center of the curvature. The information for the lengths of each AW is determined by Equations (3.12.c) and (3.13). Then replacing ψ_m as

$$\psi_m = k_c(\lambda)(L_c + \alpha \cdot x_i + r_{oi} + r_{ci}) \quad (2.21)$$

After these simple changes, the model can be used for ISZC simulation. In most commercial simulation packages such as BeamPROP, the features of regular AWG, uniform waveguide spacing and constant length increment in subsequent waveguides are utilized to simplify design and simulation, and are hard-wired in coding. It is burdensome to work around these settings. The scalar wave model provides a fast and easy way to test ISZC AWG designs. Because the size of the coupler is much larger compared to the input light wavelength, the distortions of phase of the field due to coupling between coupler and arrayed waveguide and waveguide aperture size is negligible. The disadvantage is that the absolute loss cannot be simulation in this model; only normalized transmission is presented.

2.2.3 Simulation Results

A Matlab simulation program is written using the formulation discussed in this chapter. It is relatively simple to implement, and useful in providing quick results. To verify the correctness of the program, several tests have been performed to simulate standard AWG devices, and they yielded excellent agreement with the results obtained in Section 3.1. ISZC AWG results are also presented.

As we discussed in the previous chapter, as the output light wave is focused to the center of the right arc of the OC, the dispersion equation, Equation (2.5), describes demultiplexing in space. We used linear relations provided by this formulation to verify the simulation program. Equations (2.3) and (2.5) are repeated below for convenience,

$$\lambda_0 = \frac{n_c \Delta L}{m} \quad (2.3)$$

$$\frac{\Delta x}{\Delta \lambda} = \frac{N_c f \Delta L}{n_s d \lambda_0} \quad (2.5)$$

In the analysis we used $N_c=1.47332$, $n_s=1.45013$, $n_c=1.45213$ [39, 57], and $\lambda_0=1.55 \mu\text{m}$, $f=0.8\text{mm}$, $m=100$ $d=2.96 \mu\text{m}$. The ratio of $\frac{N_c f \Delta L}{n_s d \lambda_0}=29.08 \mu\text{m/nm}$ is required. Results are

shown in Figure 2.5 They are in excellent agreement with our computer experiment. The ratio from the simulation was obtained as $29.05 \mu\text{m/nm}$. The graphs are shown below. Figure 2.5 used same conditions showing different wavelength separation. Figure 2.6 has $m=60$ with same other parameters, the ratio computed being $17.50 \mu\text{m/nm}$, and the simulation gives $17.56 \mu\text{m/nm}$. For regular AWG with 20nm operation range the deviation from design is $0.8 \mu\text{m}$ (for $m=100$) and $0.6 \mu\text{m}$ (for $m=60$) at the output, which can be corrected in mask generation. We also show the transmission spectrum of a regular AWG with 300 AW's in Figure 2.7. In Figures 2.8.a, 2.8.b, 2.8.c, transmission spectrums of ISZC AWG designs, which are based on the regular AWG shown in Figure 2.7 with same number of AW's (300), are presented. The channel counts have increased from 36 for the regular AWG to 48, 72 and 96. The noise floor of an ISZC AWG is higher than regular AWG, however, as channel count increases, as long as the number of AW's are fixed, the noise level varies very little. The tradeoff is that when this noise is

tolerable, ISZC AWG can package more channels given the same number of arrayed waveguides. More detailed discussion on channel capacity is provided in Chapter 5. In the following section, using a simple Fourier transform relation, we can gain better understanding of the cause of FSR and the factors affecting channel bandwidth for regular AWG's.

2.3 Discussion

To specify approaches for optimizing the AWG demultiplexer design, an alternative view of the output coupler region from scalar diffraction theory perspective may provide additional insight into the interplay of the physical parameters such as AW spacing and overall aperture sizes of IC/AW and AW/OC interface (AW-spacing _ # of AW's) with device spatial characteristics such as spatial FSR (X_{FSR}) and spot size of individual focal points, which can be converted to the AWG frequency domain performance characteristics FSR and wavelength channel bandwidth. The following discussion is intended to illustrate these relations through Fourier analysis of focusing couplers starting from the scalar diffraction theory.

For two confocal spherical surfaces, the scalar diffraction theory asserts that the image forming on the right surface is the Fourier transform of the source field on the left surface [23]:

$$U(x, y) = \frac{e^{jkz}}{j\lambda z} \iint U(\xi, \eta) e^{-j\frac{2\pi}{\lambda z}(x\xi + y\eta)} d\xi d\eta \quad (2.22)$$

In order for this result to be valid, the dimensions of the two caps shown in Figure 2.9 should be small compared to the separation distance between them. This is satisfied in the AWG design [32, 33, 38, and 39]. This Fourier transform relation leads to a spatial domain to frequency domain transformation, which gives rise to the diffractive harmonic orders in regular AWG devices. Given a regular AWG, the input light entering the IC can be considered as a point source. The expanding wavefront in the IC can be regarded as spherical as it reaches the end of the IC. The circular arc at the IC/AW interface closely matches the expanded input wavefront. So, the waves coupled into the AW's have

approximately equal phase and amplitude. Since the wavelength of the input signal doesn't play a major role in FSR and channel bandwidth, to simplify our discussion, we consider only the center wavelength for now. Rigorous derivation is carried out in Chapter 5 to address other wavelengths in detail. At AW/OC interface, light wave at the end of each waveguide still retains the same phase, because integer multiples of 2π phase shifts are generated in each waveguide by design (Section 2.1). Each AW launches a Gaussian field into the output coupler. When the output coupler is considered as a linear system, its input field is a repetition of Gaussian fields uniformly (periodically) placed in space (its left arc). The field at the right arc of the output coupler is the spatial Fourier transform of the input field at the left arc. The input field can be expressed as a product of the periodic δ function and a window function together convoluted with a Gaussian function. Using Fourier transform properties, the output becomes a periodic sinc function weighted by a Gaussian function in frequency domain. The process is shown below.

In Figure 2.10, the spatial domain represents the input field at the left arc in Figure 2.9; and the frequency domain represents the output field at the right arc in Figure 2.9. Compared to Figure 2.9, in Figure 2.10, the dimension is reduced from 3D to 1D. In Figure 2.10, the output of the center wavelength channel, which is repeated at the output, is shown. The distance between two center wavelength outputs is X_{FSR} . The rest of the demultiplexed multi-wavelength outputs in FSR should fall between the repeated outputs of the center wavelength channel. From this simple analysis, we can see that the X_{FSR} is inversely proportional to the spacing of the arrayed waveguides at the input side of the focusing coupler. This is consistent with the ray optics calculation [32]. So closer spacing can result in larger X_{FSR} , which means a larger FSR, yet this is limited by the spacing between adjacent waveguides. The sharpness of the sinc function, which is the image of the focusing spot, is positively correlated to the size of the window function. Therefore, the larger the total aperture window, the sharper the focus, i.e. narrower individual channel bandwidth, which means more channels can be accommodated. The maximum size of the aperture window is limited by the size of the substrate the AWG device is built. This analysis agrees with reports in the literature [33], which proposed that the profile of the window be changed to a Gaussian instead of a rectangular, the individual

channel profile would be changed from a sinc function to a Gaussian. Therefore the secondary sidelobes can be reduced. This can help to lower cross talk between individual channels. Another observation is that the shape of the Gaussian amplitude profile of each waveguide relates to the overall passband flatness, i.e. output channel uniformity. The narrower the waveguide, the flatter is the overall amplitude profile at output of IC, i.e. the right arc in Figure 2.9.

Even though this analysis is restrained by the Fresnel approximation, the observation should point to the direction of optimization. In other words, a large number of waveguides and close spacing between them are required to achieve large channel count regular AWG's. The limited space on a semiconductor substrate and minimum distance required to keep the arrayed waveguides uncoupled put a limit on the maximum number of channels achievable by a regular AWG. By placing arrayed waveguides irregularly, we can eliminate FSR; therefore the limit on number of wavelength channels due to FSR can be lifted. However, simply placing arrayed waveguides irregularly may eliminate FSR. It can also comprise the wavelength demultiplexing function of an AWG. To achieve both objectives, ISZC has proven to be an excellent approach.

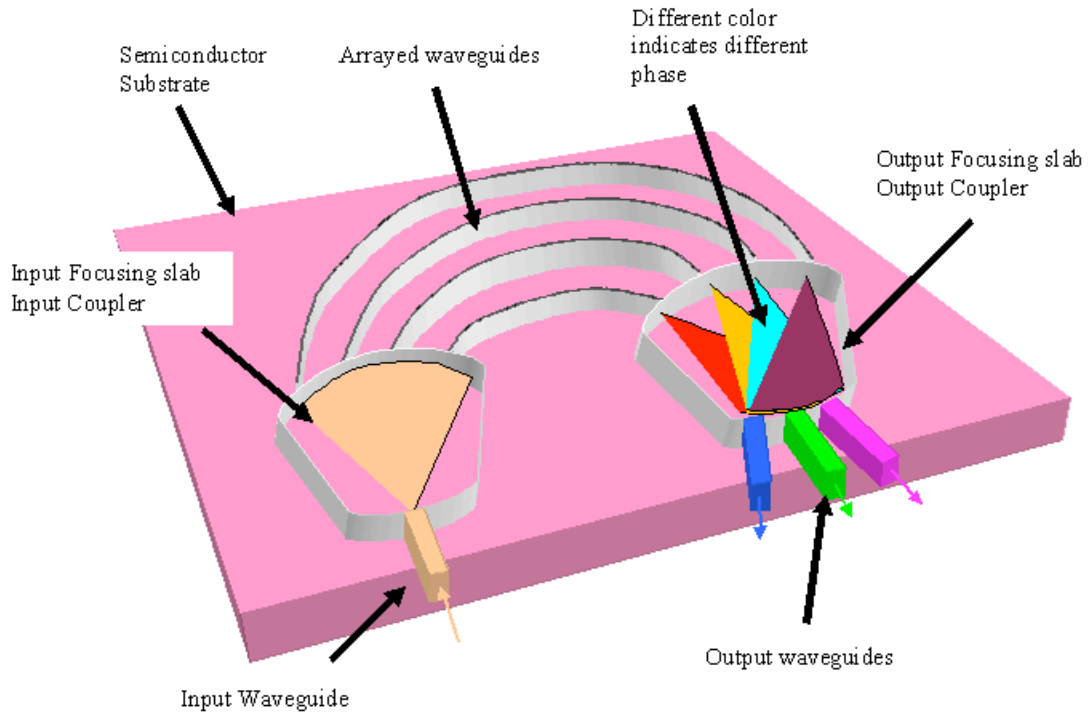


Figure 2.1.a. A sketch of AWG demultiplexer.

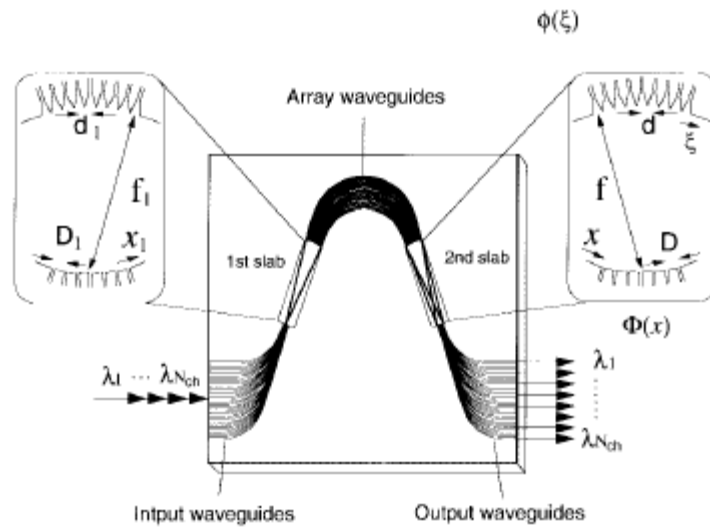


Figure 2.1.b. Definition of AWG demultiplexer parameters [11].

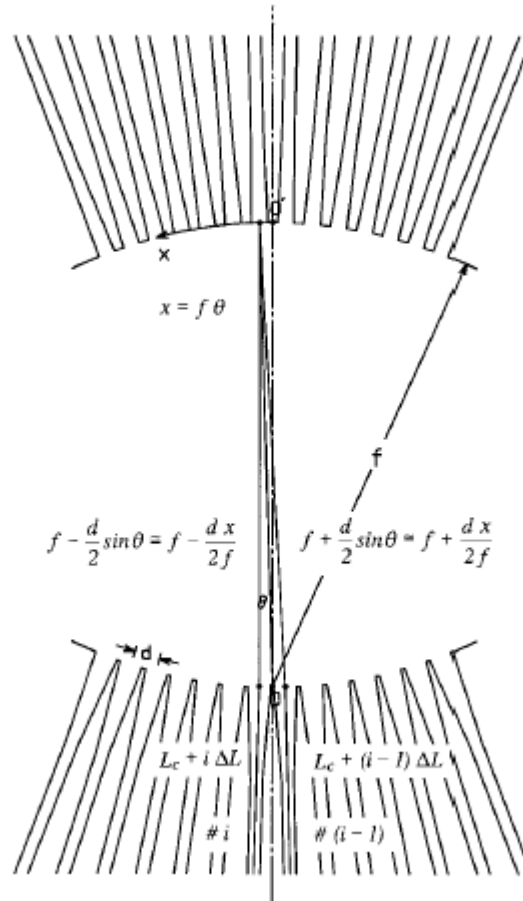


Figure 2.1c. Enlarged view of the output coupler [8].

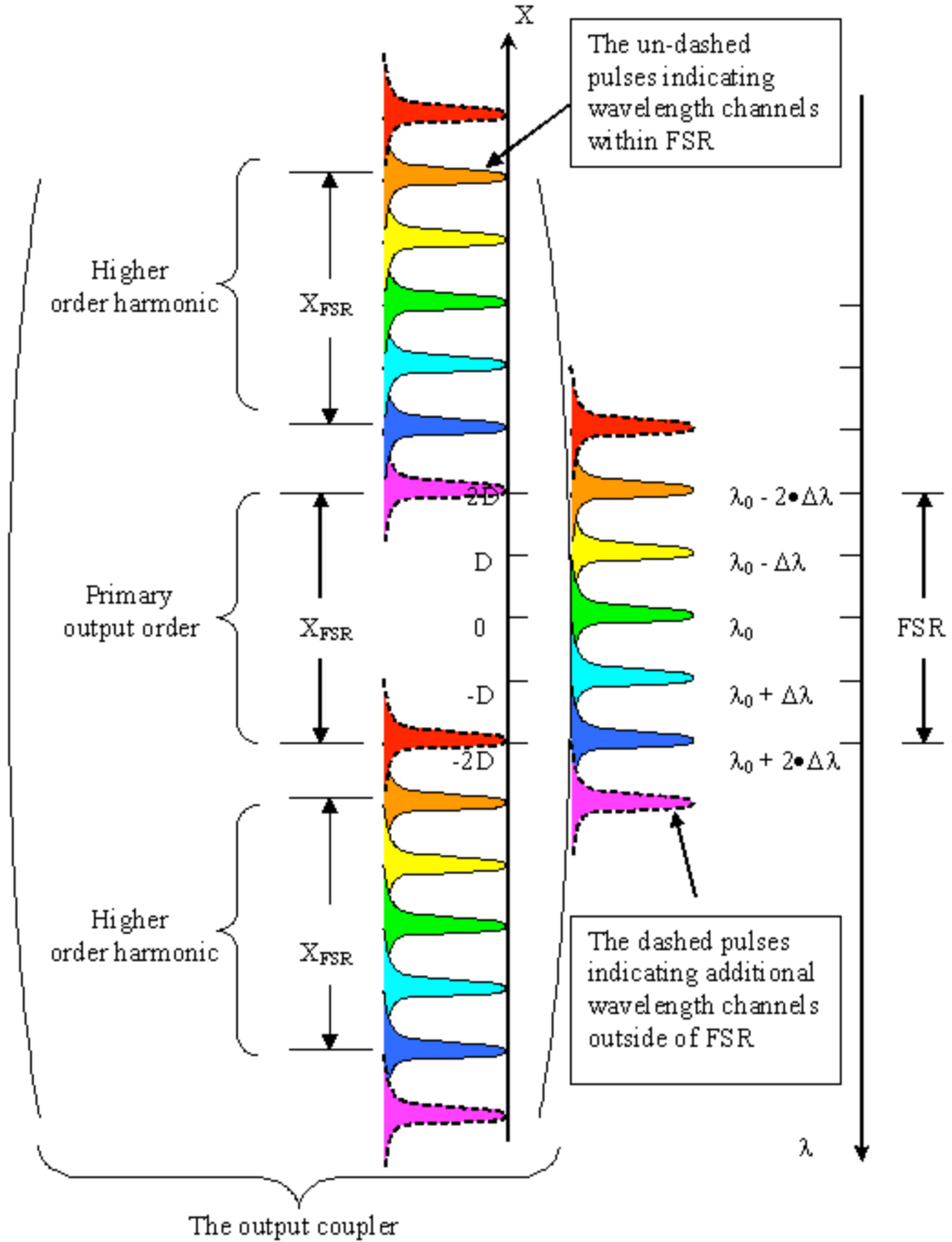


Figure 2.2. FSR of the regular AWG: the output coupler is shown here, $D=20\mu\text{m}$, $\Delta\lambda=1.6\text{nm}$.

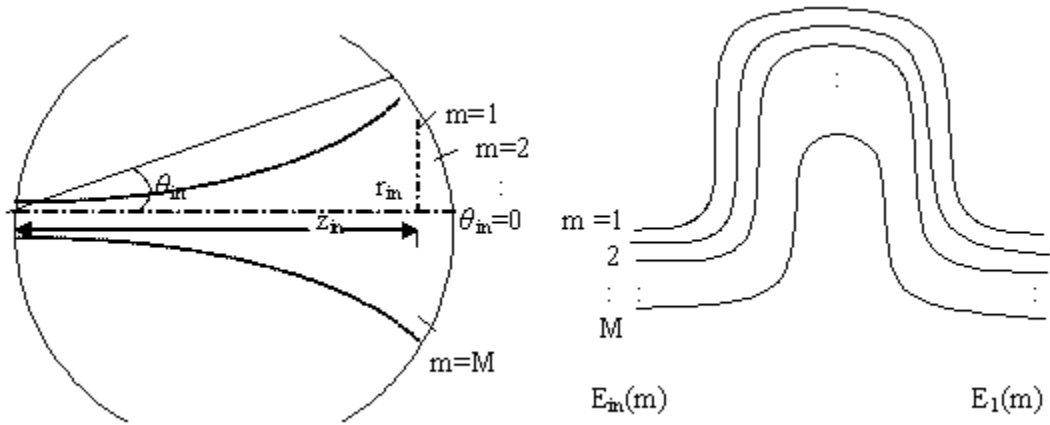


Figure 2.3.a. A diagram of input coupler and arrayed waveguides.

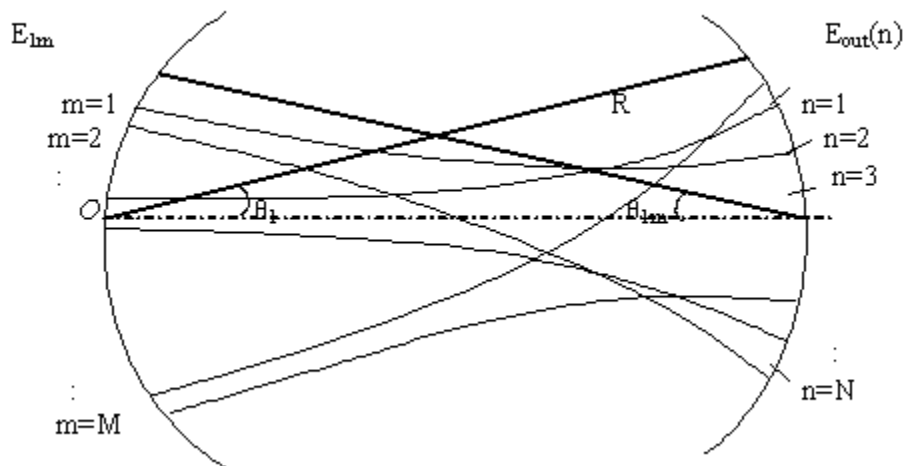


Figure 2.3.b Output coupler input-output diagram.

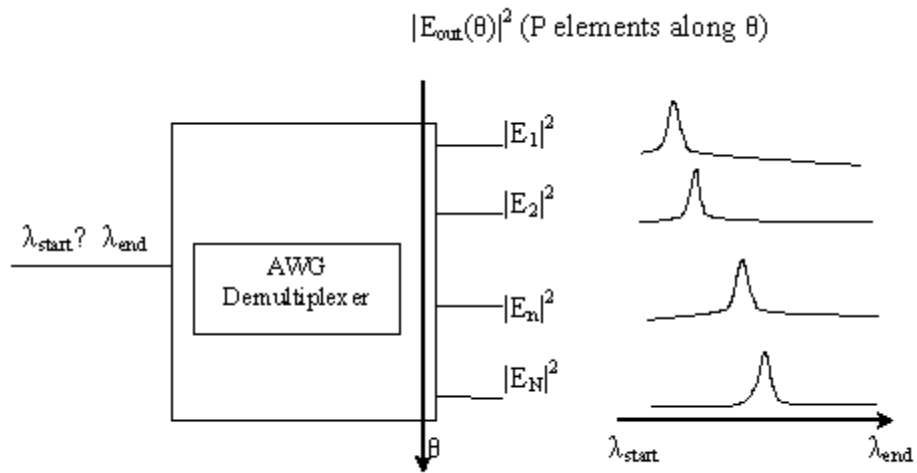


Figure 2.4.a Obtaining Transmission Spectrum of an AWG.

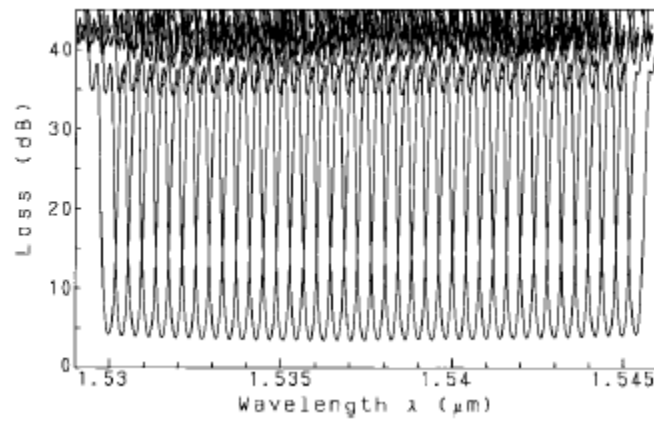


Figure 2.4.b Example of an AWG Transmission Spectrum [38].

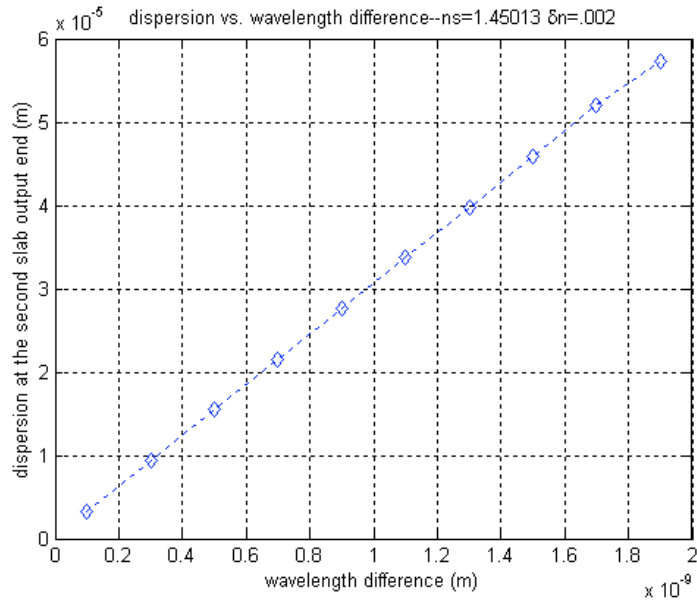


Figure 2.5. AWG output dispersion as a function of wavelength separation ($m=100$).

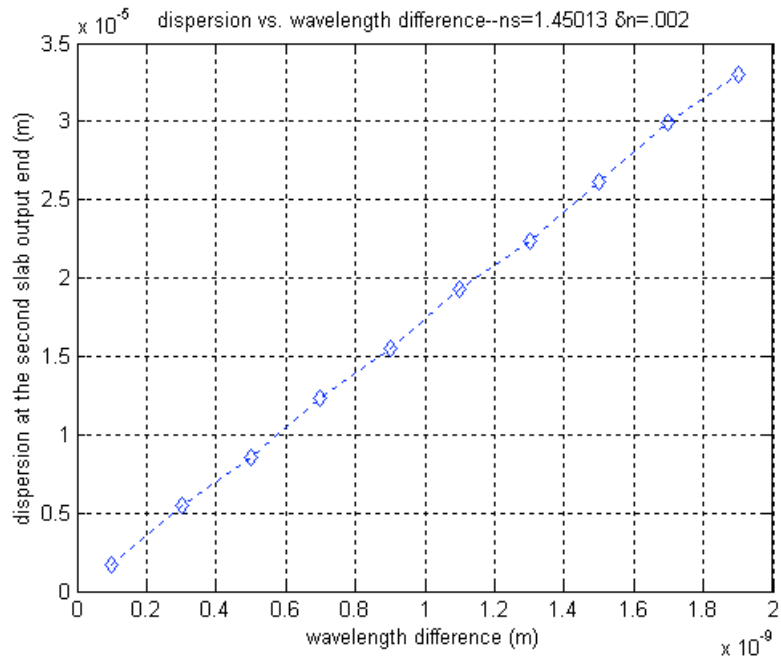


Figure 2.6. AWG output dispersion as a function of wavelength separation ($m=60$).

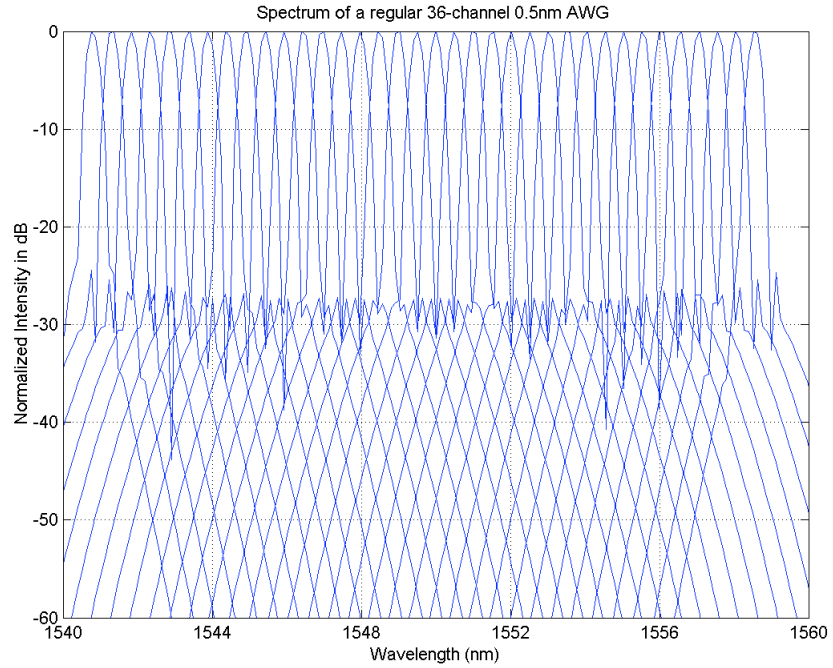


Figure 2.7. An AWG 36 channel demultiplexing output in spatial coordinates.

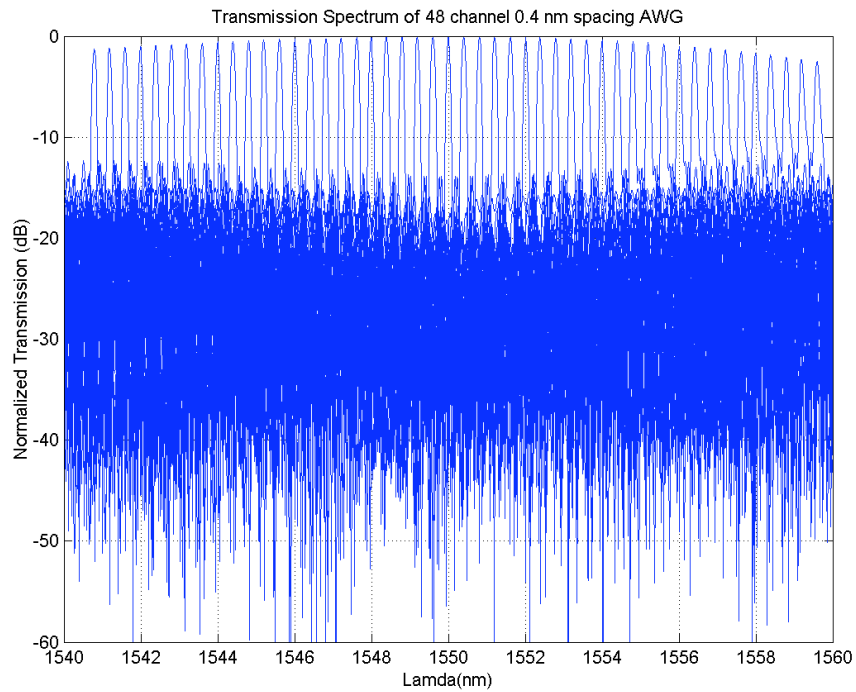


Figure 2.8.a. Transmission spectrum of a 48-channel-0.4 nm spacing ISZC AWG.

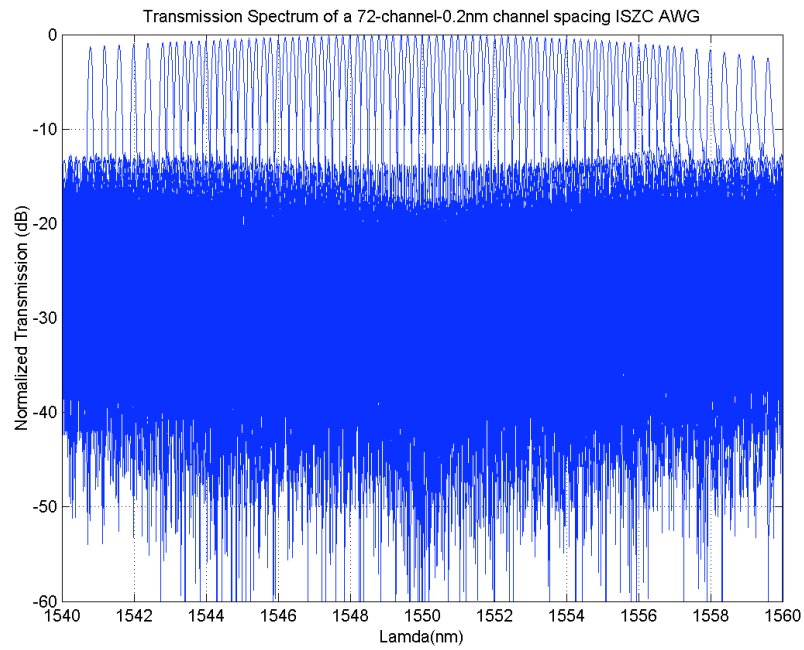


Figure 2.8.b. Transmission spectrum of 72-channel-0.2 nm spacing ISZC AWG

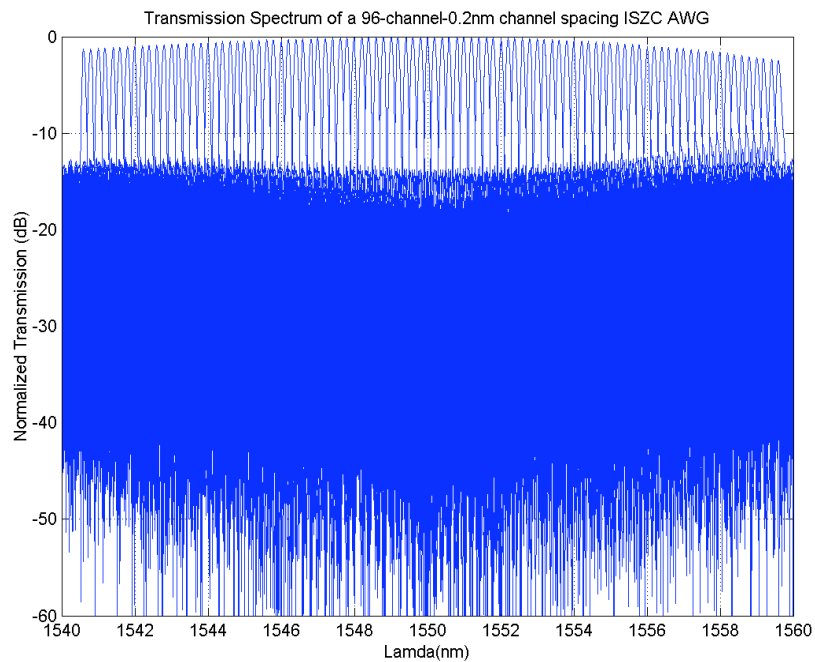


Figure 2.8.c. Transmission spectrum of a 96-channel ISZC AWG.

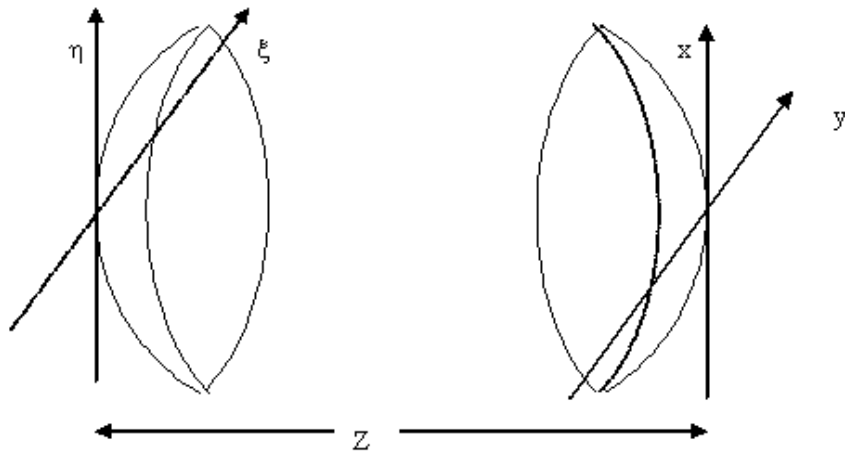


Figure 2.9. The confocal geometry

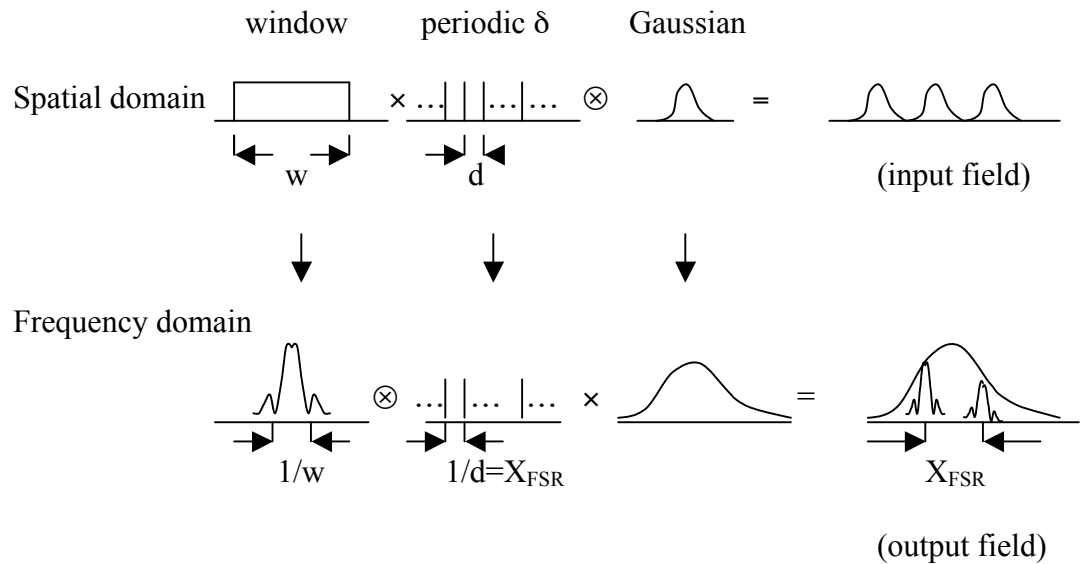


Figure 2.10. Spatial and frequency domain conversion in the output coupler.

3. METHOD OF IRREGULARLY SAMPLED ZERO CROSSINGS FOR WAVELENGTH DEMULTIPLEXING

The Method of Irregularly Sampled Zero Crossings (MISZC) modifies the array of waveguides sandwiched between the input and output couplers (free propagation ranges), whose function is to couple the light in and out of the arrayed waveguides. MISZC can be understood as a combination of zero crossing sampled phased array and irregular sampled phased array techniques applied to wavelength demultiplexing. The combined approach for phased array wavelength demultiplexing has its roots in holography. Holography is a technique that reconstructs an image by recording the interference pattern of an image and a reference wave on a hologram. When the same reference wave is applied on the hologram again, the original image can be reconstructed. In general, the hologram can be considered as a modulation of the reference wave by the object wave, and the modulation produces a wavefront at the output of the hologram. The lengths of arrayed waveguides provide effective phase modulation of the reference wave. This modulation is designed using a zero crossing method to provide the image (a single focal point) at the desired location. The linear increase of the lengths of the arrayed waveguides shifts the image locations according to their wavelengths. To illustrate the development of the MISZC, we start from fundamental holography equations and then Ersoy's [8, 10] equations for one-image-only derivation. This is followed by a derivation of the dispersion relation for wavelength demultiplexing. After that, the implementation of irregular sampling and zero crossing for wavelength demultiplexing is discussed in more detail. The major benefit of the ISZC phased array is the elimination of higher order diffractions. As a result, when more wavelength channels are added at the demultiplexer input, there is no overlapping between the fundamental output and higher order diffractions. In other words, the Free Spectral Range (FSR) related to regular grating device is theoretically extended to infinity; nevertheless in actuality the power in the eliminated higher order diffractions converts to noise. Therefore, there is a limit to the number of wavelength channels the ISZC phased array can accommodate in order to keep

the noise at a tolerable level. However, the experiments reported in later chapters indicate that noise does not increase much when the number of channels increases. There are two mechanisms that could generate higher order harmonics. One is the phase quantization and the symmetry of images for a plane wave input [8]; the second is due to the regular sampling of the input wavefront. Spherical reference wave, zero-crossings of phase, and irregular sampling are used to eliminate multiple hologram outputs in the MISZC. In this work, Ersoy's results are further extended to include the effect of linear phase term related to the lengths of arrayed waveguides. The irregularly sampled phased arrays were studied in the past for radar applications [26-31]. The effect of eliminating high harmonics due to irregular sampling is shown by a probabilistic analysis later in this chapter. Monte Carlo simulations confirm this analysis. At the end, simulation results are presented for MISZC wavelength demultiplexing. They show excellent agreement with the theoretical analysis.

3.1 Holography Basics

Holography was invented by Gabor [21] in 1948. The objective is to construct a desired wavefront by recording the intensity of the interference pattern of the desired wavefront ϕ_0 with a reference wavefront ϕ_r .

$$I = |\phi_0 + \phi_r|^2 = |\phi_0|^2 + |\phi_r|^2 + \phi_0^* \phi_r + \phi_0 \phi_r^* \quad (3.1)$$

The recording is then illuminated by the reference wave ϕ_s , and the reconstruction wavefront ϕ becomes

$$\phi \propto \left(|\phi_0|^2 + |\phi_r|^2 \right) \phi_s + \phi_r \phi_s \phi_0^* + \phi_r^* \phi_s \phi_0 \quad (3.2)$$

The first term is the intensity of the desired wavefront and the reference wavefront which is considered as noise, the second term records ϕ_0^* , and the third term records ϕ_0 . Gabor chose $\phi_r = \phi_s$ in his original work, yielding a real image and a virtual image overlapping each other. Leith and Upatnieks used an off-axis reference wave to separate the real and the virtual image as follows [2],

$$\phi_r = \phi_s = A e^{jk(\alpha x + \beta y + \gamma z)} \quad (3.3)$$

where A is the amplitude, $k=2\pi/\lambda$, λ is the wavelength, and α , β , and γ are the direction

cosines. Then, equation (2) can be written as

$$\phi \propto \left(|\phi_0|^2 + A^2 \right) \phi_s + A e^{2jk(cx+\beta y+\gamma z)} \phi_0^* + A^2 \phi_0 \quad (3.4)$$

In computer-generated holograms, a hologram is designed by computation and coding of amplitude and phase in an array of sampled phasefront. Given the reference wave, this usually involves two steps: 1) deciding the sampling points used for the object and hologram fields, 2) computing the hologram field at the sampling points given the object field. Usually either the Fourier hologram or the Fresnel hologram is used depending on whether a lens is used in the reconstruction process. Both types of holograms are usually computed by using the Fast Fourier Transform, for which the hologram field is sampled using a periodic spacing lattice structure [23]. During reconstruction, the reference wave is modulated by the hologram, and after going through the diffraction process, the image field is generated. Various methods have been introduced to encode the hologram [24, 25]. The nonlinear encoding process and periodic sampling of the hologram resulted in multiple images produced in the reconstruction process [8, 10]. The ISZC was developed by Ersoy in the late 1970's. It was originally called one-image-only holography. The algorithm calculates the locations of the aperture points such that the modulated reference wave emanating from the hologram apertures add up in phase at the desired object points. The ISZC method is non-periodic, and it is also a technique for phased array encoding. This hologram method is investigated in the thesis under wavelength demultiplexing context to examine the locations of possible higher order harmonics, and how they are filtered out of the region of interest.

3.2 One-Image-Only Holography

The algorithm for One-Image-Only holography is illustrated here following the development in the original paper [8]. If (x_o, y_o, z_o) is the observation point, and (x_i, y_i, z_i) is the position of a phase-shifting aperture, the Huygens-Fresnel principle for a collection of N apertures on a plane ($z=0$) leads to

$$U(x_o, y_o, z_o) = \sum_i^N \iint U(x_i, y_i, z_i) \frac{1}{j\lambda} \frac{\exp(jkr_{oi})}{r_{oi}} \cos \delta \cdot dx_i dy_i \quad (3.5)$$

where δ is the angle between the z -axis and the vector from the center of the aperture to

the observation point whose length is r_{oi} , λ is the wavelength, and k is the wavenumber.

For small hologram dimensions, $\cos(\delta)$ can be assumed to be constant. If the phase variations on the hologram plane are also small compared to the phase variations of $\exp(jkr_{oi})$, the above equation can be approximated by

$$U(x_o, y_o, z_o) = \frac{\cos \delta}{j\lambda R} d_x d_y \sum_i^N U(\theta_i) \iint \frac{\exp(jkr_{oi})}{r_{oi}} dx_i dy_i \quad (3.6)$$

where θ_i is the phase shift of the reference wave at the i^{th} aperture.

Assume that each aperture is rectangular on the x-y plane with dimensions d_x and d_y , and has a central point $(x_{si}, y_{si}, 0)$ whose radial distance from the observation point is given by

$$kr_{oi} = 2\pi n + \theta_i \quad n = \text{integer} \quad (3.7)$$

using far field approximation [23,10], the source field at the apertures can be considered as point sources approximated by narrow sinc functions. Thus, the integral in Equation (3.6) turns to a double summation.

$$U(x_o, y_o, z_o) = \frac{\cos \delta}{j\lambda R} d_x d_y \sum U(\theta_i) \exp(j\theta_i) \text{sinc} \left(\frac{X_i d_x}{\lambda r_{oi}} \right) \text{sinc} \left(\frac{Y_i d_y}{\lambda r_{oi}} \right) \quad (3.8)$$

where

$$X_i = x_o - x_{si}$$

$$Y_i = y_o - y_{si}$$

$$R = \text{average value of } r_{oi}$$

if all θ_i are set equal to θ , and $x_i, y_i \ll r_{oi}$, the sinc functions can be replaced by 1, and

$$U(x_o, y_o, z_o) = \left[\frac{U(x_o, y_o, z_o, \theta) \cos \delta}{j\lambda R} \right] d_x d_y N e^{j\theta} \quad (3.9)$$

Therefore, the amplitude of the field will be proportional to $d_x d_y N$, and its phase will be θ for a plane wave incident on the hologram at a right angle, an on-axis plane wave. If the incoming wave has phase variations on the hologram, its phase being Φ_i at each hologram point, then Equation (3.7) should be written as

$$kr_{oi} + \Phi_i = 2\pi n + \theta_i \quad n = \text{integer} \quad (3.10)$$

We can choose the aperture locations (x_i, y_i) , such that the resulting θ_i will be a constant. An object point is then obtained since all wavefronts generated by the hologram apertures

will add up in phase at the specified object point location. It can be written as

$$\varphi(x_i, y_i) + kr_{oi} = 2n\pi + \phi_0 \quad (3.11)$$

$\varphi(x_i, y_i)$ is the phase shift caused by the wave propagation from the origin of the reference wave front (x_c, y_c, z_c) to the hologram plate apertures (x_i, y_i) ; kr_{oi} is the phase shift caused by the wave propagation from the apertures (x_i, y_i) on hologram plate to the focal point (object point) located at (x_o, y_o, z_o) .

The most common types of reference waves are plane waves and spherical waves.

For a plane wave $\phi_r = Ae^{jk(\alpha x + \beta y + \gamma z)}$, $\varphi(x_i, y_i)$ is given as

$$\varphi(x_i, y_i) = k(\alpha x + \beta y + \gamma z) \quad (3.12.a)$$

For a divergent spherical wave originating at (x_c, y_c, z_c) as shown in Figure 3.1, $\varphi(x_i, y_i)$ is given by

$$\varphi(x_i, y_i) = kr_{ci} \quad (3.12.b)$$

$$r_{ci} = \sqrt{(x_c - x_i)^2 + (y_c - y_i)^2 + z_c^2} \quad (3.12.c)$$

The spherical reference wave is an approximation of the Gaussian wavefront from the output of a single mode waveguide. However, when far field diffraction is concerned the approximation is quite accurate. In our work for wavelength demultiplexing, the focal plane is located in the far field region. Therefore the divergent spherical wave is a reasonable assumption to start in the following derivation. The geometry of one-image-only digital holography design is shown in Figure 3.1. In the following, we examine a phased array demultiplexing design based on the one-image-only analysis for digital holography.

3.3 The Dispersion Relation for Zero Crossing Phased Array Wavelength Demultiplexing

The zero crossing phased array uses the arrangement very similar to the AWG demultiplexer. Figure 3.2.a below is a sketch of the design. A single mode waveguide is used to bring in the multi-wavelength input. The wavefront from the input waveguide diffracts in the free propagation region (the input coupler). Light wave is coupled to an array of waveguides. Then, the output wavefront from the phased array waveguides goes

through another diffraction process in the second free propagation region (the output coupler). The major departure from the regular AWG design is the placement of the phased array waveguides and special care with phase used for modulation. The arrayed waveguides are not evenly spaced as in AWG design, yet their lengths still incorporate linear increase with respect to the displacement of apertures on the interface with the output coupler, in addition to a length perturbation due to the spherical reference wave.

The waveguide coupling aperture placements on both of the interfaces between the arrayed waveguides and the couplers are the same. In principle this symmetry is not necessary, and asymmetric design of waveguide placement can provide another degree of freedom. This feature could be explored in the future work. Currently, we restrict ourselves to identical aperture placement on both interfaces. The output field emanating from the single-mode input waveguide can be accurately modeled by a spherical wave originating from the end of the input waveguide. The additional consideration is the dispersion provided by the phased array waveguides as a function of wavelength.

There are practical obstacles to implementing the couplers as shown in Figure 3.2.a. Consider the figure shown above, in the input coupler, when the wavefront impinges on the end of the coupler, the phase varies fast along the flat surface. The errors in waveguide placement on the interface due to fabrication can result in large phase errors. It is difficult to determine and correct this error. Borrowing from conventional AWG design, the coupler's end is changed to a circular surface matching the spherical wave as shown in Figure 3.2.b. The spherical wave is then implemented by adjusting the lengths of the arrayed waveguides.

Zero crossings refer to points at which phases are zero or multiples of 2π . The general equation for zero crossing phased array design using spherical reference wave is given as [6]

$$\varphi(x_i, y_i) + \theta(x_i, y_i) + k^1 r_{oi} = 2n\pi + \phi_0 \quad (3.13)$$

where ϕ_0 is set to equal to zero for zero crossings, k is the propagation constant in free space, corresponding to Figure 3.1, $\varphi(x_i, y_i)$ is the phase shift caused by the wave propagation from the origin of the spherical reference wave (x_c, y_c, z_c) to the i^{th} aperture (x_i, y_i) on the hologram. The zero crossing model in Equation (3.13) is implemented in

waveguides for ISZC AWG shown in Figures 3.2.b, and 3.2.c. For the i^{th} waveguide, $\varphi(x_i, y_i)$ is computed by

$$\varphi(x_i, y_i) = k_w^m r_{1ci} \quad (3.14.a)$$

$$r_{1ci} = \frac{r_{ci}}{n_c} \quad (3.14.b)$$

where r_{1ci} is the distance from the origin of the spherical reference wave front (x_c, y_c, z_c) to the waveguide aperture locations (x_i, y_i) incorporated in the arrayed waveguide for the center wavelength λ_1 ; and k_w^m is the propagation constant inside the waveguide for m^{th} wavelength λ_m , n_c is index of refraction of the waveguide for the center wavelength λ_1 . For convenience r_{ci} is used in place of r_{1ci} in rest of the thesis. Whenever the r_{ci} notation may cause confusion, a special note will be given.

$\alpha(x_i, y_i)$ is the spatial dependent linear phase shift corresponding to linear length increase in subsequent AW's designed for regular AWG's. For the i^{th} waveguide; therefore we have,

$$\theta(x_i, y_i) = k_w^m x_i \alpha \quad (3.14.c)$$

l_i is the length of the i^{th} waveguide as follows:

$$l_i = x_i \alpha + r_{ci} + r_{oi} + L_c \quad (3.14.d)$$

α is a constant, x_i is the displacement of the i^{th} coupling aperture on the interface between the propagation region and the waveguide. $k^1 r_{oi}$ is the phase shift caused by the wave propagation from the apertures (x_i, y_i) to the focal point (object point) located at (x_o, y_o, z_o) , where r_{oi} is the distance from the interfacing aperture (x_i, y_i) to the focal point (x_o, y_o, z_o) in the second free propagation region. They are given by

$$r_{oi} = \sqrt{(x_o - x_i)^2 + (y_o - y_i)^2 + z_o^2} \cong z_o + \frac{x_o^2 + y_o^2 + x_i^2 + y_i^2}{2z_o} - \frac{x_o x_i + y_o y_i}{z_o} \quad (3.15)$$

$$r_{ci} \cdot n_c = \sqrt{(x_c - x_i)^2 + (y_c - y_i)^2 + z_c^2} \cong z_c + \frac{x_c^2 + y_c^2 + x_i^2 + y_i^2}{2z_c} - \frac{x_c x_i + y_c y_i}{z_c}$$

So applying Equation (3.13) for the center wavelength λ_1 , for which the apertures locations x_i are designed, ignoring the common waveguide length L_c , we can write

$$k_w^1 r_{ci} + k_w^1 x_i \alpha + k^1 r_{oi} = 2n\pi \quad (3.16)$$

Substituting r_{oi} and r_{ci} in the above, and effective index inside waveguide $n_c = k_w^1/k^l$, we get

$$n_c x_i \alpha - x_i \left(\frac{x_c}{z_c} + \frac{x_o}{z_o} \right) - y_i \left(\frac{y_c}{z_c} + \frac{y_o}{z_o} \right) + \left(\frac{x_i^2 + y_i^2}{2} \right) \left(\frac{1}{z_o} + \frac{1}{z_c} \right) = n\lambda - F_{oc}$$

where

$$F_{oc} = z_o + \frac{x_o^2 + y_o^2}{2z_o} + z_c + \frac{x_c^2 + y_c^2}{2z_c} \quad (3.17)$$

The terms F_{oc} represent constant phase, and can be neglected without changing final conclusions. Let

$$n_c \alpha = \delta \quad (3.18)$$

Then, Equation (3.17) for general wavelength λ_m can be simplified as

$$x_i \delta - x_i \left(\frac{x_c}{z_c} + \frac{x_o}{z_o} \right) + \frac{x_i^2}{2} \left(\frac{1}{z_o} + \frac{1}{z_c} \right) = n\lambda_m \quad (3.19)$$

Now we apply Equation (3.19) to wavelength λ , and λ' to compute the dispersion at the output focal plane where wavelength demultiplexing occurs.

$$\begin{aligned} x_i \delta - x_i \left(\frac{x_c}{z_c} + \frac{x_o}{z_o} \right) + \frac{x_i^2}{2} \left(\frac{1}{z_o} + \frac{1}{z_c} \right) &= n\lambda \\ x_i \delta - x_i \left(\frac{x_c}{z_c} + \frac{x_o'}{z_o'} \right) + \frac{x_i^2}{2} \left(\frac{1}{z_o'} + \frac{1}{z_c} \right) &= n\lambda' \end{aligned} \quad (3.20)$$

where x_o' and z_o' constitute the location of the new focal point. $x_i \delta$ is the linear phase shift related to the i^{th} waveguide and placed at i^{th} aperture location x_i . Since the image wavefront at distance z_o away is close to a Fourier transform of the original object wave. A linear phase-shift with respect to spatial variable of the object wave produces linear displacement in the spatial frequency domain after Fourier transform. According to the diffraction theory, the image plane spatial variable is a scaled version of the spatial frequency variable of the object plane. If $f(x)$ is a spatial function in the object plane and x is the spatial variable, $F(f_x)$ is the corresponding Fourier transform. Applying a linear

phase modulation proportional to the spatial variable to the object wave, the object wave becomes $f(x)\exp(j\delta x)$. Taking Fourier transform, we have $\text{FT}\{f(x)\exp(j\delta x)\} = F(f_x - \delta/2\pi)$, And f_x is the spatial frequency variable of the object wave as well as the scaled spatial variable of the image plane y , $f_x = \frac{y}{\lambda z_o}$. If δ is linearly dependent on wavelength, the task of wavelength demultiplexing is accomplished on the image plane. A more detailed treatment is provided in Chapter 5.

After taking the ratio of the two equations in Equation (3.20), we have

$$\frac{x_i \left(\delta - \frac{x_c}{z_c} - \frac{x_o}{z_o} \right) + \frac{x_i^2}{2} \left(\frac{1}{z_o} + \frac{1}{z_c} \right)}{x_i \left(\delta - \frac{x_c}{z_c} + \frac{x_o'}{z_o'} \right) + \frac{x_i^2}{2} \left(\frac{1}{z_o'} + \frac{1}{z_c} \right)} = \frac{\lambda}{\lambda'} = R \quad (3.21)$$

$$x_i \left(\delta - \frac{x_c}{z_c} - \frac{x_o}{z_o} \right) + \frac{x_i^2}{2} \left(\frac{1}{z_o} + \frac{1}{z_c} \right) = R x_i \left(\delta - \frac{x_c}{z_c} - \frac{x_o'}{z_o'} \right) + R \frac{x_i^2}{2} \left(\frac{1}{z_o'} + \frac{1}{z_c} \right) \quad (3.22)$$

In Equation (3.22) the location of the apertures (x_i, y_i) are fixed. The only way to satisfy this equation is to equate the corresponding terms of powers of x_i . So we have

$$\frac{R}{z_o'} + \frac{R}{z_c} = \frac{1}{z_o} + \frac{1}{z_c} \quad (3.23.a)$$

$$R \left(\delta - \frac{x_c}{z_c} - \frac{x_o'}{z_o'} \right) = \delta - \frac{x_c}{z_c} - \frac{x_o}{z_o} \quad (3.23.b)$$

Solving the above system, we obtain the new focal point (x_o', z_o') as

$$z_o' = \frac{R}{\frac{1-R}{z_c} + \frac{1}{z_o}} \approx R z_o \quad (3.24.a)$$

$$x_o' = \frac{\frac{x_o}{z_o} - (1-R) \left(\delta - \frac{x_c}{z_c} \right)}{\frac{1-R}{z_c} + \frac{1}{z_o}} \approx x_o - z_o (1-R) \left(\delta - \frac{x_c}{z_c} \right) \quad (3.24.b)$$

given $1-R \approx 0$, and $z_c \ll z_o$

From the above derivation we see that the focal point location z_o' is very close to the original z_o . This indicates that the focal points for different wavelength components are focused relatively close in z direction i.e. on the same z -plane, which is desirable for wavelength demultiplexing. Since the wavelength induced dispersion is proportional to x , the output is demultiplexed in x -axis according to wavelength. The dispersion relationship is given as

$$\Delta x = x'_0 - x_0 \approx -z_0 (1 - R) \left(\delta - \frac{x_c}{z_c} \right) = -z_0 \frac{\Delta \lambda}{\lambda'} \left(\delta - \frac{x_c}{z_c} \right) \quad (3.25)$$

3.4 A Practical Algorithm for the Irregularly Sampled Zero Crossing Phased Array Wavelength Demultiplexing

Zero crossings are points on the interfaces of IC/AW and AW/OC, through which the light wave of the center wavelength accumulate phases of integer multiples of 2π . This algorithm starts with an initial guessing point, after that the phase error is calculated, then using the phase error, the true zero crossing is determined by calculating the displacement from the true zero crossing to the initial guessing point. There are three major steps for a practical implementation of MISZC wavelength demultiplexing. Firstly, an array of points is placed on a uniform grid. Secondly, a vector of random numbers is generated to give a shift to each point placed on the grid, and these points are used as initial guesses for zero crossings. Thirdly, using a computation algorithm to find a correction for each guessing point and then, add the correction to the respective point. Both the design algorithm and the computation algorithm are discussed in detail in the following.

3.4.1 Design algorithm

The three major steps are illustrated in the following diagrams. In Figure 3.3.a, a series of points x_i 's are placed on a uniform grid with a fixed separation of Δx . In Figure 3.3.b a series of random numbers u_i 's, uniformly distributed between 0 and 1 are generated. The u_i 's are multiplied by Δx and added to x_i 's. So the initial estimates for zero crossings can be written as,

$$x_i = \Delta x \cdot i + u_i \cdot \Delta x \cdot \eta \quad (3.26)$$

where

η : controls the degree of randomness, $\eta \in (0,1)$

i is an integer, $i = 0, 1, 2, 3, \dots, N-1$;

N is the number of zero crossing points;

u_i is a random number uniformly distributed in $(0, 1)$.

In Figure 3.3.c the correction Δ_i 's are found and added to x_i 's. The corrected zero crossing coordinate is x_i' . So we have,

$$x_i' = x_i + \Delta_i \quad (3.27)$$

where Δ_i is the correction term for the i^{th} estimate x_i .

3.4.2 Calculation of the coordinates for sampling points

To calculate the correction term Δ_i , using Equation (14) and (16.b), considering the x_i as the guessing point, and x_i' as the zero crossing point, we can write

$$r_{ci} + x_i \delta + r_{oi} = n\lambda + \phi_i \lambda / 2\pi \quad (3.28)$$

$$r_{ci}' + x_i' \delta + r_{oi}' = n\lambda \quad (3.29)$$

where r_{ci}' , r_{oi}' are prime version of r_{ci} and r_{oi} replacing x_i with x_i' .

Since x_i is the guessing point, the residue phase at the focal point for the wavefront propagate through x_i is ϕ_i . However, the x_i' is the zero crossing so residue phase is a constant ϕ_0 for all zero crossings x_i' . Let $\phi_0 = 0$. The residue phase ϕ_i can also be found simply. Subtracting Equation (26) from (25), we have

$$r_{ci} + x_i \delta + r_{oi} = r_{ci}' + r_{oi}' + x_i' \delta - B \quad (3.30)$$

where $B = -\phi_i \lambda / 2\pi$.

Simplifying Equation (27) and squaring both sides yields

$$(r_{ci}' + r_{oi}')^2 = (r_{ci} - \delta \Delta + r_{oi} + B)^2 \quad (3.31)$$

We expand r_{ci}' and r_{oi}' as follows:

$$\begin{aligned} r_{oi}' &= \sqrt{(x_o - x_i')^2 + z_o^2} = \sqrt{(x_o - x_i - \Delta)^2 + z_o^2} = \sqrt{r_{oi}^2 - 2\Delta X_c + \Delta^2} \\ r_{ci}' &= \sqrt{(x_c - x_i')^2 + z_c^2} = \sqrt{(x_c - x_i - \Delta)^2 + z_c^2} = \sqrt{r_{ci}^2 - 2\Delta X_o + \Delta^2} \end{aligned} \quad (3.32)$$

Defining

$$X_c = x_c - x_i$$

$$X_o = x_o - x_i$$

we get

$$\begin{aligned} & \left(r_{oi}^2 - 2\Delta X_o + \Delta^2 \right) \left(r_{ci}^2 - 2\Delta X_c + \Delta^2 \right) \\ & = \left[r_{ci}r_{oi} + \frac{B^2}{2} - B(r_{ci} + r_{oi}) + \frac{(\delta\Delta)^2}{2} - (r_{ci} + r_{oi} - B)\delta\Delta \right]^2 \end{aligned} \quad (3.33)$$

We write this equation as a polynomial in powers of Δ as

$$\Delta^4 C_4 + \Delta^3 C_3 + \Delta^2 C_2 + \Delta C_1 + C_0 = 0 \quad (3.34)$$

where,

$$\begin{aligned} C_4 &= G_1^2 - 1 \\ C_3 &= 2G_1G_2 + 2X_c + 2X_o \\ C_2 &= G_2^2 + 2G_1G_3 - 4X_cX_o - r_{oi}^2 - r_{ci}^2 \\ C_1 &= 2G_2G_3 + 2X_cr_{oi}^2 + 2X_or_{ci}^2 \\ C_0 &= G_3^2 - r_{oi}^2r_{ci}^2 \end{aligned} \quad (3.35)$$

and

$$\begin{aligned} G_1 &= \left(\frac{\delta^2}{2} - 1 \right) \\ G_2 &= -(r_{ci} + r_{oi} - B)\delta + (X_c + X_o) \\ G_3 &= r_{ci}r_{oi} + \frac{B^2}{2} - B(r_{ci} + r_{oi}) \end{aligned} \quad (3.36)$$

When Δ is solved using Equation (3.34), the correction to the zero crossing estimates is found, and the true zero crossing is located.

3.5 Elimination of High Order Harmonic Diffractions

Having discussed the algorithm of ISZC AWG design, in this section, we show the effectiveness of the ISZC AWG in eliminating higher order harmonic diffractions through a rigorous derivation. As it is mentioned at the beginning of this chapter, the major benefit of ISZC phased array is the elimination of high order harmonic diffractions. This feature enables ISZC modified AWG to provide more wavelength channels. The

modification only makes slight adjustments in the placement and length of arrayed waveguides. The cost of having an infinite FSR is the increased but tolerable noise level, since the power in the eliminated high order diffractions is scattered as background noise. As a result, given almost identical physical size of the modified AWG and original AWG, the modified AWG can add considerably many more wavelength channels until the output intensity drops at the edge of the output spectrum due to diffraction limit. There are two mechanisms that produce high order harmonic diffractions in AWG devices. The first cause is the nature of the zero-crossing method rooted in hologram, which can cause multiple output images when a plane wave is used as the reference wave to encode the hologram. The origin and solution to multiple output images generated in the hologram image reconstruction is discussed in detail by Ersoy [8]. The spherical reference wave and zero-crossings of phase are used to shift the high order diffractions away from the fundamental image in hologram image reconstruction. Around the location of the fundamental image, the high order diffractions are scattered as background noise. The second cause is the periodic sampling of the input wavefront by the linearly spaced arrayed waveguide placement. The sampling theory indicates periodic sampling produces repetitions of desired spectrum at reconstruction. Irregular sampling eliminates higher order diffractions of this nature by turning them also to background noise. Irregular sampling is also known to generate better quality beams with reduced grating lobes and lower side lobe levels [26-31]. Closed-form analysis on random sub-array grating power is presented in [28]. The grating power is found to be reduced compared to the uniformly spaced arrays. A Green's function based treatment is presented for the unequally spaced arrays on circular curvatures [26]. In this chapter, a probabilistic analysis is carried out for the irregularly (randomly) placed array elements with uniform distribution on a circular arc.

3.5.1 Eliminating Higher Order Diffractions By Zero Crossing Sampling

The origin of the higher order harmonics in zero-crossing sampling hologram with a spherical reference wave is a result of spatial symmetry on both sides of the hologram [4, 5], in that there are points that can be found satisfying the phase matching

condition, i.e. there are certain spatial locations that wavefront emanating from all apertures add up just as those designated focal points. These points tend to exist when the designated focal points are far away from the hologram, because further away from the hologram the phase variations among closely spaced points in the far field become slow, so that it's easier for phases to add up forming higher order harmonics. In the following, we closely examine the higher order harmonics when the multi-wavelength reference wave is applied to the grating assisted zero-crossing sampling hologram including a spherical reference wave.

From Equation (3.19), the focal points of high harmonics occur when the hologram equation satisfies

$$x_i \delta - x_i \left(\frac{x_c}{z_c} + \frac{x_o'}{z_o'} \right) + \frac{x_i^2}{2} \left(\frac{1}{z_o'} + \frac{1}{z_c} \right) = nm\lambda \quad (3.37)$$

where (x_o', z_o') is the focus of higher harmonics. Similarly to the procedure that gives the focal points for different wavelengths, we take the ratio of Equation (3.37) and the Equation (3.19) for the single wavelength. Thus we can write

$$\frac{x_i \left(\delta - \frac{x_c}{z_c} - \frac{x_o'}{z_o'} \right) + \frac{x_i^2}{2} \left(\frac{1}{z_o'} + \frac{1}{z_c} \right)}{x_i \left(\delta - \frac{x_c}{z_c} + \frac{x_o'}{z_o'} \right) + \frac{x_i^2}{2} \left(\frac{1}{z_o'} + \frac{1}{z_c} \right)} = \frac{1}{m} \quad (3.38)$$

Solving for x_o' and z_o' in a similar fashion, we obtain the higher order harmonic focal points for multiple wavelengths.

$$z_o' = \frac{1}{\frac{m-1}{z_c} + \frac{1}{z_o}} \approx \frac{z_c}{m-1} \quad (3.39.a)$$

$$x_o' = \frac{\frac{x_o}{z_o} - (m-1) \left(\delta - \frac{x_c}{z_c} \right)}{\frac{m-1}{z_c} + \frac{1}{z_o}} \approx \frac{x_o}{z_o} \frac{z_c}{m-1} - \left(\delta - \frac{x_c}{z_c} \right) z_c \quad (3.39.b)$$

given $z_c \ll z_o$

From the above equation, we can see a significant move of the focal points of high order diffractions in z direction, as $z_{o_}$ quickly shrinks as harmonic orders increase. This indicates the conversion of higher harmonic diffraction power to background noise in the image plane.

3.5.2 Eliminating Higher Order Diffractions By Irregular Sampling

The irregular phased array has been investigated in the past three decades in the radio and microwave regions. The optical regular phased array has been investigated in recent years. In regular phased arrays, in order to avoid multiple grating orders the spacing between the phase elements are required to be less than half the wavelength. For optical waves this requirement poses some serious challenges in fabrication [31]. The irregular phased array has been proposed to lessen the requirements on spacing between phase elements while still avoiding higher order grating lobes (harmonics) [18]. As alluded in the previous chapter, the higher order harmonics power in regular AWG's is caused by the periodic sampling of the wavefront through regular spacing of sampling points. Irregular sampling destroys the periodicity in the sampling process so that the higher order grating lobes are suppressed. The effect of irregular sampling has been known for sometime. There are iterative methods based on Monte Carlo simulation and analytical approaches to characterize the main grating lobe [27], but no detailed derivation has been found in the literature addressing the power of high order harmonics. In the following we present a detailed analysis of the effects of irregular sampling on higher order harmonics.

The location of the phased array elements will be assumed to be on a circular arc as shown in the diagram below. These elements are considered as point sources with same initial phase. The locations of the phased array elements $X_0, X_1, X_2 \dots X_N$, are specified by the radial angles $\theta_0, \theta_1, \theta_2 \dots$, and θ_N with respect to the center of the circle. These angles are randomly arranged. This assumption captures the essence of the diffraction process in the output coupler of an ISZC AWG. The locations of the phased array elements are at the end of the waveguides, and the length of waveguides can be designed to produce desired phase at their output. In the derivation, we first set up a

randomness measure η , which describes the degree of randomness for a particular selection of phased array element locations under examination. Then, we calculate where the high order harmonic peaks are located. Finally we show that the power at these locations vary as a function of the randomness measure η . At the largest degree of randomness, the peak power in high order harmonics is proportional to N . At the lowest degree of randomness, i.e. uniformly spaced phased array, the peak power in harmonics is proportional to N^2 . The result shows the coherence of the phased array output field is related to the degree of randomness in the placement of the phased array elements.

The arrangement is shown in Figure 3.4. The placement of the phase elements is not asymmetric. The arrangement can be generalized by rotating the coordinate system with respect to point O . The set up in Figure 3.4 is used to ease mathematical formulation. The circular arc presents the AW/OC interface. Since the output field around and beyond the y -axis is in the far field region, the focus in the far field has a line pattern. So the higher harmonic would also be lines crossing the y -axis. By finding field intensity across the y -axis, we can examine all harmonic peaks. Same as for a regular AWG, the primary focus, i.e. the zeroth order harmonic of the phase elements is the center of the circle. The θ_n 's are given as

$$\theta_n = n\theta + \eta \cdot u(0, \theta) \quad (3.40)$$

θ : a constant;

n : 0, 1, 2, ..., N ;

η : randomness measure, $0 \leq \eta \leq 1$;

u : a uniformly distributed random number, $0 \leq u \leq \theta$.

Therefore, as $\eta \rightarrow 0$, θ_n is uniformly spaced on the arc; as $\eta \rightarrow 1$, θ_n has the largest degree of randomness by the above definition.

Let $P(y)$ be the total field along y -axis resulting from wave propagation from the phased array. We can write

$$P(y) = \sum_{n=1}^N e^{j[\phi_n + k \cdot r_n(y)]} \quad (3.41)$$

ϕ_n is the initial phase of the n^{th} phase elements, as discussed previously. These phases can be adjusted to be integer multiples of 2π by giving the proper lengths of the waveguides for AWG applications. r_n is the distance from the n^{th} phase element to the point $(0,y)$. So,

$$P(y) = \sum_{n=1}^N e^{jk r_n(y)} \quad (3.42)$$

At $y=0$, we have $P(0) = N$.

As shown in Figure 3.5, to find $r_n(y)$, we can write

$$r_n(y) = \sqrt{(y + R \sin \theta_n)^2 + (R \cos \theta_n)^2} \quad (3.43)$$

Assuming $R \gg y$, $\sin \theta_n \ll 1$, applying paraxial approximation [23], we have

$$\begin{aligned} r_n(y) &= R \sqrt{1 + \frac{y^2 + 2R \cdot y \sin \theta_n}{R^2}} \\ &\cong R \left(1 + \frac{1}{2} \frac{y^2 + 2R \cdot y \sin \theta_n}{R^2} \right) \\ &= R + r'_n(y) \end{aligned} \quad (3.44.a)$$

where

$$r'_n(y) = \frac{1}{2R} (y^2 + 2R \cdot y \sin \theta_n). \quad (3.44.b)$$

We define

$$Q_n(y) = \frac{k}{2R} (y^2 + 2R \cdot y \sin \theta_n) \quad (3.45)$$

From Equation (3.44.b), we can write $P_n(y)$ as

$$\begin{aligned} P(y) &= \sum_{n=1}^N e^{jk[r'_n(y)+R]} \\ &= e^{jkR} \cdot \sum_{n=1}^N \exp(jQ_n(y)) \end{aligned} \quad (3.46)$$

Now we can calculate the locations of high order harmonic peaks. Consider uniform spacing case, $\theta_n = n \cdot \theta$. With $\eta=0$, and for small θ_n , we have

$$Q_n(y) = \frac{k}{2R} (y^2 + 2R \cdot y \sin \theta_n) = \frac{k}{2R} (y^2 + 2R \cdot y \cdot \theta_n) \quad (3.47)$$

Considering the m^{th} order harmonic, we get

$$Q_{n+1}(y) - Q_n(y) = 2m\pi \quad (3.48)$$

Using Equation (3.47), and (3.48), and solving for y ; the location of the m^{th} order harmonic peak Y_m is expressed as

$$Y_m = \frac{2\pi m}{k\theta} \quad (3.49)$$

To calculate the power at the peak of the high order harmonics for an irregular phased array, the total field at Y_m is given as

$$P(Y_m) = e^{jkR} \cdot \sum_{n=1}^N \exp(jQ_n(Y_m)) = A e^{jkR} \cdot \sum_{n=1}^N e^{jkY_m\theta_n} \quad (3.50)$$

where $A = e^{j\frac{k}{2R}Y_m^2}$

The power at Y_m can be written as

$$\begin{aligned} E\left[|P(Y_m)|^2\right] &= E\left[\left(\left|\sum_{n=1}^N \exp(jY_m\theta_n)\right|\right)^2\right] \\ &= E\left[\sum_{n=1}^N \Pi_n(Y_m)\Pi_n^*(Y_m)\right] + E\left[\sum_{i=1}^N \sum_{\substack{j=1 \\ j \neq i}}^N \Pi_i(Y_m)\Pi_j^*(Y_m)\right] \end{aligned} \quad (3.51)$$

$$\text{where } \Pi_i(Y_m) = \exp(jkY_m\theta_i) = \exp(jkY_m[\theta \cdot i + \eta \cdot u_i(\theta)]) \quad (3.52)$$

Assuming the random number u_n is identically and independently distributed, and taking the expectation operation inside the summation we have

$$E\left[|P(Y_m)|^2\right] = N + \sum_{i=1}^N \sum_{\substack{j=1 \\ j \neq i}}^N E[Q_i(Y_m)] \cdot E[Q_j^*(Y_m)] \quad (3.53)$$

Substituting $Y_m = \frac{2\pi m}{k\theta}$ in the above equation, we have

$$\begin{aligned} E[Q_i(Y_m)] &= E\left[e^{j\frac{2\pi m}{\theta}\eta u_i(\theta)}\right] \\ &= \int_0^\theta e^{j\frac{2\pi m}{\theta}\eta u} \frac{1}{\theta} du \\ &= \frac{1}{j2\pi\eta m} \left[e^{j2\pi\eta m} - 1\right] \end{aligned} \quad (3.54)$$

Defining $\text{sinc}(x) = \frac{\sin(\pi x)}{\pi x}$, we can write

$$E[\Pi_i(Y_m)]E[\Pi_j^*(Y_m)] = \sin^2(m\eta). \quad (3.55)$$

So the power at the m^{th} harmonic peak is

$$E[|P(Y_m)|^2] = N + (N^2 - N) \sin^2(m\eta). \quad (3.56)$$

As $\eta \rightarrow 0$, the phased array is uniformly spaced; the m^{th} harmonic power is given as the coherent vector sum of N phased array elements, and $E[|P(Y_m)|^2] = N^2$. As $\eta \rightarrow 1$, the spacing of phased array elements has the largest degree of randomness; the resulting power for the m^{th} harmonic is the sum of incoherent power addition of N phased array elements, and $E[|P(Y_m)|^2] = N$.

3.6 Simulation Results

A series of simulations are performed using Matlab to test the correctness of the zero crossing sampling using spherical reference waves, the dispersion relation for multi-wavelength inputs, and the elimination of high order harmonic powers by irregularly sampled phase arrays. A more detailed discussion of simulating the ISZC AWG in Matlab is presented in the following chapter. The results show very good agreement with theory.

3.6.1 Formation the Focal Points

In section 3.3 we discussed the focal point location of zero crossing phased array design using paraxial approximations [8]. This method can be used to eliminate multiple harmonics due to symmetry caused by the plane reference wave and the quantization of phase at the apertures and was confirmed with experimental results [6]. However, in the experiments the focuses were formed 10cm away from the hologram. In AWG design, the focuses are to be formed in the nearer field. So a set of simulations is performed to test if the image points can be generated in the nearer field region and the deviation of the placement of these image points compared to designed location. The simulations below show good agreement with the theory. The images are able to form as shown in Figures 3.6 and 3.7, and the deviations are indeed negligible as shown in Figures 3.8, 3.9.a, 3.9.b, Tables 3.1 and 3.2. The source of these errors is the spatial quantization used in

simulation. The spatial resolution is chosen to be 0.2_μm, which is comparable to current fabrication technology. Figures 3.8, 3.9.a, 3.9.b, and 3.9.c show the formation of the focuses with changing displacement from the input. Figure 3.8 shows a very near field image formation at 1mm away from the input. Note a dark red dot very close to the left hand side of the Figure. In medium to far field conditions of 5mm and 20mm, the images are brighter and begin to be stretched out. This is largely due to phase variation in the field in the longitudinal direction. In the near field the phase varies much faster than far field, so the focuses are more stable and tends to stretch out in longitudinal direction. The x-axis is in vertical direction, which is the transverse direction, and the z-axis is in horizontal direction, which is the longitudinal direction (as shown in demultiplexing output in Figures 3.8, 3.9.a and 3.9.b). So the x-axis deviation is compared to the dispersion of wavelength spacing used for regular demultiplexing (the dispersion relationship is shown in the following), which is indeed negligible. Precise placement of image points allows the demultiplexing operation to be performed. The field intensity at the designed location is compared to the field intensity measured at the actual image point. The change in intensity due to shift of image point is also very small. This simulation validates that the method of One-Image-Only hologram can be adapted to AWG design.

3.6.2 Zero crossing dispersion relation

The dispersion relation is derived in Equation (3.25); it is repeated below for convenience.

$$\Delta x = x'_0 - x_0 \approx -z_o \frac{\Delta \lambda}{\lambda'} \left(\delta - \frac{n_c x_c}{z_c} \right) \quad (3.25)$$

Throughout this simulation, δ , x_c , and z_c are fixed ($x_c = z_c = 3.5\text{mm}$, $\delta = 1550\text{nm}$). In Figure 3.10, the line shows the spatial dispersion of two images formed due two input waves of varying wavelength separation. The linear factor δ is fixed ($\delta = 30$) while each line represents a different z_o . The measured dispersion factor is compared to the theoretical values in Table 3.3. Similarly in the Figure 3.11, dispersion relationship is shown over the selected δ values, while z_o is fixed at 45mm. A comparison with the

theoretical dispersion factor is also made in Table 3.3. The simulation shows excellent agreement between theoretical and simulation dispersion factors.

3.6.3 Output intensity in harmonics for irregularly spaced phased array

As shown in Equation (3.56), the intensity of higher harmonics decreases as the randomness of the phased array increases. The intensity at the peak of a harmonic is given as

$$E\left[|P(Y_m)|^2\right] = N + (N^2 - N) \sin^2(m\eta) \quad (3.56)$$

Figure 3.12 shows the intensity of 1st and 2nd harmonics vs. the change of randomness measure η . $\eta=1$ indicates maximum degree of randomness defined in section 2.5.2, $\eta=0$ indicates minimum randomness i.e. uniformity in phase element spacing.

3.6.4 Discussion

The simulations shown in this section validate the theoretical results obtained from derivation, the forming focuses by zero cross sampling of spherical reference wave, demultiplexing of multi-wavelength inputs, and elimination of harmonics using irregularly sampled phased arrays. The tiny errors are caused by spatial quantizations in the simulations. This quantization error would also be present in actual fabrication process. The spatial resolution is chosen at 100nm. As for the ISZC AWG, electromagnetic field propagation is in different semiconductor media and propagation distances are shorter. Propagation in single mode waveguides can be better approximated by Gaussian beams. In the following chapter, a Gaussian beam based model for ISZC AWG simulation is discussed.

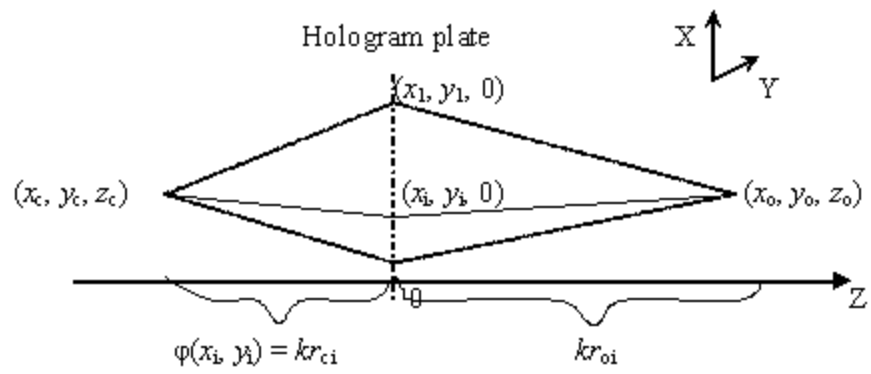


Figure 3.1. Geometry of one-image-only digital holography with spherical reference wave.

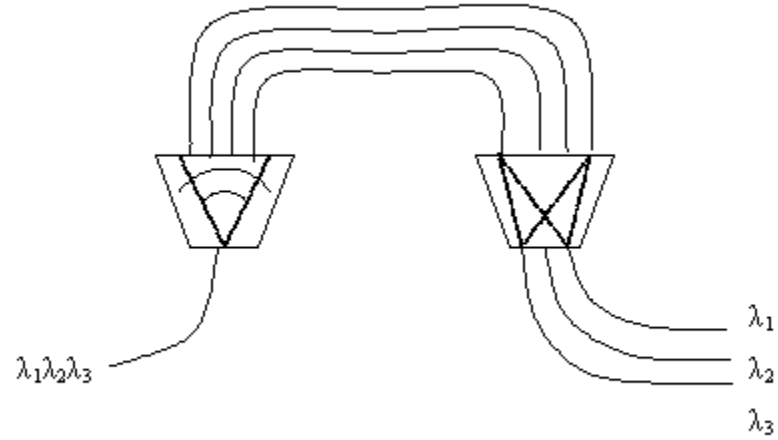


Figure 3.2.a. Zero crossing phased array wavelength demultiplexing.

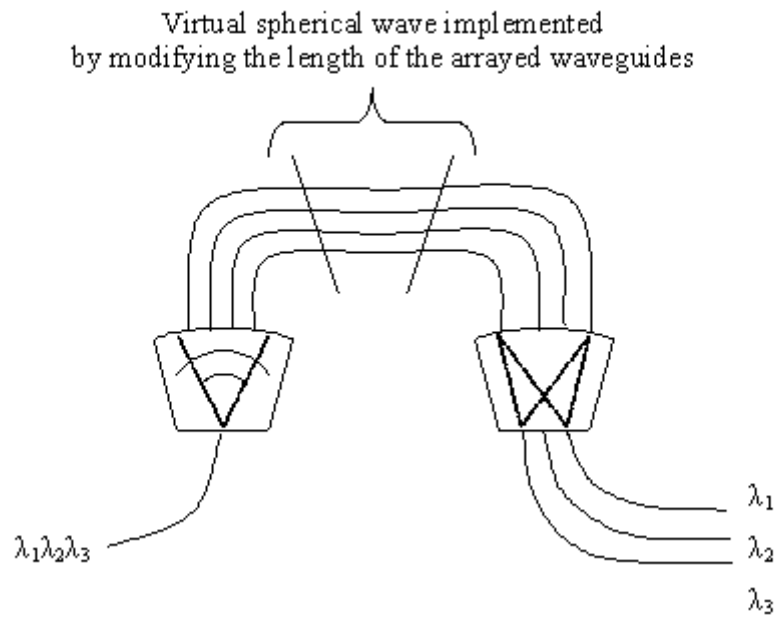


Figure 3.2.b. Zero crossing phased array wavelength demultiplexing with virtual spherical reference wave implemented in waveguides.

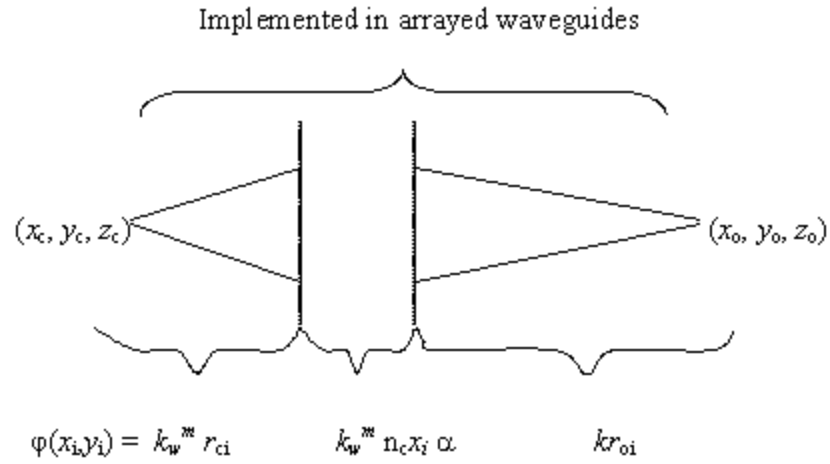


Figure 3.2.c. Corresponding phase terms implemented in the i^{th} arrayed waveguide.

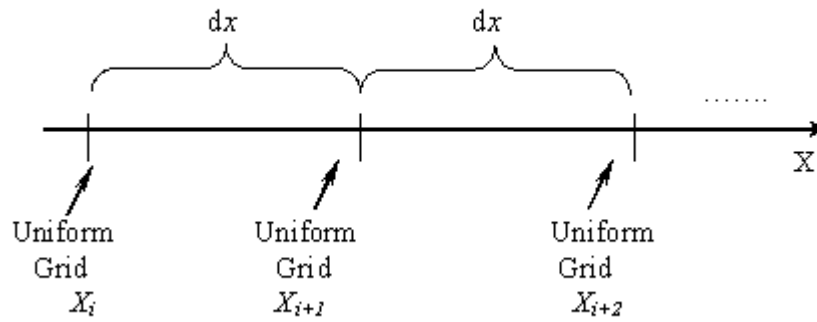


Figure 3.3.a. The uniform grid.

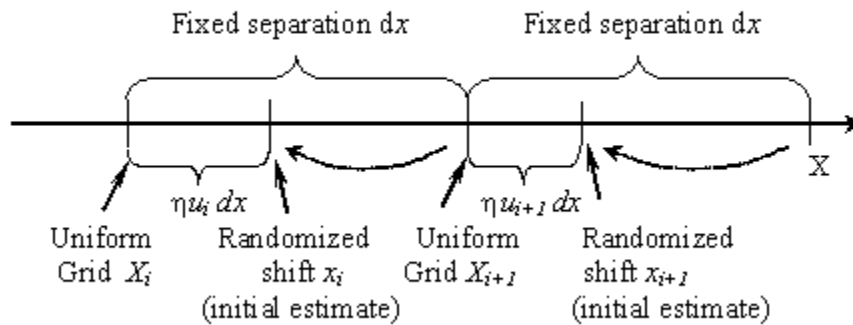


Figure 3.3.b. Initial estimate for zero crossings.

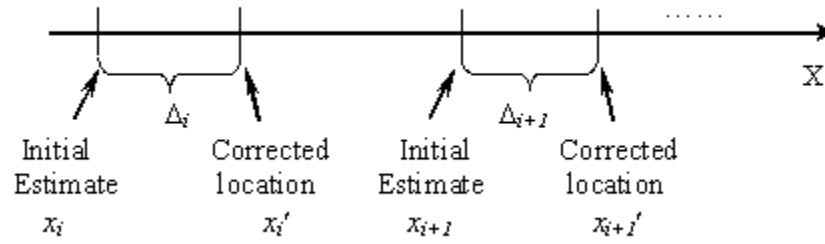


Figure 3.3.c. Zero crossings determined.

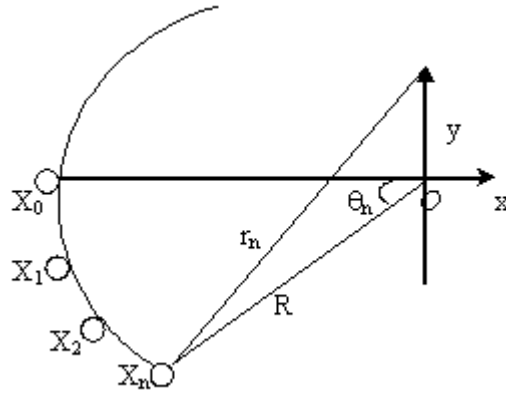


Figure 3.4. Illustration of irregular phased array on a circular arc.

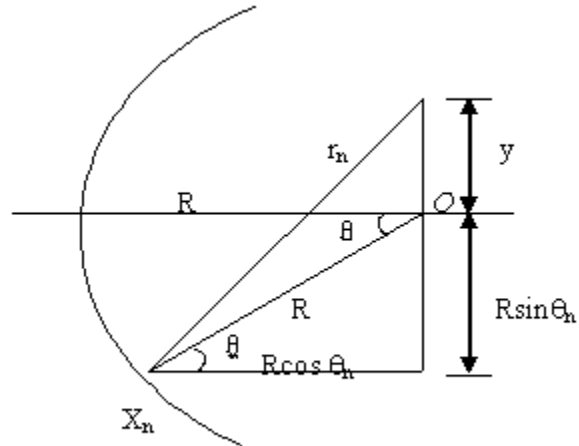
Figure 3.5. Geometry of $r_n(y)$

Table 3.1 Percentage difference of x-axis deviation to dispersion at selected wavelengths.

Z_0	0.4nm	0.8nm	1.2nm	1.6nm
20mm	2.4%	1.2%	0.8%	0.4%
40mm	1.8%	0.9%	0.5%	0.3%
80mm	0.8%	0.4%	0.2%	0.1%

Table 3.2 Intensity variation of designed image points and simulation results.

Z_0 (mm)	5	10	20	30
Intensity variation %	4.3%	1.2%	1.1%	1.1%

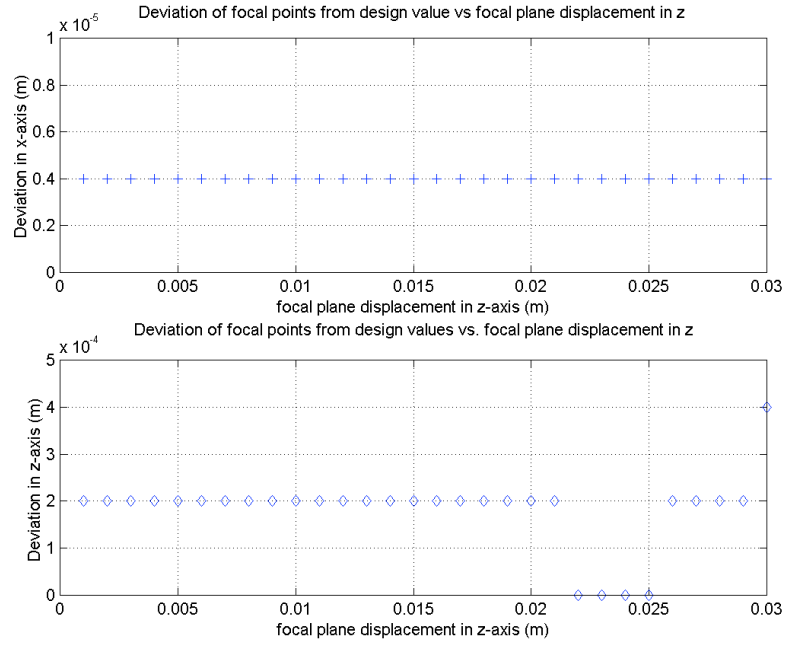


Figure 3.6. Focal point deviation in the near field.

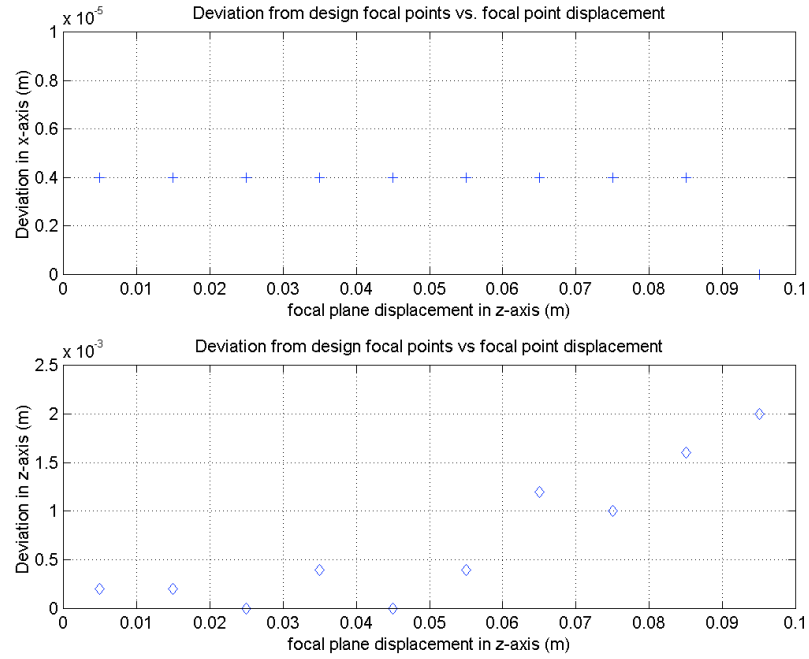


Figure 3.7. Focal point deviation in the far field.

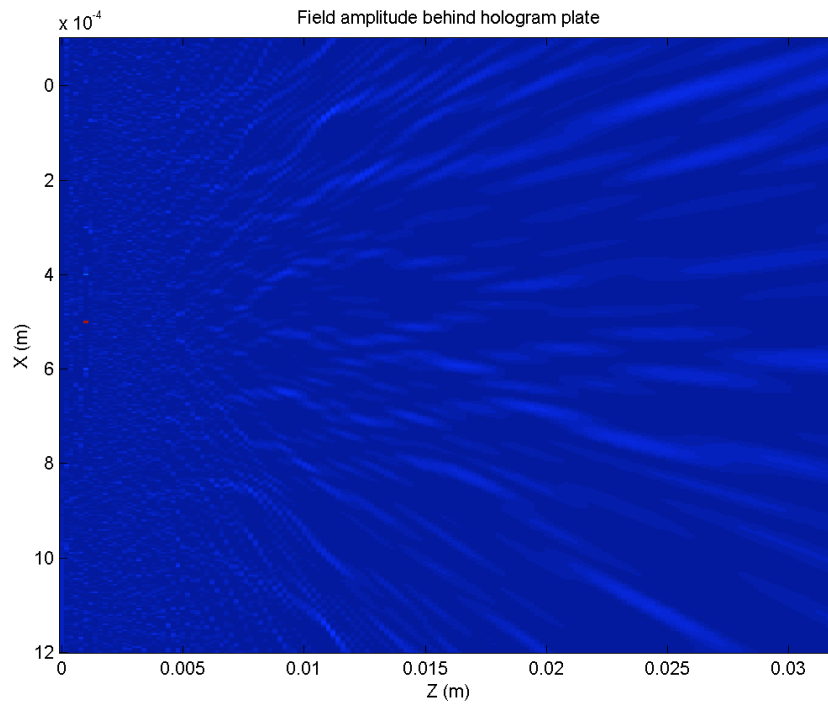


Figure 3.8. Near field focal point (1mm).

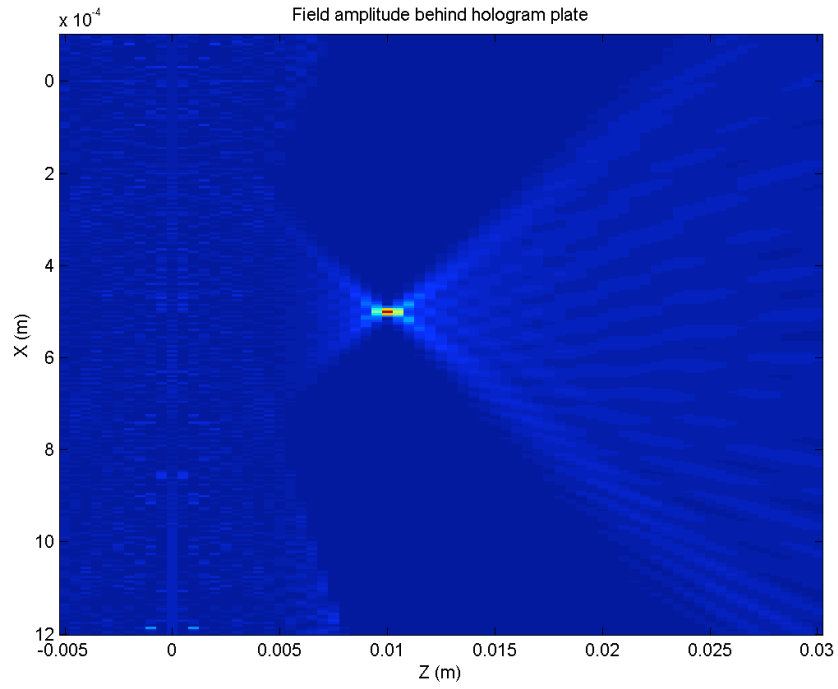


Figure 3.9.b. Near field focal point (10mm).

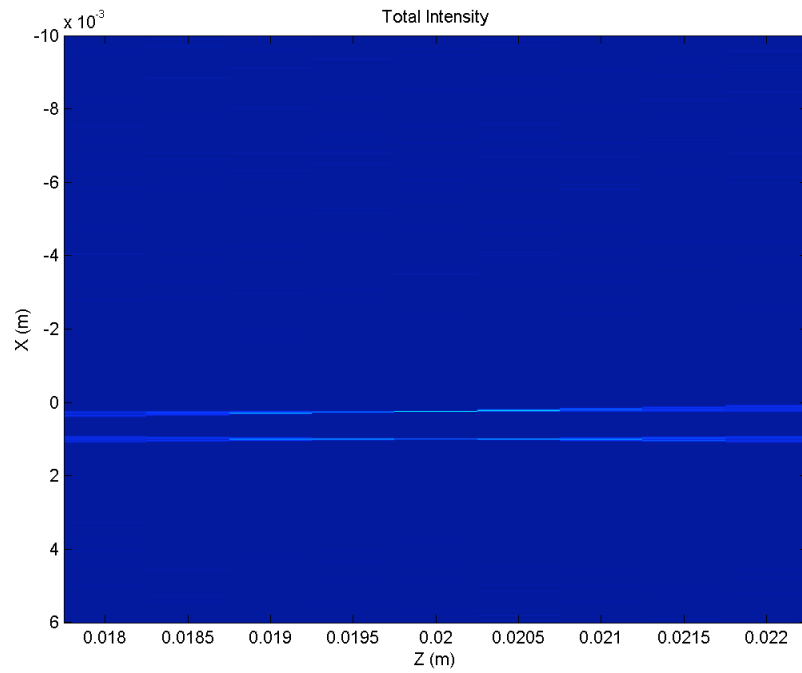


Figure 3.9.c. Mid-field focal point (20mm)

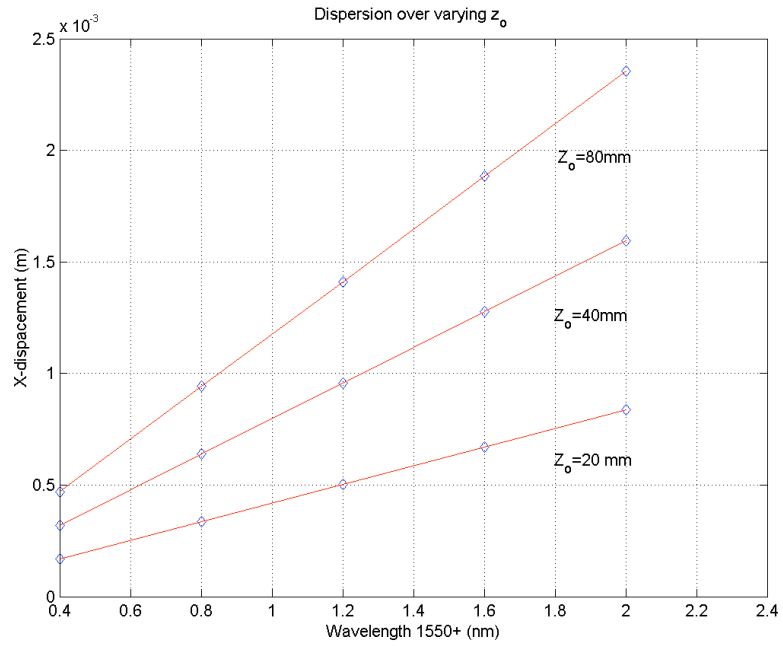


Figure 3.10. Dispersion relation for selected image planes.

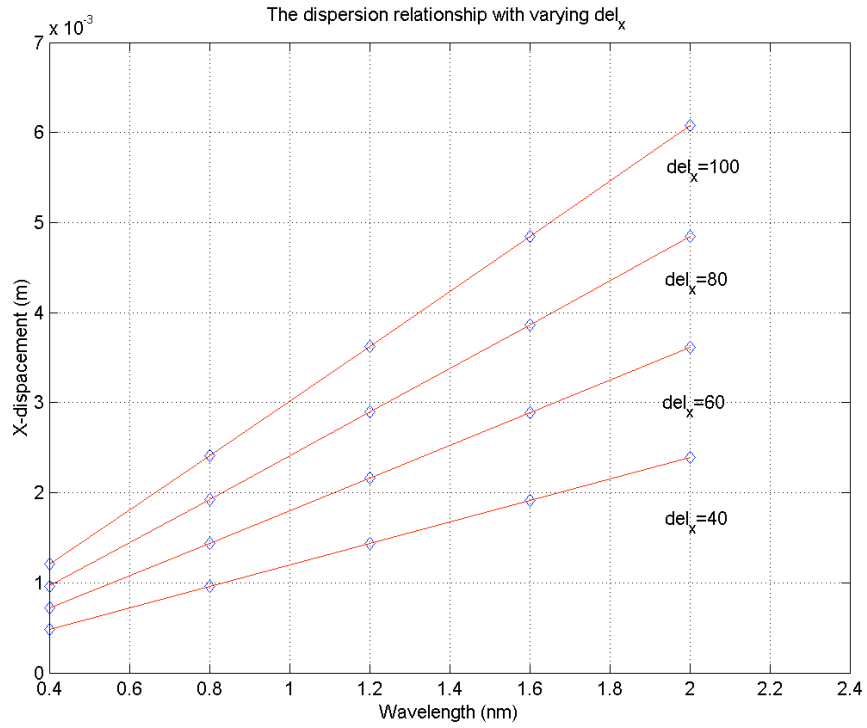


Figure 3.11. Dispersion relation for selected $_$ values.

Table 3.3 Dispersion factor with fixed $_$ and fixed z_0

$_$	Dispersion slope			Z_0	Dispersion slope		
	Simu.	Theo.	% diff.		Simu.	Theo.	% diff.
40	0.958E6	1.13E6	15.4%	20mm	0.238E6	0.274E6	13.1%
60	1.447E6	1.71E6	15.5%	40mm	0.638E6	0.548E6	28.3%
80	1.939E6	2.29E6	15.3%	80mm	0.983E6	1.096E6	10.3%
100	2.437E6	2.87E6	15.2%				

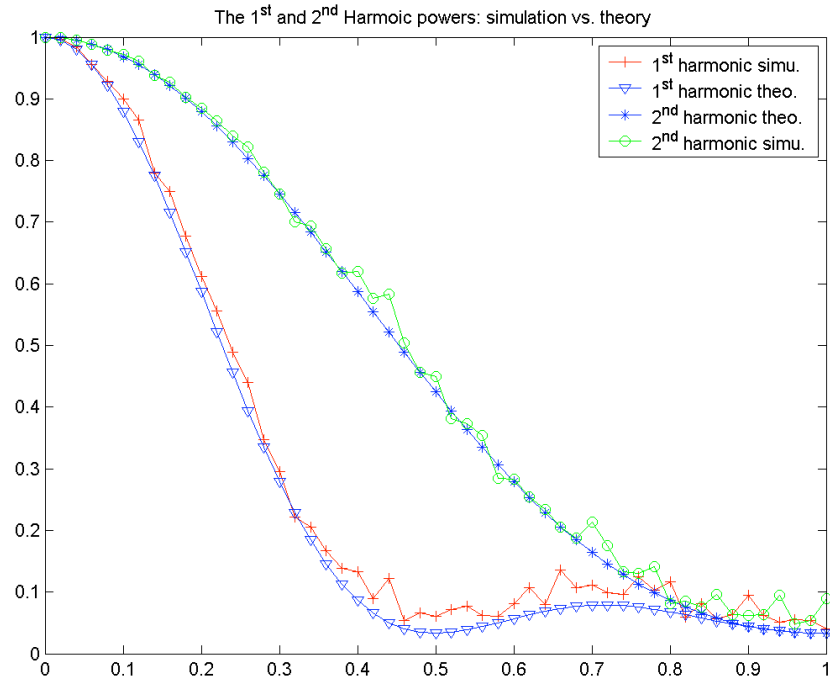


Figure 3.12. Monte Carlo simulation of 1st and 2nd Harmonic peak intensity vs. random measure.

4. IMPLEMENTATION OF ISZC PHASED ARRAY USING BEAMPROP AWG UTILITY BY RSOF

The ISZC phased array demultiplexing design is implemented using the AWG utility included in the *BeamPROP*TM professional simulation package. In this chapter, we

first discuss the implementation of a spherical wavefront modulation related to zero-crossing sampling, wavelength dependent linear phase change as well as irregular sampling by adjusting lengths and placement of arrayed waveguides. Then the layout of ISZC phased array using *BeamPROP*TM AWG utility, and transfer of ISZC design in *BeamPROP*TM simulation are presented. An explanation of the Beam Propagation Method (BPM), which *BeamPROP*TM is based on, is given. Finally we show the simulation results of ISZC modified AWG in comparison with the original AWG.

4.1 Waveguide Implementation of ISZC Phased Array Wavelength Demultiplexing

4.1.1 Overview and motivation for waveguide implementation

First we look closely at the phase evolution of the input wavefront in a regular AWG. Observing the input coupler in a regular AWG, we see the input field is coupled to the input coupler via a waveguide; the field then propagates and expands in the coupler until the wavefront reaches the output coupling apertures ready to be coupled to the arrayed waveguides at the end of the input coupler. Assuming all waveguides are single mode, the field emerging from the input waveguide is approximately TEM₀₀ Gaussian mode [44]; in most cases the coupler is sufficiently large compared to wavelength of the input field [33, 15]. Then as the field reaches the end of the coupler, its wavefront can be considered a spherical wave. The end of the input coupler is shaped to be circular (in 2D) to match the expanded spherical wavefront. The input field is then coupled to the arrayed waveguide by apertures placed uniformly at the end of the input coupler. So the initial phases of the wavefronts inside each arrayed waveguides are almost identical. As these wavefronts propagate through the arrayed waveguides, each alters its phase depending on the length of the waveguide it travels in. Since the lengths of the arrayed waveguides increase in a linear fashion, a linear phase change proportional to spatial displacement is added to these wavefronts at the output of the arrayed waveguides. All the wavefronts are then coupled to the output coupler. As each wavefront emanates from the coupling aperture placed on the interface between the arrayed waveguides and the output coupler, each of them goes through a diffraction process in the output coupler. The resulting interference pattern accomplishes the focusing and demultiplexing functions.

Following the above discussion, we observe the initial phases are the same in all arrayed waveguides, and then a linear phase shift is accumulated as the waves travel through the entire lengths of the arrayed waveguides. The key in implementing the ISZC method on AWG is to introduce a spherical wave modulation to the input wavefront in the arrayed waveguide section, which is done by properly adding a stretch of waveguide for each individual AW. There are two justifications for this modulation. Firstly, as we have seen in the previous chapter, the spherical reference wave can remove high order diffractions due to discretization of phases in zero crossing sampling. Secondly, the additional spherical wave makes random placement of AW's on the AW/OC interface possible. To modify the regular AWG with ISZC method, three constraints are needed. The first two are zero crossing phase condition and irregular sampling for the placement of the phase elements, i.e., coupling apertures, on the AW/OC interface. The third constraint is the linear phase change from waveguide to waveguide, which induces wavelength related phase dispersion. The regular AWG already satisfies the zero crossing condition and the linear phase dispersion requirement. If randomness of the placement for the phase elements is introduced, the zero crossing phase matching and the linear phase dispersion cannot be satisfied simultaneously. The parts of the total phase shift are shown in Figure 4.1. In Figure 4.2, the phase elements are placed on circular arcs at the IC/AW and AW/OC interfaces, and all phase elements are the same distance away from the symmetric focal points for the two circular arcs. To illustrate this point, from the phase relation given in Equation (3.29), we have

$$r_{ci} + x_i \delta + r_{oi} = n\lambda + \text{constant} \quad (4.1)$$

In this case, without the spherical wave, we have a plane wave input as argued previously: $r_{ci} = \text{constant}$; constant distance to focal points: $r_{oi} = R$, α is the center wavelength, eliminating the constants the equation becomes

$$x_i \delta + R = n\lambda \quad (4.2)$$

$n = 1, 2, 3, \dots$; $i = 1, 2, 3, \dots, N$; α, R are constants, therefore the location of phase elements (end of arrayed waveguides) x_i 's cannot be random.

Introduction of spherical wave modulation generates additional phase fluctuation across the arrayed waveguides. This enables us to find zero crossing points while still including the spatial linear phase modulation. So the equation becomes

$$r_{ci} + x_i \delta + r_{oi} + R = n\lambda_0 + \text{constant} \quad (4.3)$$

Additional lengths of r_{ci} and r_{oi} can be stretches of waveguides added to each arrayed waveguide, so that x_i can assume random positions.

4.1.2 The modification of regular AWG

In order to modify a regular AWG with ISZC method, the placement and length of the regular AWG arrayed waveguide should be altered. The placement of the phase elements follows the ISZC design algorithm described in detail in Chapter 3. The algorithm involves two steps: laying out a uniformly spaced angular grid and then introducing a random shift on each grid point within the range of a unit step length. The length of individual arrayed waveguide is controlled by three factors: 1) spherical modulation, 2) linear phase modulation, and 3) zero crossing phase matching. Note the arrayed waveguide length calculation and phase element placement are satisfied simultaneously. When the spherical modulation is properly chosen (the radius of the sphere is not too large), the zero-crossing phase matching and irregular sampling are decoupled, due to the fact all phase elements have the same distance to the focal point, and ZC phase correction is done by adjusting the length of the individual waveguide. Therefore the calculated location is both a random point and it also satisfies zero-crossing phase match condition. We note that the zero-crossing points can also be generated by the shifting of position of the aperture as discussed in Chapter 3.

The overall design procedure to implement ISZC technique on regular AWG requires two major steps: 1) setting up the random points, and 2) calculating the compensation to the random points for zero crossing phase condition. Since Step 1 has been illustrated previously, this discussion is centered more on Step 2.

Step 1) Setting up the random points. The geometry is shown in Figure 4.2 above. The random points are on a circular curvature, and their coordinates θ_n 's are given as:

$$\theta_n = n\theta + \eta \cdot u(0, \theta) \quad (4.4)$$

θ : a constant;

n : 0, 1, 2, ..., N;

η : randomness measure, $0 \leq \eta \leq 1$;

u : a uniformly distributed random number, $0 \leq u \leq \theta$;

R : radius of the circular curvature.

Therefore, as $\eta \rightarrow 0$, θ_n is uniformly spaced on the curvature; as $\eta \rightarrow 1$, θ_n has the largest degree of randomness. The coordinates of the random points are then transferred from polar coordinates to Cartesian coordinates.

Step 2) Calculating the individual waveguide length. The length of each arrayed waveguide is made up of three sections as shown in Figure 4.3, spherical wave modulation L_s , linear phase dispersion L_p , and zero crossing phase matching L_z . They are given in the following:

$$L_s = R' \cos \theta_n - r \quad (4.5)$$

$$L_s = R' - R' \cos \theta_n \quad (4.6)$$

$$R'^2 = r^2 + \left(\frac{X_{\max}}{2} \right)^2 \quad (4.7)$$

$$L_p = x_i \alpha \quad (4.8)$$

$$L_z = \lambda - [(L_s + L_p) \pmod{\lambda}] \quad (4.9)$$

Equation (4.5) and (4.6) are for divergent and convergent spherical wave respectively; r is the distance from the center of the virtual spherical wave away to the virtual phase plane; X_{\max} is maximum width of the coupler; x_i is x-axis coordinates for random points; L_z is the length that makes total waveguide length ($L_s + L_p + L_z$) multiples of wavelength λ , so the zero crossing phase matching is satisfied.

4.2 ISZC Modified AWG Layout and Simulation Using *BeamPROP*TM

*BeamPROP*TM is a Beam Propagation Method (BPM) based waveguide simulation package. BPM is the most widely used numerical method for integrated optical devices simulation and is the method of choice for most commercial software. There are many benefits of the BPM. One is its simplicity in concept and implementation. It has good

efficiency. The computation complexity is linearly proportional to the number of grids in the computation domain. It is also easily adapted into complex geometries for different devices. The BPM also readily includes the guided and scattering fields, as well as mode coupling and conversion. Finally, the BPM is also a very flexible method. On the other hand, the basic BPM assumes scalar and paraxial field conditions as well as lacking capacity to account for backward reflection. In *BeamPROP*[™] Version 4.0, with some extension of the basic BPM, the vector field and nonlinearity effects can be included. The paraxial field condition can also be relaxed to a more general wide-angle implementation. The bidirectional algorithm can be implemented to account for back reflection waves. The **AWG Utility** is part of the *BeamPROP*[™] package. It has a CAD layout program, which generates waveguide layout for the standard AWG's. There is also a script program that generates script files to simulate the AWG structure using the core BPM program.

4.2.1 Overview of regular and ISZC modified AWG layout and simulation

The procedures for regular AWG layout and simulation are illustrated in the *BeamPROP*[™] **AWG Utility Version 2.1** [45]. A brief description of both procedures is presented here for later discussion to extend the design to generate the ISZC modified AWG layout and simulation. *BeamPROP*[™] simulation package uses the **WDM Router Layout File** option under the **Utility** pull down menu in the main *BeamPROP*[™] window to generate related layout files. The parameters of the number of Wavelength Channels, number of input/output ports, and number of Arrayed Waveguides, Center Wavelength, and Channel Spacing should be provided in the dialog box. (A step-by-step procedure can be found in detail in the *BeamPROP*[™] **AWG Utility**, Chapter 4). The layout files for a desired regular AWG design can also be generated by using command line to run the executable of the *stargen.c* CAD layout program. The modified AWG layout design is accomplished by modifying the CAD program. The generated layout files are

<meta-prefix>in.ind	input start coupler
<meta-prefix>out.ind	output star coupler

<meta-prefix>full.ind	full layout with “round” array turn
<meta-prefix>flat.ind	full layout with “flat” array turn

The star coupler files are used for simulation; the full layout files are used for mask generation. Based on the completed AWG layout design, a script file is generated using the **WDM Router Simulation** option under the **Utility** pull down menu. The script file calls the various executables and handles data movement among these programs. Then by selecting the **Run Script** option under the **Run** pull down menu in the main *BeamPROP*TM window; simulation of the designed AWG can be processed. When the simulation is complete, a plot showing the results in wavelength axis is displayed.

The ISZC enhanced AWG design layout is carried out by a modified CAD program, which is run from a DOS command window in Windows PC environment. Using the ISZC modified layout files; the script for processing the simulation is generated in the same way as regular AWG simulations. The execution and result of simulation also follow the same procedure as regular AWG simulations. The key to successfully implement the ISZC in AWG design is to modify the layout design equations provided in the **AWG Utility Version 2.1**, and incorporate them into the CAD layout program. In the following, the regular AWG layout is discussed, and then, it is followed by an extension to incorporate the ISZC features.

4.2.2 Layout design for regular AWG

Given all the required parameters of a regular AWG design, two types of layout geometries “flat” and “round” can be generated by the *stargen.c* layout program. Since the **AWG Utility Version 2.1** manual only provides the “round” layout design, this discussion is limited to the “round” layout. Both layouts are shown schematically in Figure 4.4. The following variables are important with respect to the full router layout:

A central angle of star couplers with respect to z axis

Rin/Rout	radius of input/output waveguide bends
Rz	minimum radius of arrayed waveguide bends
Lg	length along z of arrayed waveguide structure
Lextra	additional length added to Lg
Lin/Lout	straight length of input/output waveguides
Sin/Sout	lateral separation if input/output waveguides

The constraint equations for the option 1 are given as follows

$$zL_i + (zA_{ai} * zR_i) - (A_0 * R_z) = (i-1) * dL/2 \quad (4.10)$$

$$zR_i * \sin(zA_{ai}) + (R_{end} + zL_i) * \cos(zA_{ai}) = R_z * \sin(A_0) + R_{end} * \cos(A_0) \quad (4.11)$$

The definitions of the variables are illustrated in Figures 4.5 and 4.6. Both figures show half of the Full Layout configuration shown in Figure 4.4; the other half is symmetrical as shown in Figure 4.4. Two constraints are needed to generate the Full Layout. One is the progressive path length differences between successive waveguides. The other one is the alignment of waveguides along the z-axis, so that when flipped along the plane of symmetry (shown in Figure 4.4), the waveguides can connect smoothly. Corresponding to Figure 4.5, Equation (4.10) describes the path length difference between the first waveguide, which is located at $A_0 (=zA_{a1})$, and the i^{th} waveguide placed at zA_{ai} . The radius of the first waveguide is $R_z (=zR_1)$. As shown in Figure 4.6, Equation (4.11) describes the alignment of all waveguides along the z-axis; they are equal to the dimension of the first waveguide in z-axis. Solving Equations (4.10) and (4.11), given zA_{ai} as constant, zR_i and zL_i can be found, which determines the layout of the i^{th} waveguide. Equations (4.10) and (4.11) are coded in the layout program `stargen.c` along with other auxiliary equations to calculate the entire Full Layout design. In the following section, this design method is extended to incorporate ISZC techniques.

4.2.3 Adopting regular AWG layout design to ISZC based AWG

Since only Full Layout constraint equations are provided, the ISZC method is implemented for the Full Layout. Once the design equations of the Flat Layout are available, the same principle used for Full Layout also applies. The essential difference between regular AWG design and ISZC enhanced design is the irregular spacing of waveguides on the input and output couplers. There are three major issues needed to be addressed. Two of them involve the modification of the layout program STRAEGEN.C. The third uses a feature in the **WDM Router Simulation** option under the **Utility** pull down menu in the main *BeamPROP*TM window to compensate for phase calculation (phasecore.exe) based on uniform path length increment in regular AWG device.

The first modification is the placement of waveguides on the input/output couplers. For the i^{th} waveguide the waveguide is placed at an angle zA_{ai} away from reference as shown in Figure 4.5. In regular AWG implementation, zA_{ai} is calculated uniformly ($zA_{ai}=(i-A_{so})\cdot A_o$) in stargen.c. Before design layout for ISZC modified AWG, the arrayed waveguide path lengths and location of waveguide placement at input/output coupler are calculated in a MatlabTM program. The second modification is to Equation (4.10); the RHS of the equation is the path difference between the first waveguide and the i^{th} waveguide, which is calculated uniformly in regular AWG case. In implementing ISZC, this path difference should be random, which can also be calculated in the MatlabTM program. Equation (4.11) stays the same. The system of Equation (4.10) and Equation (4.11) is again solved in the Matlab program for zR_i and zL_i . When carrying out ISZC modified AWG layout, zA_{ai} , zR_i , and zL_i are required parameters for defining the layout using stargen.c. In the original STARGEN.C zA_{ai} , zR_i , and zL_i are calculated within the program. In the modified layout program, these three sets of data are imported to STARGEN.C using results from MatlabTM program calculation.

4.2.4 A Note on PHASCORE.EXE

During the *BeamPROP*TM simulation of the AWG layout, both input and output couplers are simulated using the main BPM program. The phase retardation in the array waveguide is simulated by adding phase induced by the path length of waveguide to the field profile entering the arrayed waveguides from the input coupler. This simplification

is justified since the traveling wavefront inside single mode waveguides is a plane wave only accumulating phase in longitudinal direction. This phase calculation is accomplished in an executable program called PHASECOR.EXE. However, this executable code is designed for regular AWG devices, and it assumes uniform length increments in the arrayed waveguides. Some modification is in order to incorporate the ISZC method.

The initial phase at the starting of each arrayed waveguide involves the coupling due to the interface between the coupler and the starting of every waveguide section. This coupling effect is simulated by the main *BeamPROP*[™] BPM simulator. As illustrated below, the BPM simulator propagates the input field in a series of xy planes (n=1,2,3...,N) throughout the input coupler along the z-axis. The Nth xy plane stops just crossing the tangential (indicated by the X' axis in Figure 4.7) of the circular arc at the end of the IC. So, on the xy plane of the last BPM step, the fields are coupled into all arrayed waveguides. The fields in some AW's have traveled further than that in the middle. The phases at the starting of each waveguide can be calculated by retracing back the distance traveled in each of the waveguides, since all AW's are straight and in radial direction from the center of the arc.

So let φ_{i0} be the phase in the *i*th waveguide at the end of BPM calculation, and θ_{i0} be the initial phase at the interface of the coupler slab region and *i*th arrayed waveguide. Then, φ_i , the overall phase for the *i*th waveguide is given as

$$\begin{aligned}\varphi_{i0} &= \theta_{i0} - R \left(\frac{1}{\cos \theta_i} - 1 \right) k \\ \varphi_i &= \varphi_{i0} + k [(i-1)\Delta L + L_0]\end{aligned}\tag{4.14}$$

The executable PHASCORE.EXE takes the initial phase calculated in the above fashion, and adds the phase accumulated by field in each AW according to individual AW length. Therefore, in simulating ISZC based AWG structures, the nonlinear increment of waveguide-stretch for each arrayed waveguides can not be provided in PHASCORE.EXE. This can be remedied by using a phase correction feature provided by *BeamPROP*[™]. Under the **WDM Router Simulation** option in the **Utility** menu, the **WDM Router Description File Generator** dialog box offers the **Design Info File** option as shown in Figure 4.9. Design Info Files can include phase, transmission, and

length corrections to the arrayed waveguides information. In this case, only length correction information is needed. This length correction is given by first finding out the path lengths of the arrayed waveguide of the regular AWG to be modified, then subtracting it from the results of ISZC enhanced version of the arrayed waveguide. The format of the Design Info File is specified in *BeamPROP™ AWG Utility Version 2.1, Appendix C*. An example is given below to correct an ISZC AWG router with 3 arms for the arrayed waveguide:

PhaseCorDataFormal	<fixed title>
3 1	<number of arms><number of data field columns>
dL	<data-name 1><data-name 2> ...
11.3	<data-name 1><data-name 2> ... (for arm 1)
-5.4	<data-name 1><data-name 2> ... (for arm 2)
7.8	<data-name 1><data-name 2> ... (for arm 3)

Table 4.1 Example of Design Info File used to correct PHASCORE.EXE.

<data-name> could be taken from “Transmission”, “Phi”, or “dL” to adjust power, phase, and length of every arrayed waveguide. The file is saved as a text file, and its name is used in the **Design Info File** option under the **WDM Router Description File Generator** dialog box. Thus the PHASCORE.EXE can be used in ISZC AWG simulation successfully.

4.3 Discussion of BPM Methods

To better comprehend the simulation results obtained from the BeamPROP, it is critical to understand the strengths and limits of the simulation method employed. Like most simulation tools in optical component design, BeamPROP is based on the Beam Propagation Method (BPM), which is the most widely applied technique in optical component design. This section discusses the underlying approach used for BeamPROP implementation of BPM, and its advantages and some inherent weakness as well as remedies to the limitations in the basic BPM formulation. It starts with the development

of a basic FD-BPM [5, 6], which is different from conventional Fourier based approach [7, 8]. Then it goes on to cover the extension to Wide-angle BPM and vectorial BPM, which relaxes the assumption of scalar field and paraxial propagation in the basic FD-BPM formulation. Both extensions are available options in the BeamPROP software package.

4.3.1 General BPM

The BPM/scalar paraxial approximation is actually a way of solving the Helmholtz equation. The scalar time independent Helmholtz equation is given as

$$\frac{\partial^2 \phi}{\partial x^2} + \frac{\partial^2 \phi}{\partial y^2} + \frac{\partial^2 \phi}{\partial z^2} + k(x, y, z)^2 \phi = 0 \quad (4.15)$$

where the scalar electric field is written as $E(x, y, z, t) = \phi(x, y, z)e^{-i\omega t}$; and the notation $k(x, y, z) = k_0 n(x, y, z)$ is the spatially dependent wavenumber with $k_0 = 2\pi/\lambda$ being the wavenumber in free space. The refractive index of the region of interest is given as $n(x, y, z)$. The paraxial approximation is that the wave propagation in the waveguide is primarily along the longitudinal direction, the z -axis. The phase variation of the wavefront due to propagation in z -axis is the most rapid component. The scalar Helmholtz equation can be simplified by factoring out the phase variation in z -axis. Let

$$\phi(x, y, z) = u(x, y, z)e^{i\beta z} \quad (4.16)$$

Here β is a constant number representing the average phase variation of the field ϕ , and is referred to as the reference wave number. The reference wave number can also be expressed as $\beta = k_0 n_0$; n_0 is the reference refractive index. Using the above relationship, the Helmholtz equation can be simplified as

$$\frac{\partial^2 u}{\partial z^2} + 2i\beta \frac{\partial u}{\partial z} + \frac{\partial^2 u}{\partial x^2} + \frac{\partial^2 u}{\partial y^2} + (k^2 - \beta^2)u = 0 \quad (4.17)$$

This equation describes the slowly varying field u . Assume the variation of u with z is sufficiently slow so that the first term above can be neglected with respect to the second. The result is the familiar slowly varying envelope approximation, and in this context, it is

referred to as the paraxial or parabolic approximation. Using this approximation and rearranging the equation, we get

$$\frac{\partial u}{\partial z} = \frac{i}{2\beta} \left(\frac{\partial^2 u}{\partial x^2} + \frac{\partial^2 u}{\partial y^2} + (k^2 - \beta^2)u \right) \quad (4.18)$$

This is the basic BPM equation in three dimensions; the two-dimensional BPM equation is obtained by omitting the dependency on y . Once the input field $u(x, y, z = 0)$ is given, the above equation determines the evolution of the field in the space $z > 0$.

There are two major benefits in this approach. First, once the rapid phase variation is factored out, the slowly varying field can be represented numerically along the longitudinal grid, which can be many orders of magnitude larger than that of the wavelength. This effect makes the BPM much more efficient than purely finite difference based techniques, which requires grid spacing of one tenth of the wavelength. Secondly, eliminating the second order derivative term in z enables the problem to be treated as a first order initial value problem instead of a second order boundary value problem. A second order boundary value problem usually requires iteration or eigenvalue analysis, yet a first order initial value problem can be solved by simple integration of the equation in the z -direction. This effect similarly decreases the computational complexity greatly compared to full numerical solution of the Helmholtz equation. There are also prices paid for the reduction of computational complexity by the BPM formulation. The slow envelope approximation assumes the field propagation primarily along the z -axis (i.e. the paraxial direction), and it also limits the index contrast of the waveguide. Removing the second derivative in the approximation also eliminates the backward traveling wave solutions. So reflection based devices are not suited for using this approach. However, these issues can be resolved by recasting the approximations, so the assumptions can be relaxed. Extensions such as wide-angle BPM and bi-directional BPM have been formulated, and they will be discussed later. BeamPROP uses a finite difference based numerical method to implement the basic BPM formulation, which is reviewed in the following section.

4.3.2 Finite difference based BPM

Most early BPM techniques use the well-known split-step Fourier method proposed by Feit and Fleck [48]. Later a finite difference method based on equation (4.18) was developed [46]. It can be shown that the finite difference based method is more accurate in dealing with waveguides with larger index contrast [47, 49]. It can also use larger longitudinal step size to ease the computation complexity without compromising accuracy [51]. It has consequently become the standard approach, and is reviewed below.

Using the finite-difference approach, the field is represented by discrete points on a grid in transverse planes, which is located along the longitudinal or propagation direction (z). Once the input field is known (at $z=0$), the field on the next transverse plane in the propagation direction can be calculated. Repeating this procedure, the field of propagation waves can be calculated one step a time along the propagation direction through the domain of interest. This approach is illustrated for a scalar field in 2D (xz); extension to 3D is easily obtained.

Let u_i^n denote the field at transverse grid point i and longitudinal plane n , and assume the grid points and planes are equally spaced by Δx and Δz apart, respectively. In the Crank-Nicholson method, Equation (4.18) is represented at the midplane between the known plane n and the unknown plane $n+1$ as follows:

$$\frac{u_i^{n+1} - u_i^n}{\Delta z} = \frac{i}{2\beta} \left(\frac{\delta^2}{\Delta x^2} + (k(x_i, z_{n+1/2}) - \beta^2) \right) \frac{u_i^{n+1} + u_i^n}{2} \quad (4.19)$$

The Crank-Nicholson method is illustrated above in Figure 4.10. Here δ^2 represents the standard second order difference operator, $\delta^2 u_i = (u_{i+1} + u_{i-1} - 2u_i)$, and $z_{n+1/2} \equiv z_n + \Delta z / 2$. The above equation can be rearranged into the form of a standard tridigonal matrix equation for the unknown field u_i^{n+1} in terms of known quantities, resulting in:

$$a_i u_{i-1}^{n+1} + b_i u_i^{n+1} + c_i u_{i+1}^{n+1} = d_i \quad (4.20)$$

Given $h=\Delta z$ and $\rho=\Delta z/\Delta x^2$, the variables a_i , b_i , c_i , and d_i are given as follows:

$$\begin{aligned}
A_i^{n+1/2} &= \frac{i}{2\beta_i^{n+1/2}} \\
B &= i \frac{k^2 - \beta^2}{2\beta} \\
a_i &= c_i = -\rho A_i^{n+1/2}, \\
b_i &= 2(1 + \rho A_i^{n+1/2}) - h B_i^{n+1/2}, \\
d_i &= \left[2(1 - \rho A_i^{n+1/2}) + h B_i^{n+1/2} \right] \psi_i^n + \rho A_i^{n+1/2} (u_{i-1}^n + u_{i+1}^n)
\end{aligned} \tag{4.21}$$

Once the field is known at grids $n=1..N$ along the x-axis, on plane i along the z-axis, the field on plane $i+1$, which is the next plane along the z-axis, can be calculated using Equation (4.20). Thus, the propagating field can be calculated along the z-axis [51]. Equation (4.20) can be used to calculate the field in $O(N)$ operations, where N is the number of grid points in x .

Since the field can only be represented in a finite computational domain ($i = 1..N - 1$), when the above equation is applied at the boundary points $i=0$ and N , it requires the knowledge of unknown quantities outside the domain. These unknown quantities are replaced by appropriate boundary conditions to complete the system of equations. Proper choice of these boundary conditions is critical. In case of a poor choice, it can cause artificial reflection of light incident on the boundary back into the computation domain. The transparent boundary condition is used in *BeamPROP*[™] implementation of BPM. More details can be found in [52].

4.3.3. Wide angle extension to FD-BPM

The paraxial approximation used to carry out the BPM derivation restricts the application of BPM to straight waveguides or waveguides with large bands, as well as restrictions on index contrast and multimode propagation. The cause for the restriction is the elimination of the second derivative term in Equation (4.17). By including the second derivative term at the start of derivation, the paraxial approximation can be relaxed. Various extensions known as Wide-angle BPM have applied this approach successfully to relax the restriction of paraxiality. The Pade-based wide-angle technique is most popular and is used in *BeamPROP*[™]. It is reviewed below.

Consider the slowly varying field in Equation (4.17):

$$\frac{\partial^2 u}{\partial z^2} + 2i\beta \frac{\partial u}{\partial z} + \frac{\partial^2 u}{\partial x^2} + \frac{\partial^2 u}{\partial y^2} + (k^2 - \beta^2)u = 0 \quad (4.17)$$

Let D be the differential operator denoting $\partial/\partial z$, and let D^2 represent $\partial^2/\partial z^2$. The slowly varying envelope can be expressed as

$$D^2 u + 2i\beta D u + \left(\frac{\partial^2}{\partial x^2} + \frac{\partial^2}{\partial y^2} + (k^2 - \beta^2) \right) u = 0 \quad (4.22)$$

The formal solution for the first derivative can be found by putting aside u and solving a quadratic equation for D [53]. After substituting back u , the formal solution for the first derivative is given as,

$$\begin{aligned} \frac{\partial u}{\partial z} &= i\beta \left(\sqrt{1+P} - 1 \right) u, \\ P &= \frac{1}{\beta^2} \left(\frac{\partial^2}{\partial x^2} + \frac{\partial^2}{\partial y^2} + (k^2 - \beta^2) \right) \end{aligned} \quad (4.23)$$

The above equation only gives the one-way propagation solution. It is one of the two possible solutions to the quadratic equation for D . The backward solution can be found by changing the sign of the square root term. Either solution is exact. There is no approximation involved in this derivation. To solve for u , the radical in the first derivative solution needs be approximated. Pâdé expansion has been found to have best accuracy with fewest terms applied [53]. Using Pâdé approximation, the first derivative can be written as

$$\frac{\partial u}{\partial z} = i\beta \frac{N_m(P)}{D_n(P)} u \quad (4.24)$$

Here N_m and D_n are polynomials in terms of the operator P . The set (m, n) gives the order of the Pâdé approximation. Examples of the first few terms of the Pade expansion are given below.

Table 4.2 The first few terms of Pâdé expansion [12].

Order(m,n)	N_m	D_n
(1,0)	$P_1/2$	1

(1,1)	$P_1/2$	$1+P_1/4\beta$
(2,2)	$P_1/2+\beta P_2/4$	$1+3P_1/4\beta+P_2/16$

where $P_1 = \frac{P}{\beta}$ and $P_2 = \frac{P^2}{\beta^4}$.

As the Pâd  order increases, the accuracy of the solution improves. The (1, 1) order Pâd  approximation is highly accurate up to 30 deg while the (3, 3) Pâd  approximation is equivalent to the 15th order Taylor expansion of the exact square root term in Equation (4.23). Therefore, this approach can be employed to analyze large propagation angle, high reflective index contrast, and complex mode structures in waveguides and free space.

4.3.4 Vectorial extension of FD-BPM

Polarization effects can be included in the BPM when the electric field E is introduced as a vector. Instead of scalar Helmholtz equation, the derivation can be started from the vector wave equation [54]. In terms of the transverse field components, the set of coupled equations for the slowly varying field are given as

$$\begin{aligned}\frac{\partial u_x}{\partial z} &= A_{xx}u_x + A_{xy}u_y \\ \frac{\partial u_y}{\partial z} &= A_{yx}u_x + A_{yy}u_y\end{aligned}\tag{4.25}$$

The A_{ij} 's are complex differential operators given by

$$\begin{aligned}A_{xx}u_x &= \frac{i}{2\beta} \left\{ \frac{\partial}{\partial x} \left[\frac{1}{n^2} \frac{\partial}{\partial x} (n^2 u_x) \right] + \frac{\partial^2}{\partial y^2} u_x + (k^2 - \beta^2) u_x \right\} \\ A_{yy}u_y &= \frac{i}{2\beta} \left\{ \frac{\partial}{\partial y} \left[\frac{1}{n^2} \frac{\partial}{\partial y} (n^2 u_y) \right] + \frac{\partial^2}{\partial x^2} u_y + (k^2 - \beta^2) u_y \right\} \\ A_{yx}u_x &= \frac{i}{2\beta} \left\{ \frac{\partial}{\partial y} \left[\frac{1}{n^2} \frac{\partial}{\partial x} (n^2 u_x) \right] - \frac{\partial^2}{\partial y \partial x} u_x \right\} \\ A_{xy}u_y &= \frac{i}{2\beta} \left\{ \frac{\partial}{\partial x} \left[\frac{1}{n^2} \frac{\partial}{\partial y} (n^2 u_y) \right] - \frac{\partial^2}{\partial x \partial y} u_y \right\}\end{aligned}\tag{4.26}$$

The operators A_{xx} and A_{yy} are related to polarization dependence due to different boundary conditions at interfaces, and address effects of different propagation constants, field shapes, bend loss for TE and TM fields. The off-diagonal terms A_{xy} and A_{yx} relate to polarization coupling and hybrid modes due to geometric effects, for instance, the influence of corners or sloping walls in the cross-sectional structure. The above equations are generally known as the full-vectorial BPM. The simplification $A_{xy}=A_{yx}=0$ is called semi-vectorial BPM, which eases the computation load significantly. In most cases, the coupling of the polarization fields is very weak, so the semi-vectorial BPM provides excellent results.

4.4 Simulation Results

4.4.1 Interpretation of simulation results

The simulation results are obtained by detecting the power output at each output port (waveguide) while a light source with fixed power scans through designated wavelength range at the input of the AWG. Power readings from different output ports are plotted with different colors over the wavelength axis. The simulations are set up to illustrate the effect of eliminating high order harmonics using ISZC AWG device.

Regular AWG's are grating devices, which have repeated harmonics orders. The range of output repetition in wavelength or frequency is called the FSR. When the range of input wavelength moves beyond FSR, different harmonic orders overlap with one another, as illustrated in Figure 4.11. Therefore, the range of input wavelength is limited by the FSR for regular AWG. The ISZC AWG devices greatly reduce the power of high order harmonics, thus effectively extending FSR to the infinity. In this way, the limit on the range of the input wavelength by the FSR is eliminated. Figure 4.11 shows an example of the output field of a regular AWG. The output is displayed in harmonic orders, and input wavelengths beyond the FSR are added. As shown, if new wavelengths outside FSR are introduced, the AWG output port will have overlapping outputs. When plotted along the wavelength axis using different colors to indicate output ports, same wavelengths, may have two peaks of different color and same color lines may have

double peaks, indicating same wavelength coming out from different output ports and same outputs producing light signals of different wavelengths.

The ISZC AWG devices are designed by modifying regular AWG's. The benefit is to remove the limit of FSR. So when wavelengths beyond the original FSR of regular AWG are applied at the input, no overlapping outputs would appear at output port. If the number of the output ports were same as the original AWG, the wavelengths outside the FSR of the AWG, which is applied at the input of an ISZC AWG would not appear in the output. If additional output ports are attached at the ISZC AWG's output coupler, the wavelengths outside the original FSR can be guided to the output. In the following section, simulations are performed to demonstrate these propositions.

4.4.2 Simulation results for 200 channel ISZC AWG

Two sets of simulations are presented here. The first simulation presents a 28 channel ISZC AWG design based on a 24 channel regular AWG. The second is a simulation of a 200 channel ISZC AWG based on a 180 channel regular AWG design. The first simulations illustrate the overlapping of wavelengths at the output, when additional wavelength channel beyond the FSR is scanned at input, and the elimination of high order diffraction achieved by ISZC AWG. The second set of simulations shows the result of carrying the principle to high channel count applications, converting a 180-channel regular AWG into a 200 channel ISZC AWG.

Figures 4.12 to 4.18 show the layout of a regular/ISZC AWG including the device as whole and individual sections. The ISZC AWG has similar layouts as a regular AWG, and uses same parameters; the irregularly spaced arrayed waveguide section is what differentiates a regular AWG from an ISZC AWG. This is emphasized in a close up view of the arrayed waveguide section in Figure 4.18.

Figures 4.19 to 4.21 show the results of converting a regular 24 channel AWG device to a 28 channel ISZC AWG by adding 4 more wavelength channels. Simulations are carried out to show the frequency overlapping when 4 additional output ports are present and input field scans the entire 28 wavelength channels. The physical parameters are: coupler radius $R=8.4\text{mm}$, grating order=40, number of waveguides=100, arrayed

waveguide spacing=20_μm, output waveguide spacing=18.5_μm, waveguide width=6_μm, and $\lambda = 1.6\text{nm}$. All simulations of 24/28-channel regular/ISZC AWG use these parameters. In figure 4.19, the input field scans 4 extra wavelength channels into the 24 channel regular AWG, with 4-output port to couple the extra wavelength channels. 4 outputs at both ends of the spectrum containing overlapping wavelengths are present. This is illustrated in Figure 4.11. Figures 4.20 and 4.21 plot the transmission spectrum of the ISZC AWG with 24 and 28 output ports attached to the output coupler. In both simulations 28 wavelength channels were scanned. Figure 4.11 shows the elimination of high order diffraction, i.e. eliminating FSR. Figure 4.21 shows the ability of ISZC to function normally in wavelength demultiplexing for the additional 4 wavelength channels. The full functionality of an ISZC AWG is demonstrated in Figures 4.19 to 4.21, namely providing wavelength demultiplexing without FSR. Currently, this function comes at a cost of losing about 10dB in output signal strength.

In Figures 4.22 to 4.31, a 180-channel regular AWG is converted to an ISZC AWG. The parameters for the regular/ISZC AWG pair are: Coupler radius $R=61.8\text{mm}$, Grating order=29, Number of waveguides=400, Arrayed waveguide spacing=20_μm, Output waveguide spacing=18.5_μm, Waveguide width=6_μm, and $\lambda = 0.3\text{nm}$. In order to achieve high channel count the Coupler radius is fairly high compared to 3~36mm in general AWG design [32]. This may due to the extreme low grating order. Attempts have been made to try different parameters, but are unsuccessful. Grating order is determined by *BeamPROP*TM, and we are not able to alter the software to generate more desirable parameters. As in Figures 4.19 to 4.21, the capability of ISZC AWG to eliminate FSR and function as a wavelength demultiplexer in high channel count application is demonstrated. *BeamPROP*TM regularly can only support up to 140 channels. After working with the vendor, we are able to increase channel count to 200. Due to the limit on the size of coupler, currently 210 or more channels are not possible to be implemented on *BeamPROP*TM. Overall currently, there is still a 10dB power tradeoff to apply the method of ISZC to high channel count AWG design to eliminate FSR of a regular AWG.

4.4.3. Conclusions

In this chapter the design procedure of ISZC AWG devices using Rsoft BPM software is presented. The ISZC AWG design eliminates the high harmonic diffractions caused by the grating patterns of the regular AWG, and greatly extends the FSR of original AWG. Simulation results of ISZC AWG based on the regular AWG design demonstrated the removal of high order diffractions. The limiting factor of channel count to ISZC AWG demultiplexers becomes the envelope of the overall intensity profile and the width of each wavelength channel. This issue is further explored in the following chapter to determine the maximum channel count available to an ISZC AWG demultiplexer. We note this is not a fundamental limitation, and can be externally eliminated by making output-coupling apertures very small.

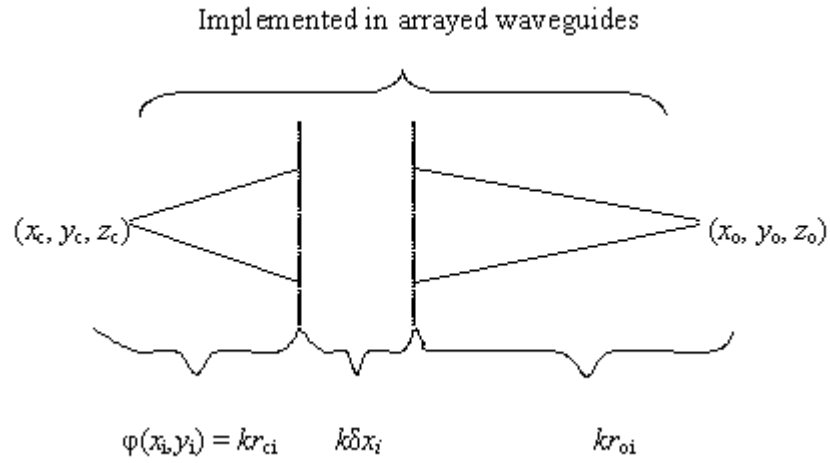


Figure 4.1. Implementing a virtual spherical modulation in the arrayed waveguide

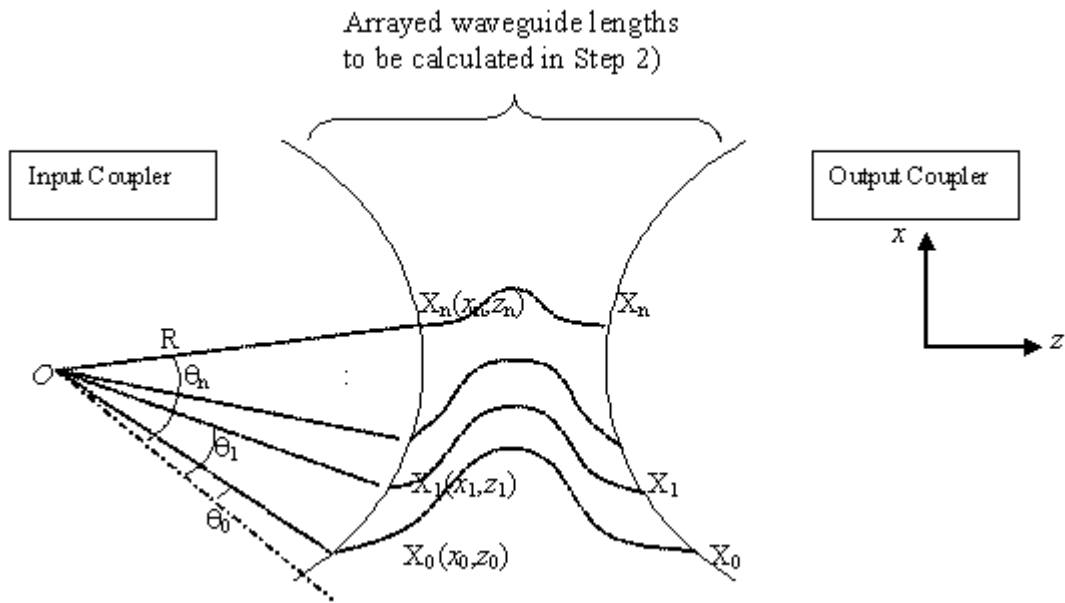


Figure 4.2. Setting up of random points

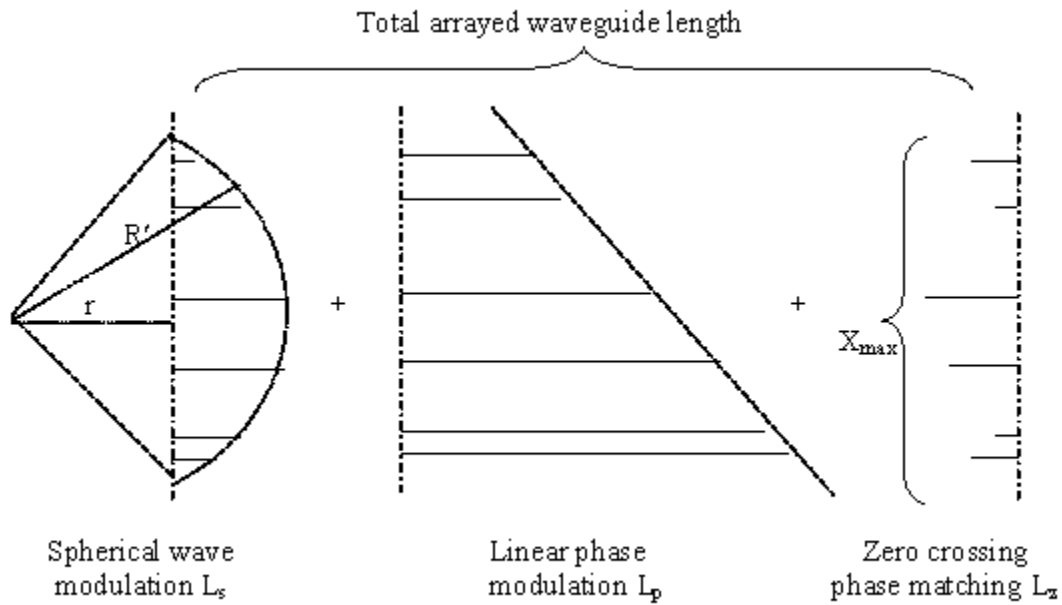


Figure 4.3. Sections of ISZC modified arrayed waveguide lengths.

Arrayed Waveguides

Two constraint options are generated when the layout is specified. Design, and some internal, parameters are shown. Parameter specifications are symmetric about cross section at the z midpoint, although their values may be different between the input and output sides. Parameters with a '1' on the end apply to only the 1st waveguide in the array. Similar parameters exist for the other waveguides as well.

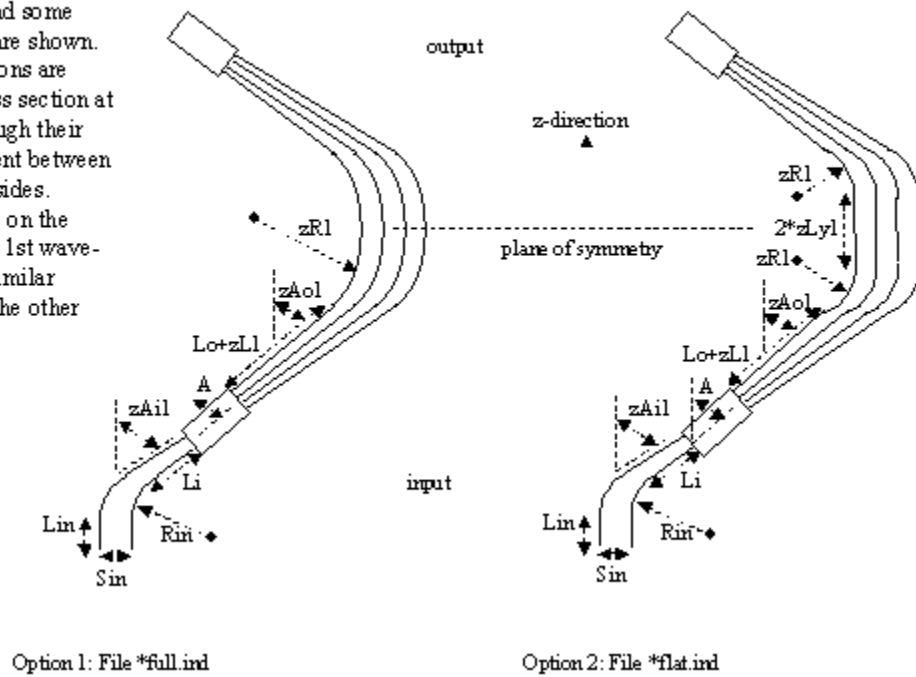


Figure 4.4. Layouts for AWG device [45].

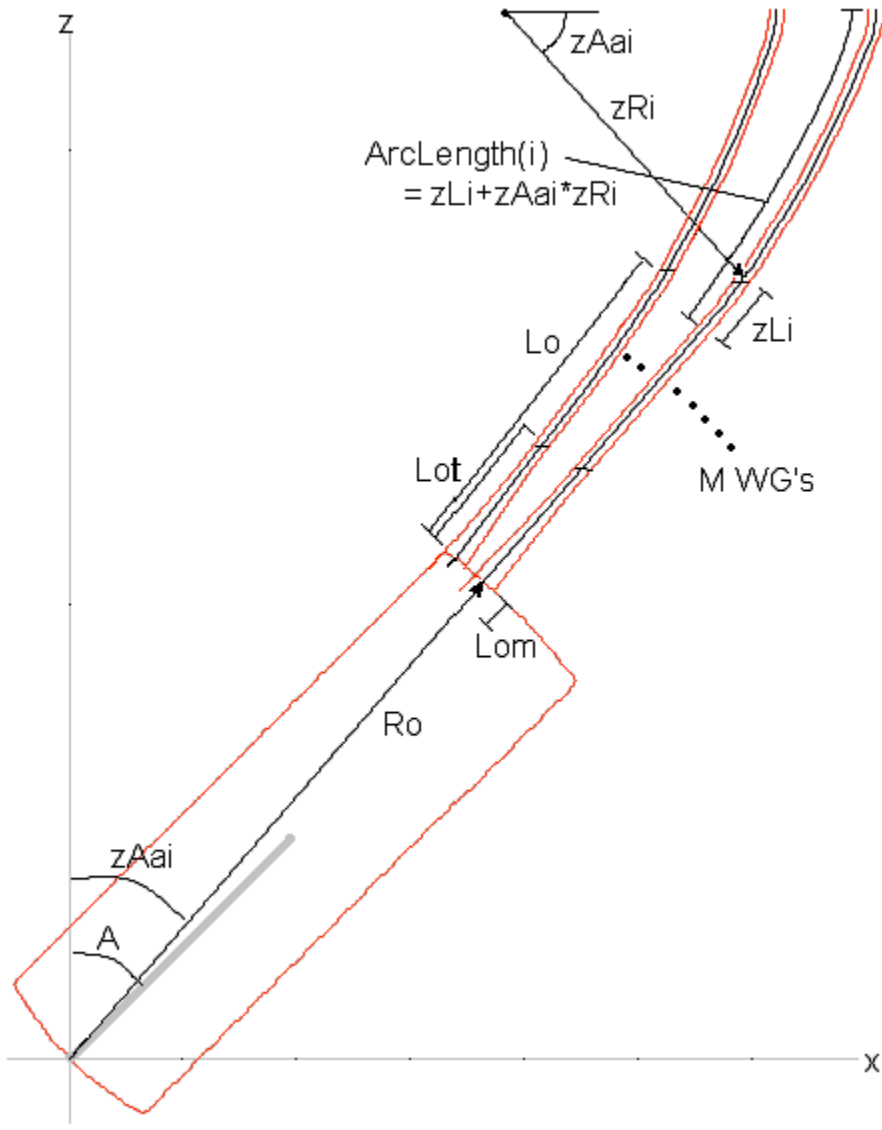


Figure 4.5. Array Design for Full Layout [45].

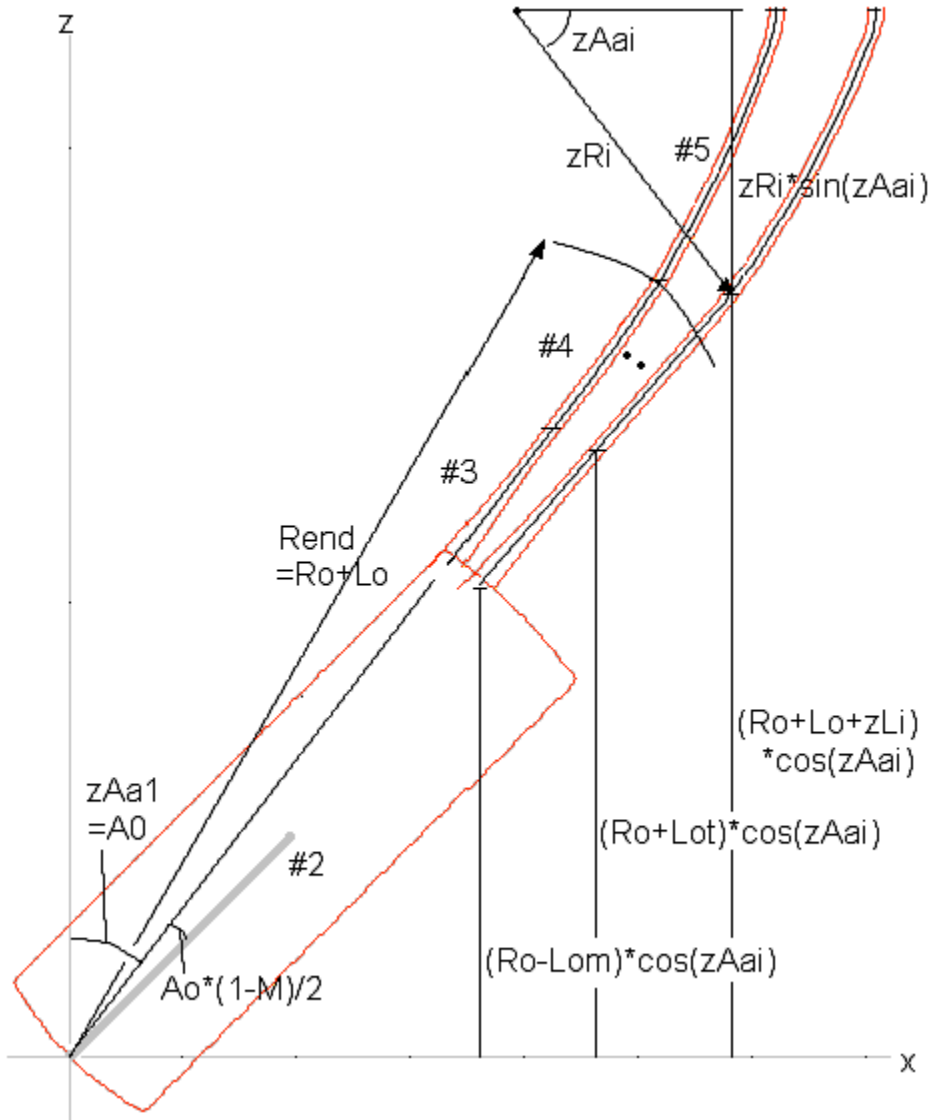


Figure 4.6. Array Design for Full Layout [45].

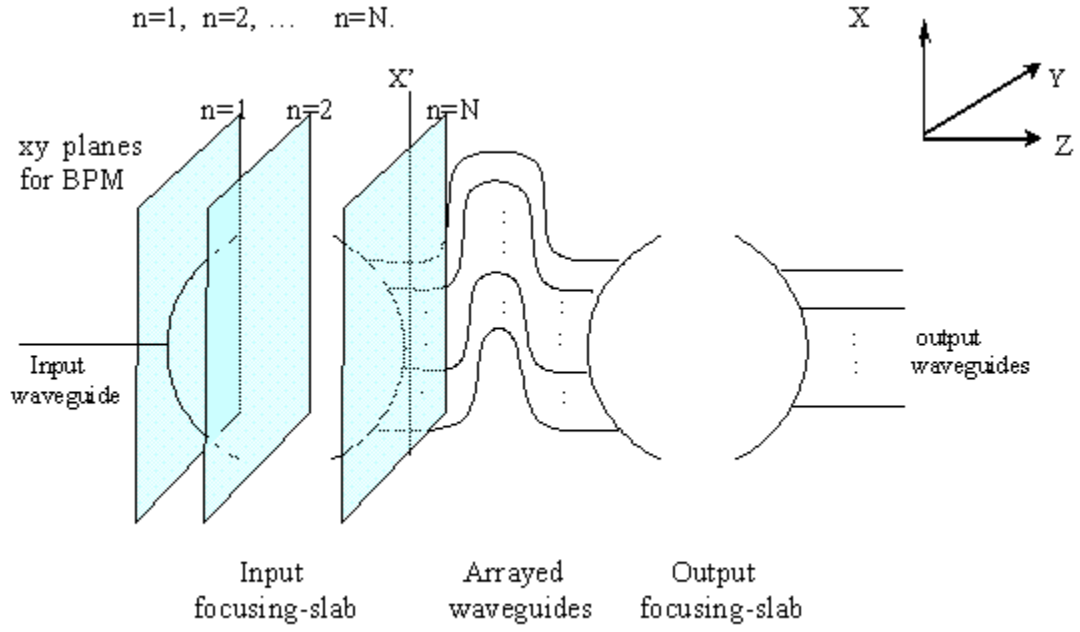


Figure 4.7. Domain of BPM Calculation.

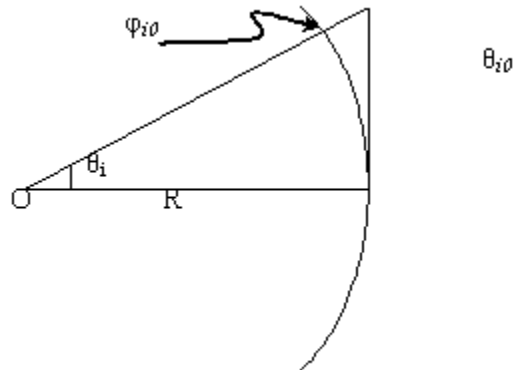


Figure 4.8. Geometry for calculating initial phase in arrayed waveguides.

WDM Router Script File Generator

Simulate Both Stars: Layout File Meta Prefix:

Phase Error (degrees): # Input Ports:

Design Info File: # Output Ports:

Points per Channel: # Wavelength Channels:

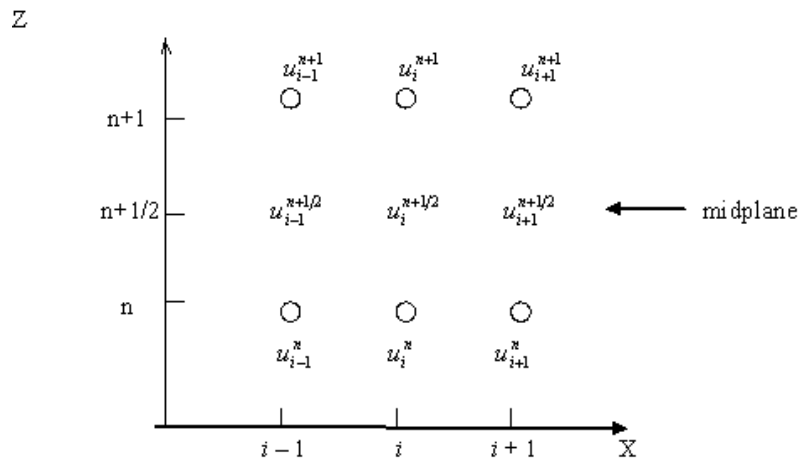
Starting Channel: Center Wavelength (um):

Ending Channel: Channel Spacing (um):

Script File Meta Prefix:

OK Cancel

Figure 4.9. The input window for **WDM Router Description File Generator**.



$$\left. \frac{\partial u_i}{\partial z} \right|_{z=n+\frac{1}{2}} = \frac{u_i^{n+1} - u_i^n}{\Delta z}$$

$$\left. \frac{\partial^2 u_i}{\partial x^2} \right|_{z=n+\frac{1}{2}} = \frac{\partial^2}{\partial x^2} \left(\frac{u_i^{n+1} + u_i^n}{2} \right) = \frac{\delta^2 u_i^{n+1} + \delta^2 u_i^n}{2\Delta x^2}$$

Figure 4.10. Crank-Nicholson method (CN)

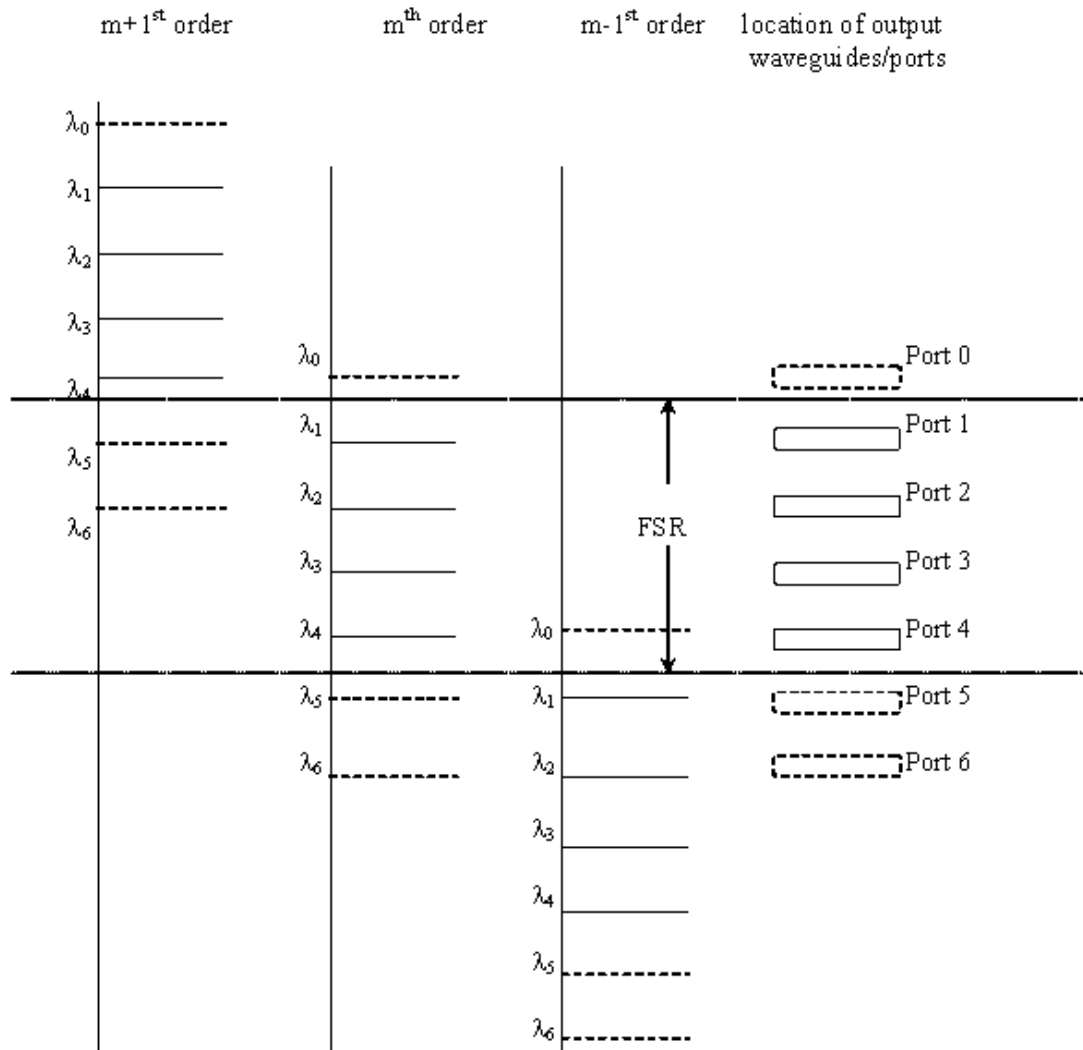


Figure 4.11. Illustration of diffraction orders for AWG output
(The dashed lines represent wavelengths outside of FSR).

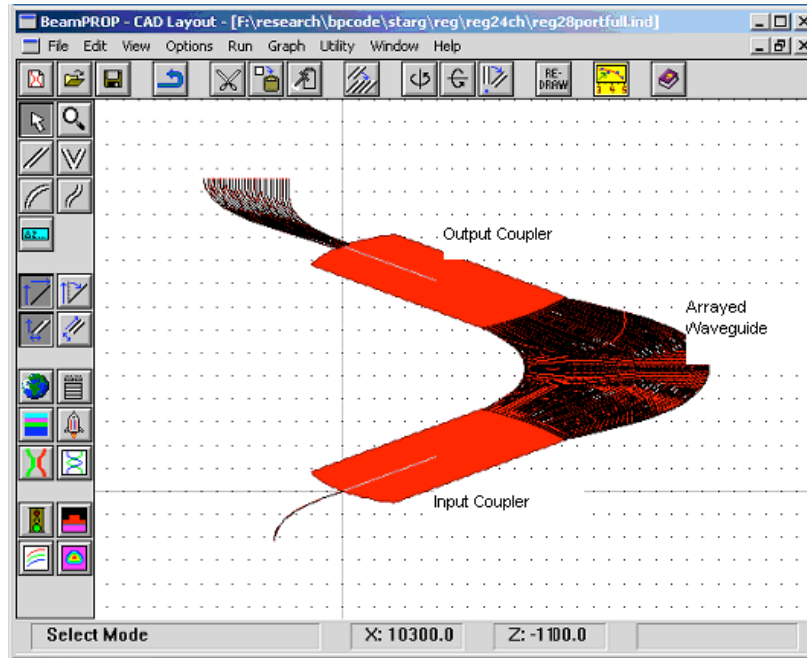


Figure 4.12. Full layout of a 24 channel 100 waveguide regular AWG ($m=40$).

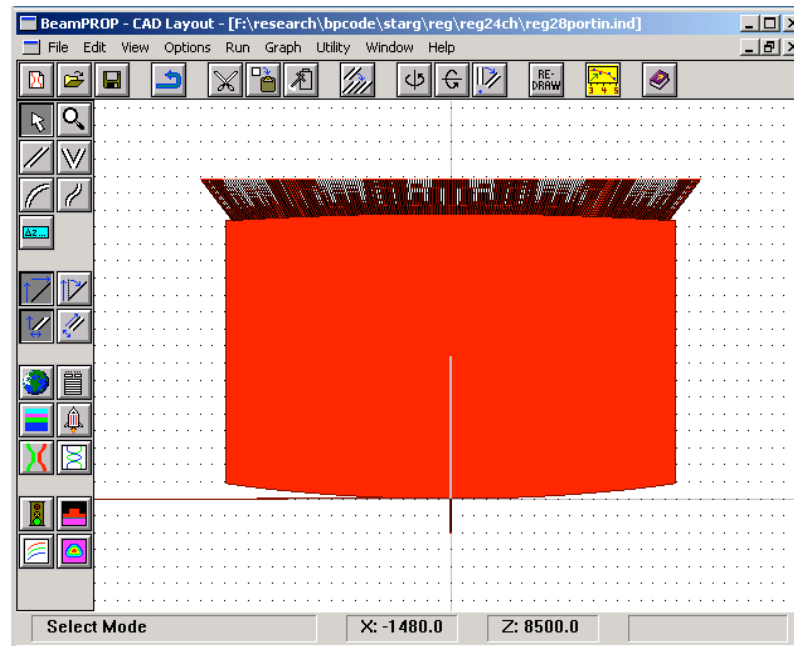


Figure 4.13. The input coupler of the 24-channel AWG.

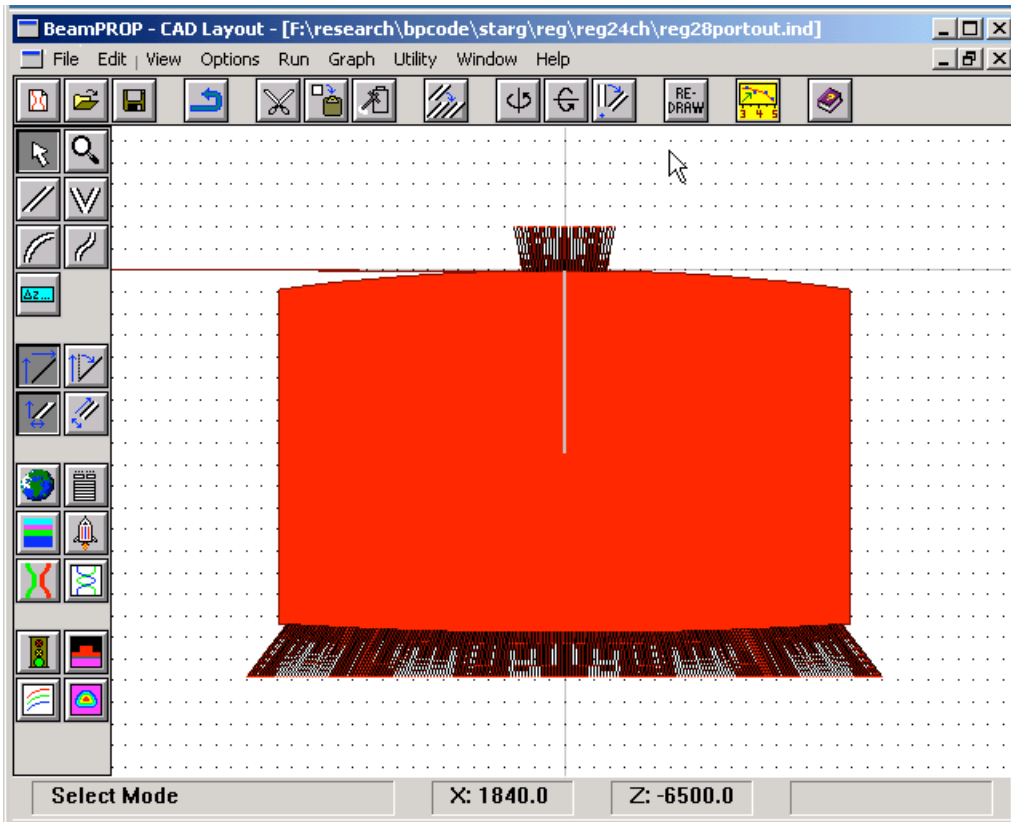


Figure 4.14. The output coupler of the 24 channel AWG.

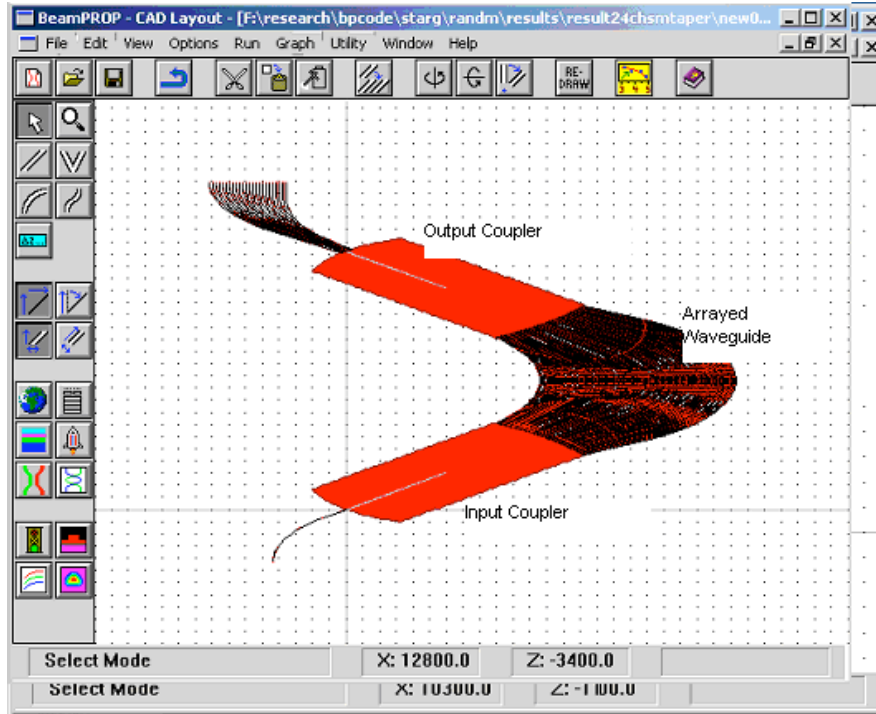


Figure 4.15. Full layout of ISZC AWG based on the 24 channel regular AWG.

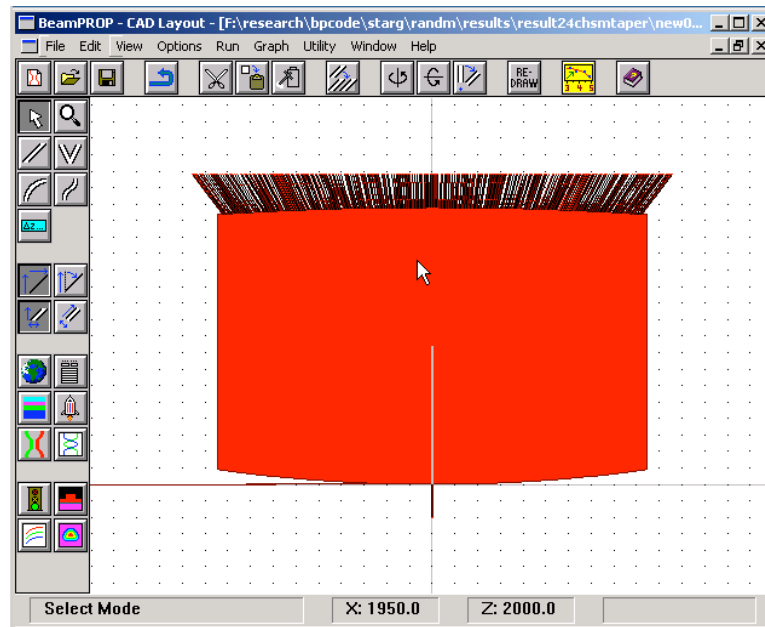


Figure 4.16. The input coupler of the ISZC AWG

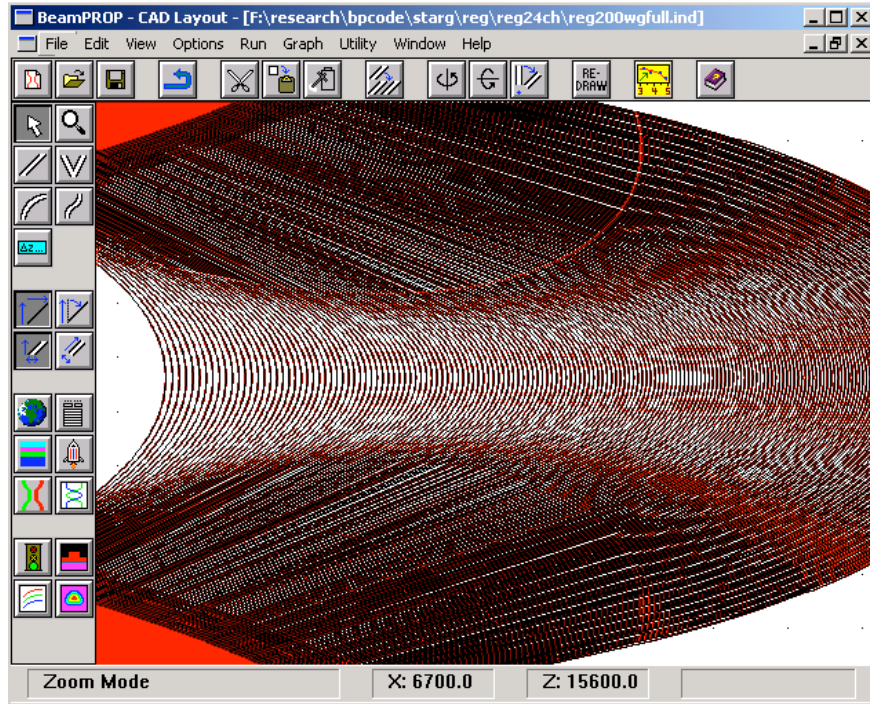


Figure 4.17. A close-up view of the AWG arrayed waveguide section.

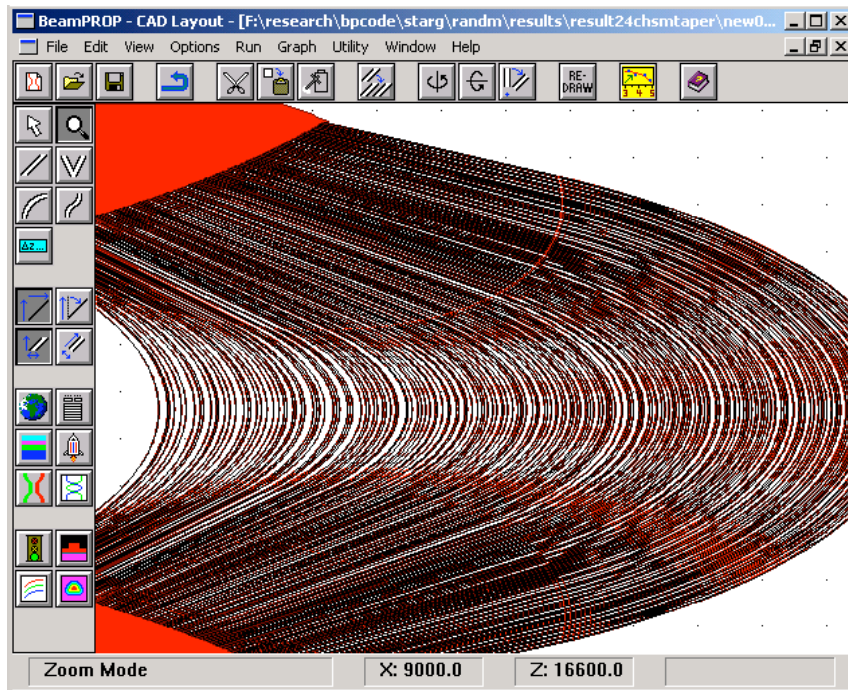


Figure 4.18. A close-up view of the ISZC AWG arrayed waveguide section.

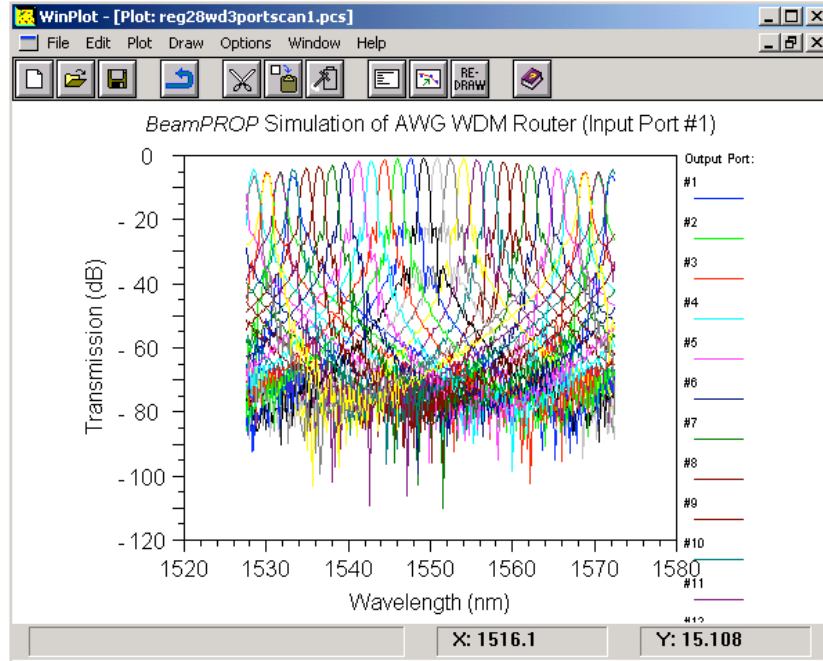


Figure 4.19. 24-channel AWG transmission spectrum scanned for 28 channels.

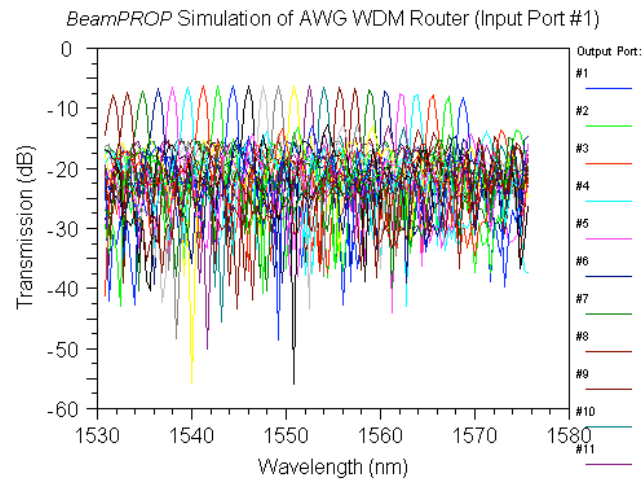


Figure 4.20. Transmission characteristic of the ISZC AWG with 24 output ports

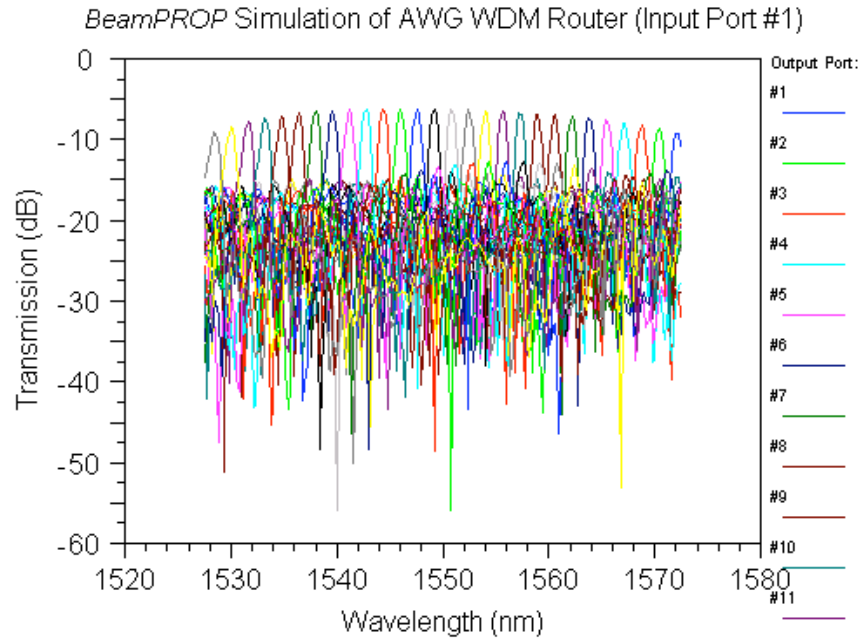


Figure 4.21. Transmission characteristics of the ISZC AWG with 28 output ports.

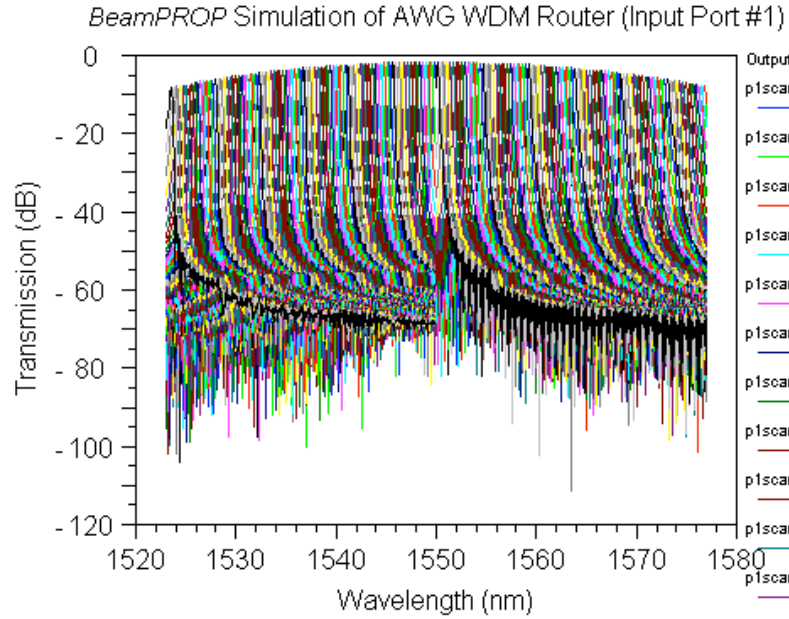


Figure 4.22. 180 channel 0.3 nm spacing regular AWG transmission spectrum.

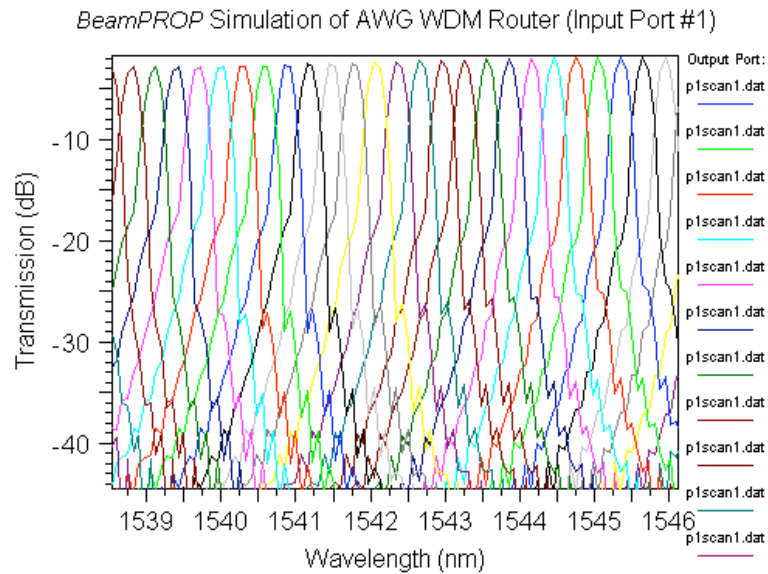


Figure 4.23 A closeup view of the 180 channel 0.3 nm spacing regular AWG transmission spectrum.

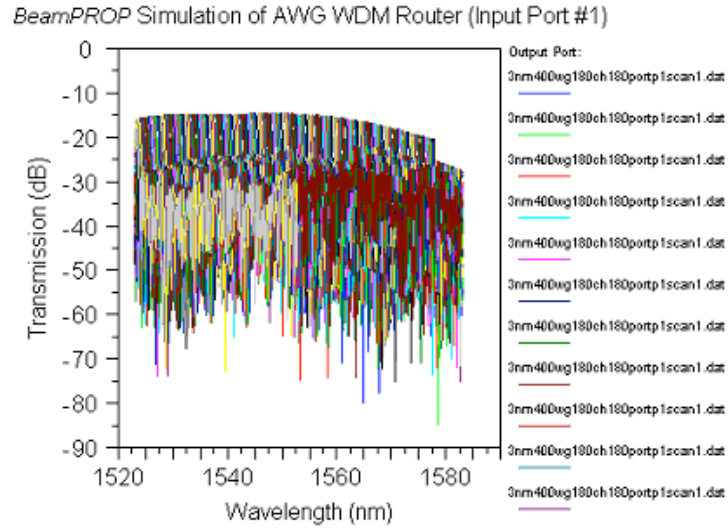


Figure 4.24. ISZC AWG based on 180-channel 0.3nm regular AWG with 180 output ports (200 channels scanned).

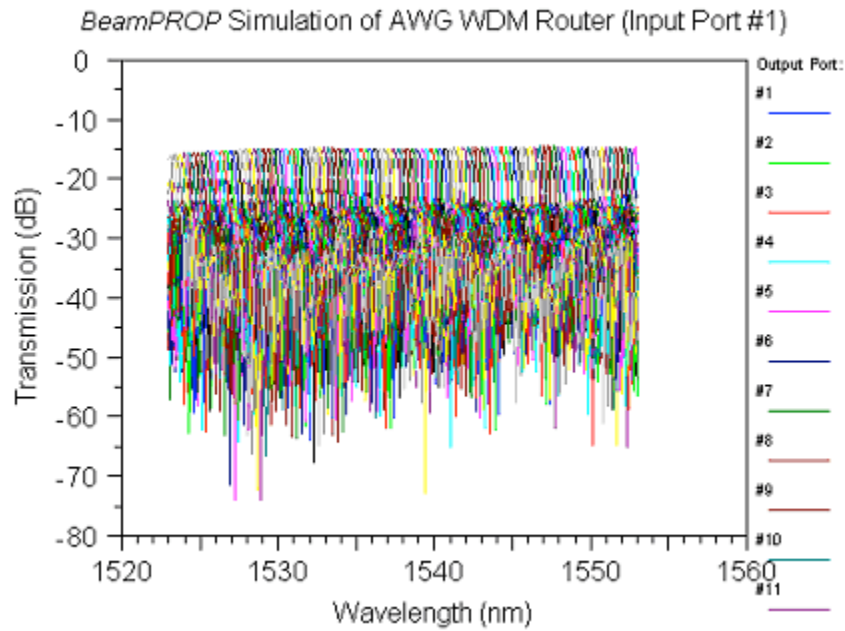


Figure 4.25. First 100 channels scanned for the ISZC AWG in Figure 4.24.

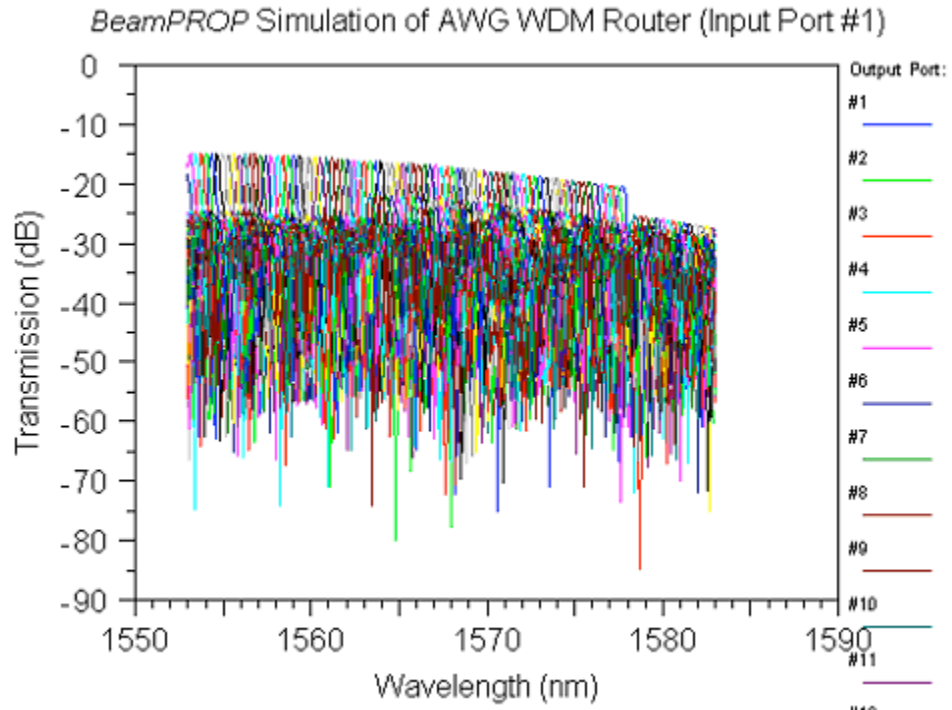


Figure 4.26. Rest of the 80 channels scanned for ISZC AWG in Figure 4.24.

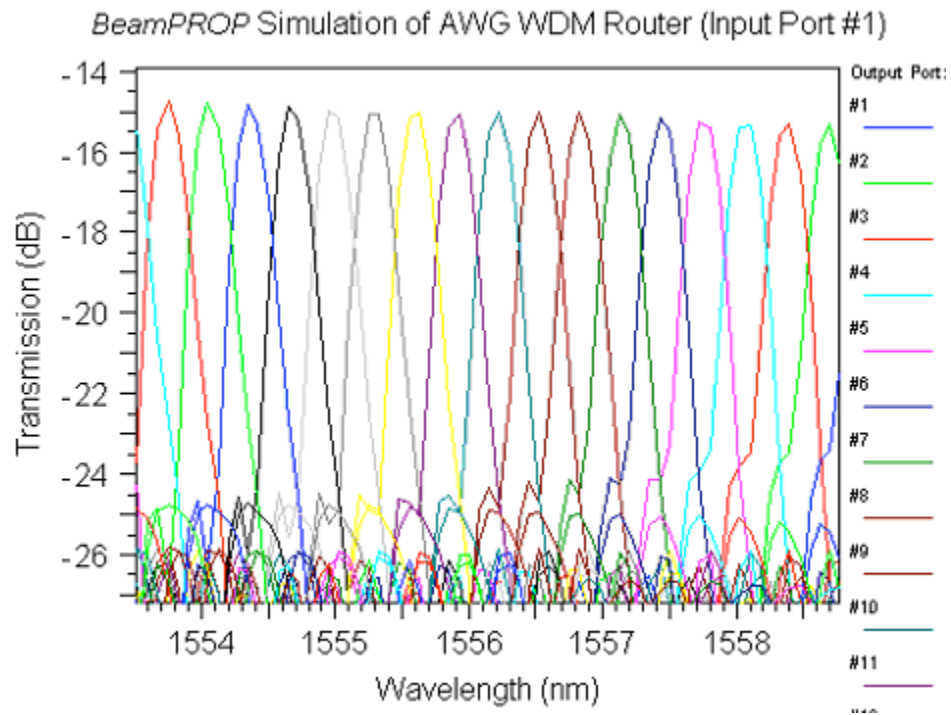


Figure 4.27. A close up view of 200 channel ISZC AWG with 180 output ports.

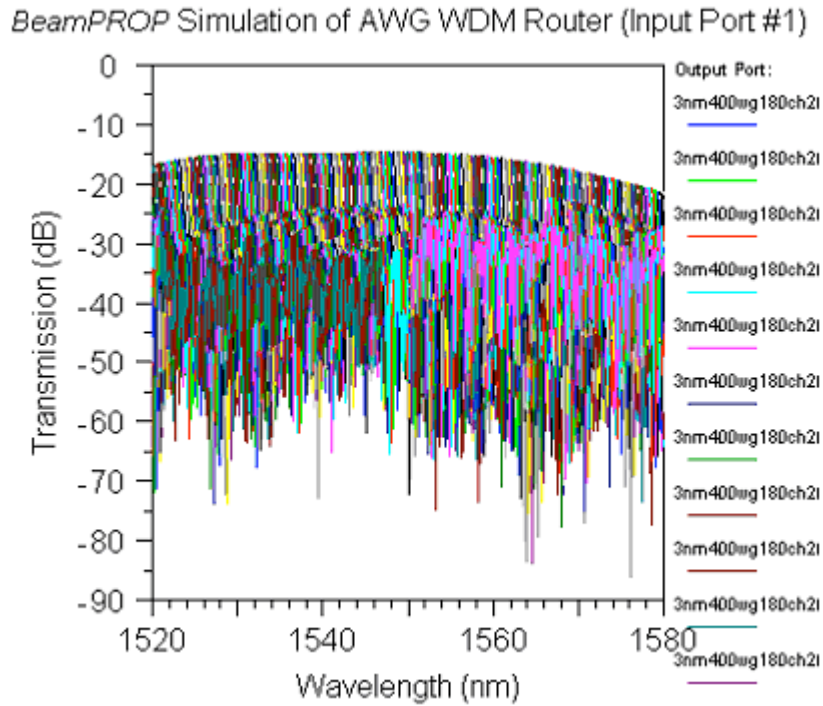


Figure 4.28. ISZC AWG based on the regular AWG in Figure 4.22 with 200 output ports
 200 channels scanned.

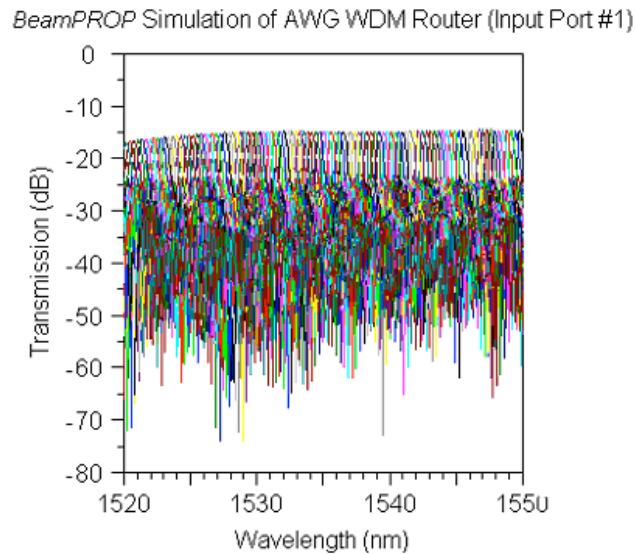


Figure 4.29. First half of the transmission spectrum shown in Figure 4.28 with the
 first 100 channels scanned.

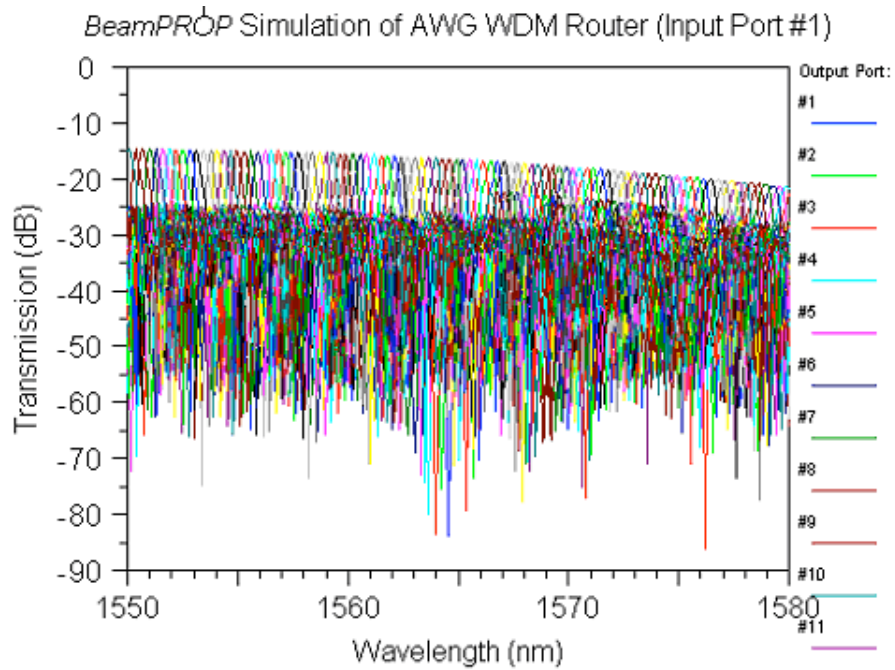


Figure 4.30. Second half of the transmission spectrum shown in Figure 4.28 with the second 100 wavelength channels scanned.

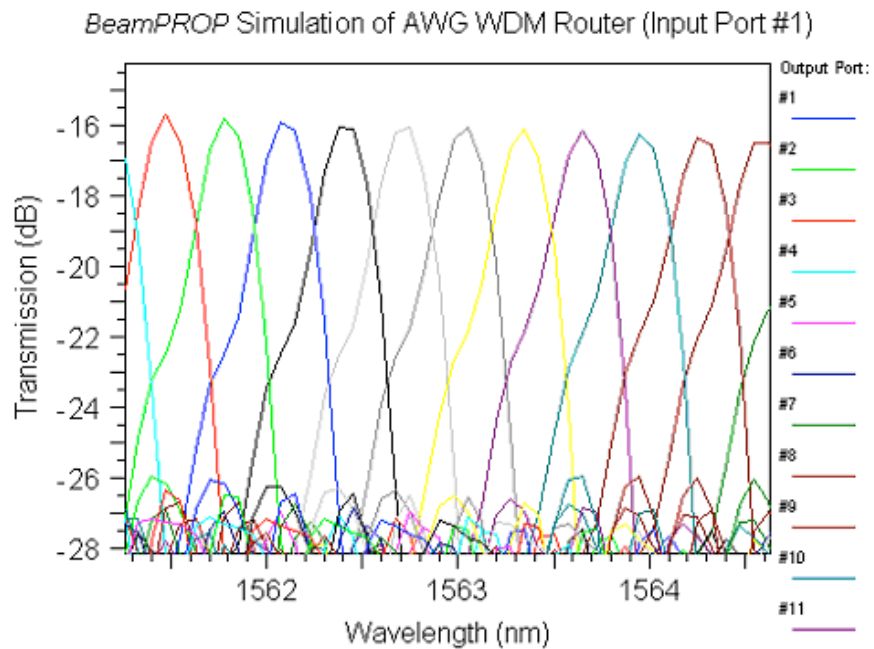


Figure 4.31. A close up view of 200 channel ISZC AWG

5. ISZC AWG NOISE AND CHANNEL CAPACITY CONSIDERATIONS

The main benefit of ISZC AWG design is the increased channel capacity by the elimination of the FSR. For a regular AWG, with respect to the center wavelength, the phase change between adjacent waveguides at their outputs is $2m\pi$. Since the input coupler physically matches the wavefront of the expanding field of the input wave, a plane wavefront is coupled into the arrayed waveguide. Therefore, a plane wavefront is reproduced at the arrayed waveguide output. In the process of applying MISZC, a spherical phase modulation is added to the arrayed waveguide section. At the end of the arrayed waveguide section, instead of the original plane phase front, a fast varying phase front is created, which produces abundant zero crossings. In this way, when a random location is picked for an arrayed waveguide, a zero crossing, which can both satisfy the phase match condition and generate wavelength dependent linear factor, can be found in a close by position. This is of key importance to focusing outputs of the arrayed waveguides in the output coupler, since all arrayed waveguides are placed on the circular curvature.

As we shall see in the following discussion, the wavelength dependent linear phase factor provides wavelength demultiplexing function through the spatial Fourier transform provided by the coupler geometry, which is present in both regular AWG design and ISZC AWG design. The previous discussion shows that, in ISZC AWG design, an additional phase factor is introduced to each arrayed waveguide to provide zero crossings for focusing purpose, when waveguide locations are randomly positioned. This nonlinear phase modulation turns harmonic images into noise in ISZC AWG design. In the following, the nature of wavelength demultiplexing is illustrated and the phase term that generates noise is discussed in detail. Then, channel capacity of ISZC AWG is derived using Fraunhofer diffraction approximation and the ratio of the AW count over

the maximum channel count is obtained for comparing channel capacity of an ISZC AWG and a regular AWG with same number of AW's.

5.1 Noise Considerations

As discussed previously, the noise in the ISZC AWG output is mainly due to the additional phase modulation in the arrayed waveguide section, after the diffraction process in the output coupler, which can be accurately modeled as a Fourier transform. To investigate the noise in the output of ISZC, we first establish the field at the output of the arrayed waveguides, then proceed to take the Fourier transform in space. The fields at AW/OC interface are a series of Gaussian mode amplitude profiles affected by two factors, a spatial function that describes the location of each arrayed waveguide, and a complex phase function that describes the phase change in each arrayed waveguide.

The overall phase change in the i^{th} arrayed waveguide is given in Equation (3.29). Adjusting the wave number in free space k^1 to wave number in waveguide k_w^1 due to implementation in waveguide for the center wavelength λ_1 , this equation is repeated below

$$k_w^1 r_{ci} + k_w^1 x_i \alpha + k_w^1 r_{oi} = 2n\pi \quad (5.1)$$

k_w^1 is wave number inside waveguide, x_i is the waveguide section generating wavelength dependent phase shift, r_{ci} and r_{oi} together provide zero crossing phase match condition. So we define for m^{th} wavelength the phase factor S_i^m as,

$$S_i^m = \exp(jk_w^m x_i \alpha) \exp(jk_w^m r_i) \quad (5.2)$$

$$r_{ci} + r_{oi} = r_i$$

The superscript stands for the wavelength index, subscript stands for the waveguide index. S_i^m stands for the complex phase factor induced by the m^{th} wavelength in the i^{th} waveguide for M input wavelengths and P waveguides as shown in Figure 5.1.

In Figure 5.1, the IC/AW interface is the arc on the left. Fields in the OC propagates from the left to the right, and the OC is in the confocal geometry. Since the radial angle of the arc is small ($<10^\circ$), as discussed in section 2.3, the fields at the right arc (assigned as the x-axis) and the left arc (assigned as the y-axis) are related by the Fourier transform. The field on the AW/OC interface (the left arc) consists of identical

Gaussian mode profiles located at x_i 's with initial phase determined by S^m_i . The Gaussian amplitude profiles can be expressed by the convolution of a summation of Kronecker delta functions and the Gaussian mode function. Thus, the field at the AW/OC interface is modeled as a double summation over wavelength and x_i 's. Then, we can write $h(x)$, the field at the end of the arrayed waveguides as

$$\begin{aligned}
 h(x) &= \sum_{m=1}^M \sum_{i=1}^P g(x - x_i) \exp(jk_w^m x_i \alpha) \exp(jk_w^m r_i) \\
 &= \sum_{m=1}^M \left(\sum_{i=1}^P \exp(jk_w^m x_i \alpha) \exp(jk_w^m r_i) \delta(x - x_i) \right) \otimes g(x) \\
 g(x) &= E_o \exp\left(-x^2/w^2\right) \\
 x_i &= (i-1) \cdot \Delta x + u_i \cdot \Delta x
 \end{aligned} \tag{5.3}$$

u_i is a random number uniformly distributed in (0, 1), and $g(x)$ is the Gaussian mode profile; w is the effective waveguide width. Note that, in Equation (5.3), r_i is defined the same as in Equation (5.1) for the center wavelength λ_1 ; the total net phase change in every waveguide is integer multiples of 2π . This is not the case for other wavelengths in general, since r_i are constants, and are only calculated for the center wavelength. Due to the nonlinear nature of the complex phase function, this phase factor can be considered random for all other wavelengths. Using the property of the Kronecker delta function, the discrete phase factor related to waveguide section x_i can be expressed as a continuous function. Thus, we write

$$\begin{aligned}
 h(x) &= \sum_{m=1}^M \left[\exp(jk_w^m x \alpha) \left(\sum_{i=1}^P q(x) \exp(jk_w^m r_i) \right) \right] \otimes g(x) \\
 q(x) &= \delta(x - x_i) \\
 x_i &= (i-1) \cdot \Delta x + u_i \cdot \Delta x
 \end{aligned} \tag{5.4}$$

k_w^m is the wave number inside waveguide for the m^{th} wavelength, and the m^{th} wavelength is give as

$$\lambda_m = \lambda_1 + (m-1) \cdot \Delta \lambda \tag{5.5}$$

Assume the chromatic (total) dispersion in the waveguide is linear shown in Figure 5.2. We write

$$k_w^m = \left. \frac{\partial k_w^m}{\partial \lambda} \right|_{\lambda=\lambda_i} \cdot (m-1) \cdot \Delta\lambda + k_w^1 \quad (5.6)$$

Given $\left. \frac{\partial k_w^m}{\partial \lambda} \right|_{\lambda=\lambda_i} = \xi$. Then, the field at the output of the arrayed waveguide can be expressed as

$$h(x) = \sum_{m=1}^M \left[\exp \left\{ j \left[\xi (m-1) \cdot \Delta\lambda + k_w^1 \right] x \alpha \right\} \left(\sum_{i=1}^P q(x) \exp(jk_w^m r_i) \right) \right] \otimes g(x) \quad (5.7)$$

The Fourier transform of Equation (5.7) is given by

$$FT \{h(x)\} = \sum_{m=1}^M \left[FT \left\{ \exp \left[j \left(\xi (m-1) \cdot \Delta\lambda + k_w^1 \right) x \alpha \right] \right\} \otimes FT \left\{ \sum_{i=1}^P q(x_i) \exp(jk_w^m r_i) \right\} \right] \cdot FT \{g(x)\} \quad (5.8)$$

It's simple to obtain the Fourier transform of the first term inside summation over variable m ,

$$FT \left\{ \exp \left[j \xi \left((m-1) \cdot \Delta\lambda + k_w^1 \right) x \alpha \right] \right\} = \delta \left(f_x - \frac{(m-1) \cdot \Delta\lambda}{2\pi} \xi \alpha + \frac{k_w^1 \alpha}{2\pi} \right) \quad (5.9)$$

Therefore the Fourier transform of the Gaussian mode function determines the overall amplitude envelope. In most cases, since the width of the waveguide is small, the Fourier transform of the Gaussian mold function is broad. As a result, its effect to cross talk can largely be ignored. Equations (5.8) and (5.9) show the wavelength demultiplexing is accomplished by the wavelength dependent linear phase term in Equation (5.7). As long as the chromatic dispersion is linear, the output noise can be considered to be due to the Fourier transform of the term inside the second summation in Equation (5.8). It is defined below as

$$\varphi(x) = \sum_{i=1}^P q(x) \exp(jk_w^m r_i) \quad (5.10)$$

$\varphi(x)$ is random in nature; it contributes to the noise in ISZC output. To find the spectral content of $\varphi(x)$, we first calculate $R_\varphi(t)$ the autocorrelation function of $\varphi(x)$, then its power spectral density function can be expressed as $FT \{R_\varphi(t)\}$. We have

$$\begin{aligned}
R_\varphi(t) &= E\left\{\varphi(x) \cdot \varphi^*(x+t)\right\} = E\left\{\sum_{i=1}^P q(x) \exp(jk_w^m r_i) \sum_{l=1}^P q(x+t) \exp(-jk_w^m r_l)\right\} \\
&= \sum_{i=1}^P \sum_{l=1}^P E\left\{q(x) \cdot q(x+t) \cdot \exp(jk_w^m r_i) \cdot \exp(-jk_w^m r_l)\right\}
\end{aligned} \tag{5.11}$$

Since, $x_i = (i-1) \cdot \Delta x + u_i \Delta x$, x_i 's are a series of random locations placed in the bins of Δx in size on the real axis as illustrated in Figure 5.3.

Given that x_i 's and r_i 's are independent, we write

$$\begin{aligned}
R_\varphi(t) &= \sum_{i=1}^P \sum_{l=1}^P E[q_i(x) \cdot q_l(x+t)] \cdot E[\exp(jk_w^m r_i) \cdot \exp(-jk_w^m r_l)] \\
q_i(x) &= \delta(x - x_i) \\
q_l(x) &= \delta(x - x_l)
\end{aligned} \tag{5.12}$$

Assuming r_i 's are uniformly distributed in $(0, \theta]$, the second term inside double summation is easy to carry out.

$$E[\exp(jz)] = \begin{cases} 1 & i = l \\ \int_{-\theta}^{\theta} e^{jz} f(z) dz & i \neq l \end{cases}$$

where

$$z = k_w^m (r_i - r_l), \quad i, l = 1, 2, 3 \dots P \tag{5.13}$$

The random variable z is a function of two random variables, $k_w^m r_i$ and $k_w^m r_l$, which are independently and uniformly distributed in the interval of $(0, \theta]$. The probability density function of z is a convolution of density functions of $k_w^m r_i$ and $k_w^m r_l$ centered at 0, as shown in Figure 5.4. Performing integration, we have

$$E[\exp(jz)] = \begin{cases} 1 & i = l \\ \int_{-\theta}^{\theta} e^{jz} \left(\frac{1}{\theta^2} z + \frac{1}{\theta}\right) dz + \int_0^{\theta} e^{jz} \left(\frac{1}{\theta} - \frac{1}{\theta^2} z\right) dz = \frac{2}{j\theta^2} (\cos\theta - 1) & i \neq l \end{cases} \tag{5.14}$$

The independent uniform distribution for random variables $k_w^m r_i$ and $k_w^m r_l$ are first order approximations. Both phases are a result of matching phase for randomly selected waveguide locations at center wavelength λ_1 . Uniform distribution is reasonable since no preference is known. The value of θ is in the range of $(0, \Delta x)$. If the phase modulation introduces fast phase variation in the arrayed waveguides, there will be a large number of

zero crossings available along the interface of AW/OC. We may introduce certain selection rules in the algorithm for random points to control $_$, which may provide opportunities to reduce noise in the future. It is quite challenging to derive an analytical expression for the first expectation operation in Equation (5.12). As $t=0$, $R_ (0)=P$. As $t \neq 0$, the problem turns to a Random Poisson Points problem. Computation of $R_ (t)$ is carried out by Monte Carlo simulations as discussed below. Using different sampling rates, we can gain insight about the noise spectrum by such simulations.

Figures 5.5.a, 5.5.b, and 5.5.c show a Monte Carlo simulation of the autocorrelation function $R_ (t)$ and its Fourier transform $_ (f_x)$, which is the power spectral density function. In Figures 5.5.a, 5.5.b, and 5.5.c, we note that zero spatial shift for autocorrelation functions and zero spatial frequency for power spectral density functions are at the middle of the horizontal axis. The impulse at the center of the autocorrelation function, $R_ (0)$, is caused by the white noise behavior of the locations of x_i 's. As t increases or decreases, the number of possible terms inside the double summation in Equation (5.12) decreases, and goes to zero as the spatial shift reaches the entire length of $_ (x)$. As a result, autocorrelation is higher in the middle, and reduces to zero at the two ends. The power spectral density is plotted in dB scale. Considering Equation (5.8), we have

$$\begin{aligned}
 FT\{h(x)\} &= \sum_{m=1}^M \Phi \left(f_x - \frac{(m-1) \cdot \Delta\lambda \cdot \xi \cdot \alpha}{2\pi} - \frac{k_w^1 \alpha}{2\pi} \right) \cdot G(f_x) \\
 \Phi(f_x) &= FT\{\varphi(x)\} \\
 G(f_x) &= FT\{g(x)\}
 \end{aligned} \tag{5.15}$$

Therefore, the output of the ISZC AWG is a shifted version of $_ (f_x)$ scaled by the envelop of the Fourier transform for the Gaussian field mold profile at individual arrayed waveguides. $_ (f_x)$ is the square root of the power spectral density shown in Figures 5.5.a-5.5.c.

The -20dB noise around the center impulse is comparable with simulations performed in previous chapters for regular AWG's. The impulse is the result of the white noise behavior of the autocorrelation function. The interesting phenomenon is rise and fall of the noise spectrum. As sampling rate increases, more spectrum content is revealed.

This could be understood in regular spaced grating context. The spatial frequency in $_x$ power spectral density function is equivalently the physical coordinates of the receiving end of the output coupler. The harmonic peaks present in regular grating structure should fall as the harmonic order increases, i.e. physically further away from the fundamental order. The randomly spaced phase elements turn those harmonic peaks into noise around their original locations. As the power in higher harmonic peaks decrease for regular gratings, the noise around those peaks should reduce as well in irregularly sampled grating structures. This feature suits the demultiplexing purpose of the ISZC device. As the noise is further away from the original channel, the crosstalk to the far away channels would not increase. Therefore, increasing wavelength channels will not result in accumulating crosstalk noise in far away channels. The near by channels will be affected. Even though the -20dB noise floor is higher than the regular AWG device (-25dB) [55, 56]. It is still tolerable. High channel count ISZC AWG is a trade off between more wavelength channels and higher crosstalk. The crosstalk in wavelength scale is not accumulative, as long as the maximum crosstalk from individual wavelength channel is under a certain level. Simulating the ISZC AWG using Matlab, the crosstalk noise further investigated below and found to be shown comparable between different channel counts.

In order to have a more comprehensive understanding of the various effects different parameters have on the ISZC AWG noise level, extensive simulations are carried out using the scalar wave model developed in Chapter 3. These simulations are designed to investigate the relationship between the noise performance of an ISZC AWG and important device parameters over aperture size, number of arrayed waveguides and waveguide spacing.

The results are summarized in Figures 5.6a-5.6.c. Figure 5.6.a shows effects of constant AW count (200) with varying average waveguide spacing (i.e. the spacing of initial uniform grid). The results show the crosstalk margins stay relatively constant; average waveguide spacing (center to center), equivalently the overall-aperture-size ($\#AW _ \text{average spacing, OAS}$), determines the bandwidth of the wavelength channel. Figure 5.6.b summarizes results for constant average spacing with varying AW count. It shows reduction of crosstalk margins as number of AW increases, and channel bandwidth

decreases as the OAS increases. Figure 5.6.c shows the results for fixed OAS (3mm) with varying numbers of AW's, noting a different OAS (4.5mm) for 1024-ch case. Again it shows the decrease of crosstalk with increase of AW count, and channel bandwidth remains constant. In summary, the results indicate crosstalk decreases with increasing AW count for varying channel counts, thus crosstalk is unrelated to channel count. Another observation is that channel bandwidth is inversely correlated to the OAS as expected, since the couplers of AWG's are effectively a lens and OAS is the aperture of it.

Examples are shown in Figures 5.7.a-5.7.c for the results in Figures 5.6.a-5.6.c. Figure 5.7.a shows the output spectrum of a 1024-channel ISZC AWG. Figures 5.7.b and 5.7.c show a close up view for different AW count and OAS. The relationships between crosstalk/AW count and channel bandwidth/OAS are illustrated. Given 500 AW count, the crosstalk margin is reduced to -20dB. The larger than usual crosstalk is a trade off for large channel count (>500). Similar channel count would be achieved by more complex multi-stage cascaded systems.

5.2 Channel Capacity Consideration

The emanation of field from a single mode waveguide can be approximated as the TEM₀₀ Gaussian mode. The far field Fraunhofer diffraction can be found using the Rayleigh-Sommerfeld diffraction formula [23]. The observing point P₀ is in spherical coordinate, and the source point P₁ is in cylindrical coordinate as shown in Figure 5.8.

Starting with the Rayleigh-Sommerfeld diffraction formula, we have

$$E(P_0) = \frac{1}{j\lambda} \iint_s E(P_1) \frac{\exp(jkr_{01})}{r_{01}} \cos(\vec{n}, \vec{r}_{01}) ds \quad (5.16)$$

Using the above diagram, we can express r_{01} as

$$\begin{aligned} r_{01} &= \sqrt{(R \cos \Theta)^2 + r^2 + (R \sin \Theta)^2 + 2rR \sin \Theta \cos(\Phi - \phi)} \\ &= R \sqrt{1 + \frac{2r}{R} \sin \Theta \cos(\Phi - \phi) + \frac{r^2}{R^2}} \end{aligned} \quad (5.17)$$

In the 2-D case, we have

$$\begin{aligned}
r_{01} &= \sqrt{r^2 + R^2 + 2rR \sin \Theta} \\
&= R \sqrt{1 + \frac{2r}{R} \sin \Theta + \frac{r^2}{R^2}}
\end{aligned} \tag{5.18}$$

In the following, we work with a more general 3-D case. Since $R \gg r$, we have

$$r_{01} = R + r \sin \Theta \cos(\Phi - \phi) \tag{5.19}$$

Since $\cos(\vec{n}, \vec{r}_{01}) = \cos \Theta' \approx \cos \Theta$, the wave propagates forward in a narrow cone, the paraxial approximation gives $\cos \Theta \approx 1$. We can substitute r_{01} and further simplify the denominator while keeping r_{01} for the phase factor. We have,

$$E(R, \Theta, \Phi) = jk \frac{e^{jkR}}{2\pi R} \iint E(r, \phi, 0) e^{jkr \sin \Theta \cos(\Phi - \phi)} r dr d\phi \tag{5.20}$$

Since the emanating field is Gaussian, its field profile can be written as

$$E(r, \phi, 0) = E_0 e^{-r^2/w_0} \tag{5.21}$$

where w_0 is the waist size of the Gaussian beam. After integration, we have

$$E(R, \Phi, \Theta) = jkE_0 \frac{e^{jkR}}{R} \frac{w_0}{2} e^{-(kw_0 \sin \Theta)^2/4} \tag{5.22}$$

The effective width w_e of a Gaussian profile is given as

$$w_e = \frac{\int_0^\infty E^2(r) r dr}{E^2(0)} = w_0 \sqrt{\frac{\pi}{2}} \tag{5.23}$$

The relation between the effective width and physical width of a waveguide [33] is given as

$$w_e = \frac{w_{WG}}{2} \left(0.5 + \frac{1}{V - 0.6} \right) \tag{5.24}$$

where V is the normalized frequency. The curve in Equation (5.24) is found empirically through curve fitting [33]. For a single mode waveguide, let $2 < V < 4$; as a result, we can conclude $w_e \approx 0.5 w_{WG}$.

To calculate the width of the Gaussian profile at the output side of the coupler, we express the intensity profile as

$$I = I_0 e^{-2\theta^2/\theta_0^2} \tag{5.25}$$

Comparing to Equation (5.22), and setting $\sin \theta = \theta$, we have

$$I = I_0 e^{-\frac{(kw_0\Theta)^2}{2}} \quad (5.26)$$

Therefore the Gaussian profile width θ_0 can be found as

$$\Theta_0 = \frac{2}{kw_0} = \frac{\lambda}{\pi n_s w_0} = \frac{\lambda}{n_s w_e \sqrt{2\pi}} = \frac{\sqrt{2}\lambda}{n_s w_{WG} \sqrt{\pi}} \quad (5.27)$$

The channel bandwidth in wavelength can be found using Fraunhofer diffraction calculation. The channel bandwidth in wavelength is the main lobe of the image, which is determined by the overall aperture size, which is made up of the output ends of the arrayed waveguides at their interface with the output coupler as shown in Figures 5.9 and 5.10. Considering Figure 5.10, given the aperture size $D=N_{WG}W_{WG}$ and propagation distance R as shown in the diagram, the main lobe of the diffraction pattern, i.e. the bandwidth, is [23]

$$CW = \frac{\lambda R}{N_{WG} \cdot W_{WG}} \quad (5.28)$$

where CW is the channel bandwidth in wavelength, N_{WG} is the number of waveguides, W_{WG} is the width of waveguides, and R is the radius of the input arc of the coupler. So the maximum channel count (see Figure 5.9), disregarding the effect of FSR, can be found as

$$N_{chan}^{max} = \frac{\Theta_0 R}{\frac{\lambda R}{N_{WG} W_{WG}}} = \frac{\sqrt{2} N_{WG}}{n_s \sqrt{\pi}} \quad (5.29)$$

The ratio of the maximum channel count over the AW count can be used to compare the channel capacity of an ISZC AWG or a regular AWG device for given number of AW's. Defining channel capacity measure ρ as

$$\rho = \frac{N_{WG}}{N_{chan}^{max}} = \frac{n_s \sqrt{\pi}}{\sqrt{2}} \quad (5.30)$$

Taking $n_s=1.45$, we have $\rho=1.8$ in Equation (5.30), while in literature, the ratio have reported for high channel count AWG's are greater than 3 [55, 56]. We note this derivation does not necessary give the upper bound of ρ for ISZC AWG.

5.3 Conclusions

In this chapter the origin of noise is considered, and channel capacity of an ISZC AWG is derived. The output noise of ISZC is mainly due to the modulation of spherical wave in the arrayed waveguide section. The noise spectrum generated by each channel falls away from its pass band. This makes the accumulative crosstalk for each wavelength channel tolerable. This is due to the implementation of irregular sampling. The adjacent channel noise floor does increase since the irregular placement of the AW apertures on the IC/AW and AW/OC interfaces turns harmonic power to background noise. The maximum channel capacity for given AW's for ISZC AWG is derived using diffraction theory and waveguide analysis, and the ratio of the AW count over the maximum channel count shows improvement for an ISZC AWG in accommodating more channels for given number of AW's over a regular AWG.

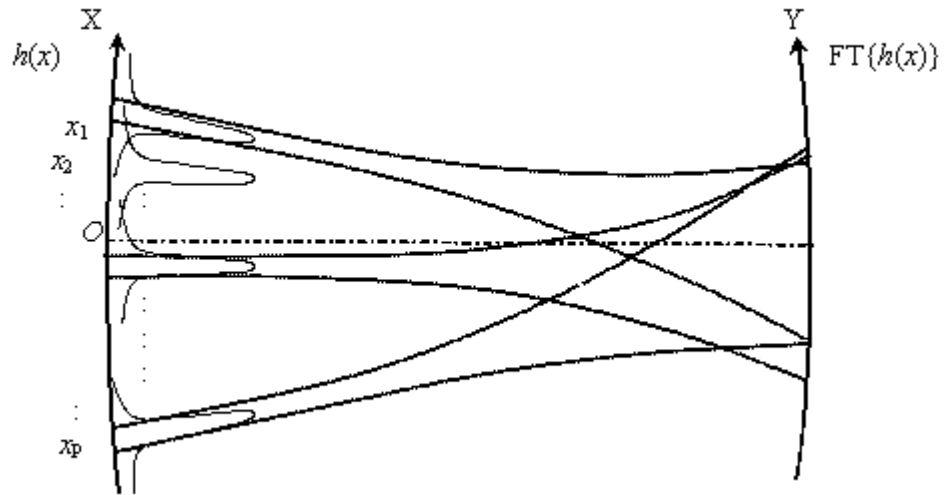


Figure 5.1. Output coupler input-output diagram.

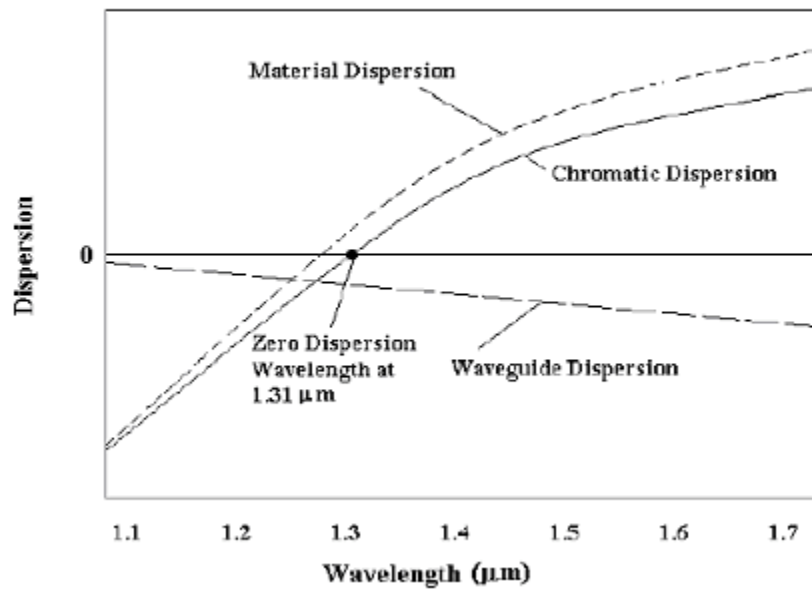


Figure 5.2. Dispersion in single-mode optical fiber as a function of wavelength.

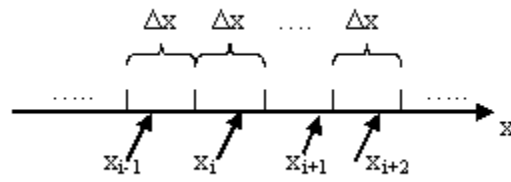


Figure 5.3. Random locations of x_i 's on the x -axis

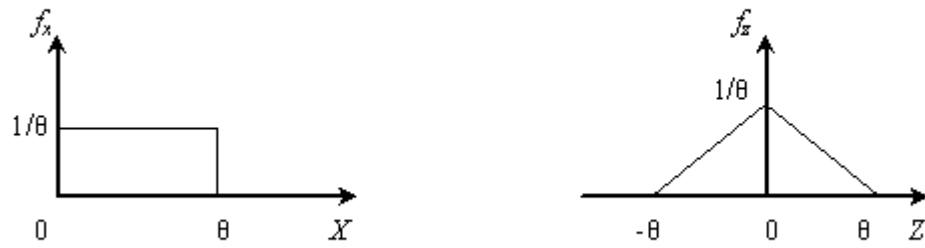


Figure 5.4. Probability function of z ($z = k_w^m (r_i - r_j)$).

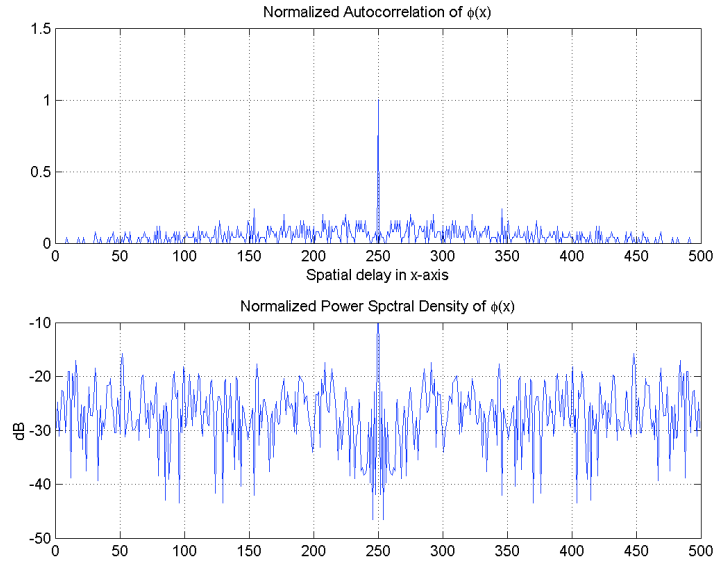


Figure 5.5.a. Noise Spectrum with 500 points, $x=20$ m.

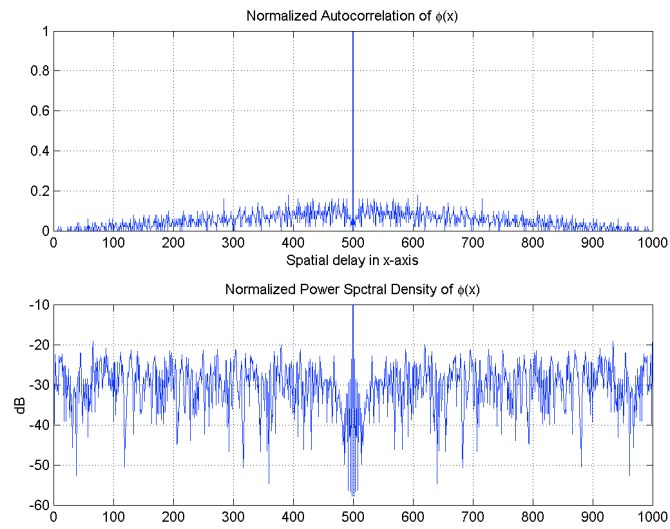


Figure 5.5.b. Noise Spectrum with 1000 points, $x=4$ m.

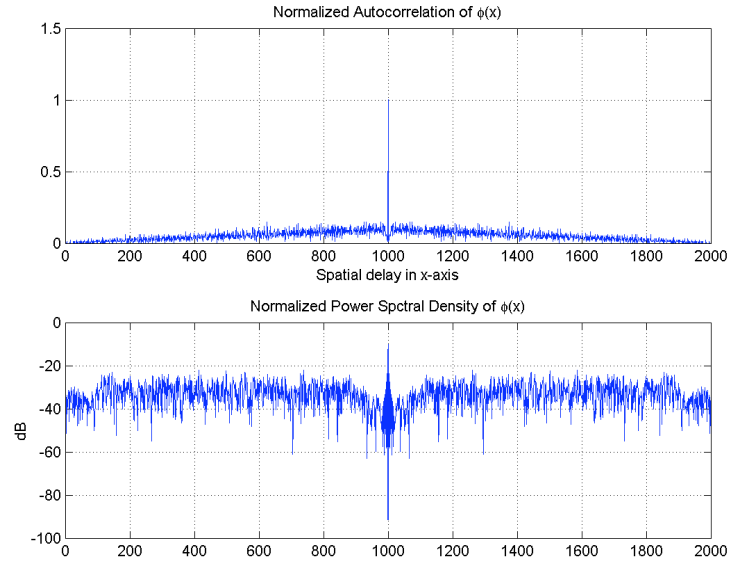


Figure 5.5.c. Noise Spectrum with 2000 points, $x=4$ μ m.

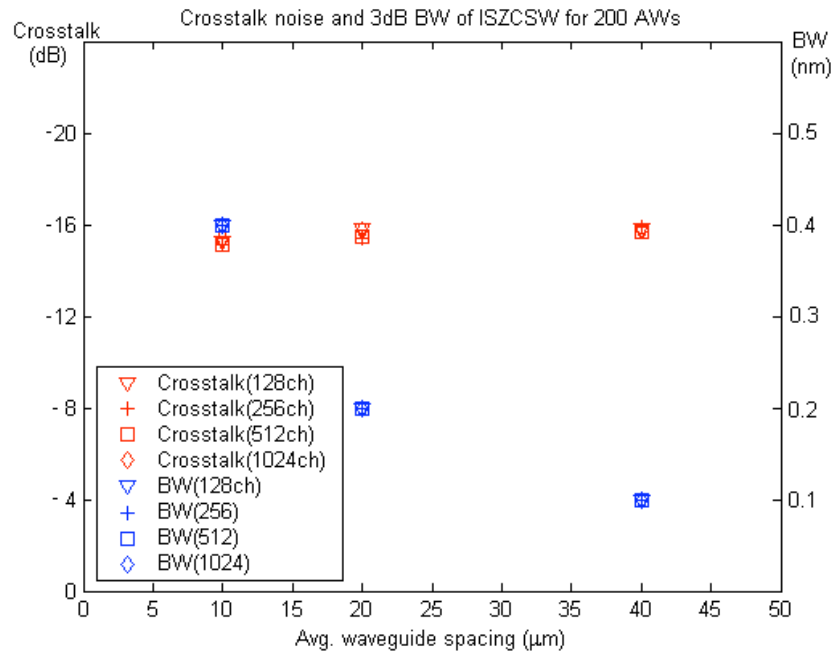


Figure 5.6.a. Crosstalk noise and wavelength channel width of ISZCSW AWG's for fixed number of waveguides ($M=200$).

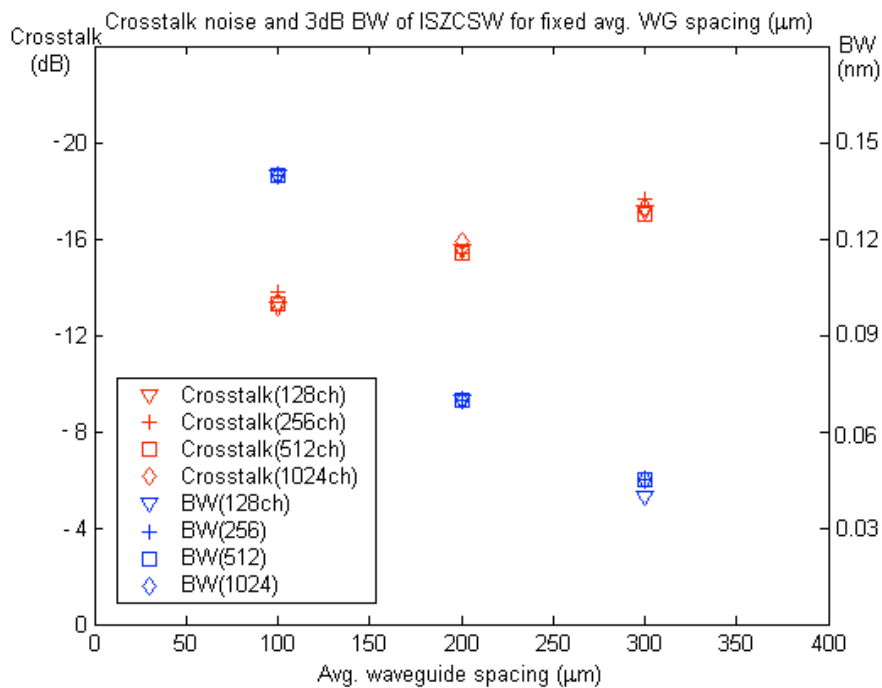


Figure 5.6.b. Crosstalk noise and wavelength channel width of ISZCSW AWG's for fixed average waveguide spacing (15 μm).

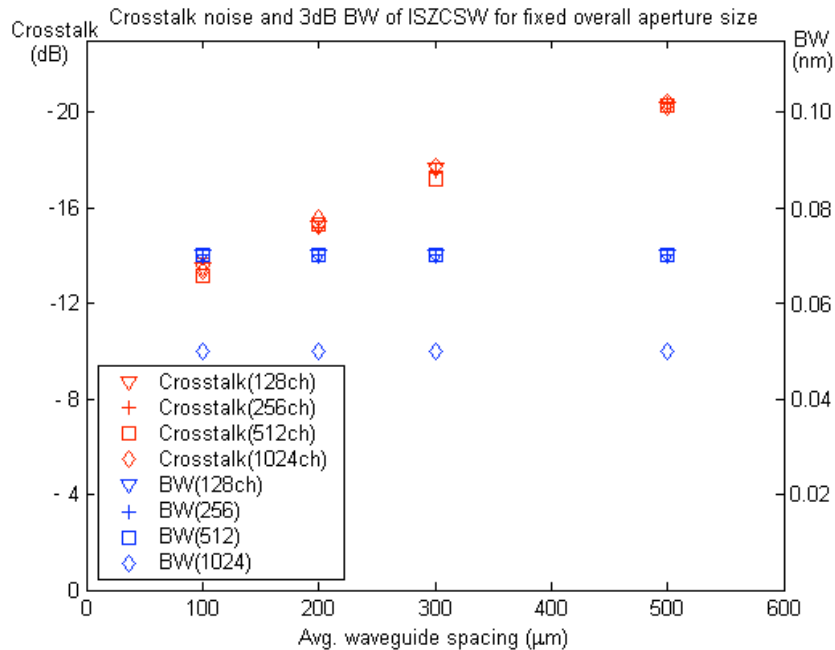


Figure 5.6.c. Crosstalk noise and bandwidth of wavelength channel for ISZCSW AWG's with fixed total aperture size 3mm (the total length covered by the arrayed waveguides on the interface to couplers).

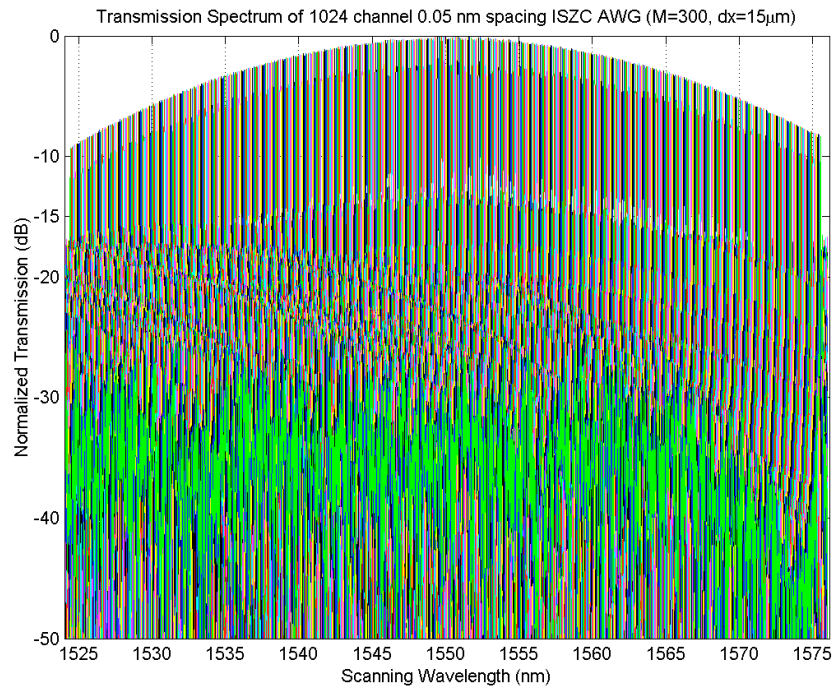


Figure 5.7.a. 1024-Channel ISZC AWG with 300 waveguides, overall aperture 4.5mm

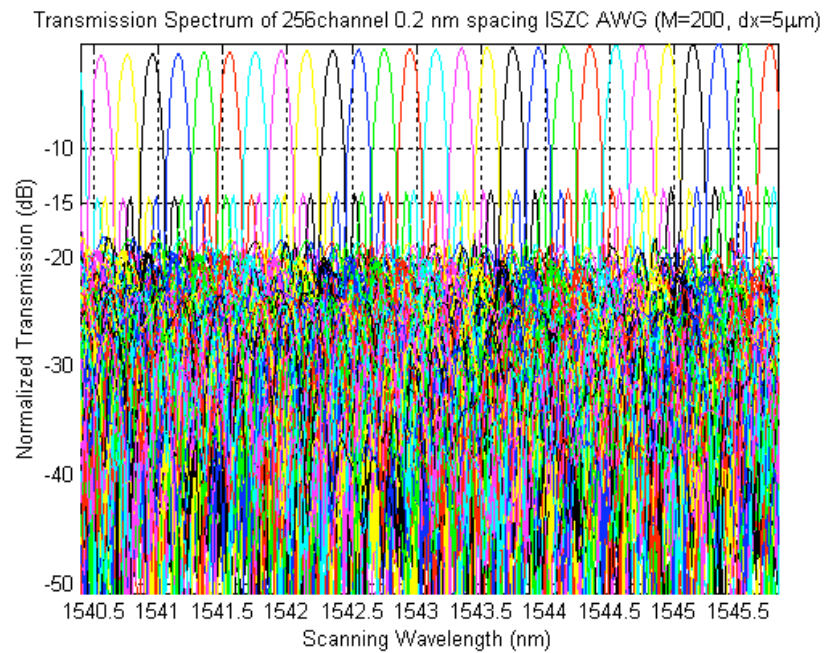


Figure 5.7.b. 256-Channel ISZC AWG with 200 waveguides, overall aperture size 1mm.

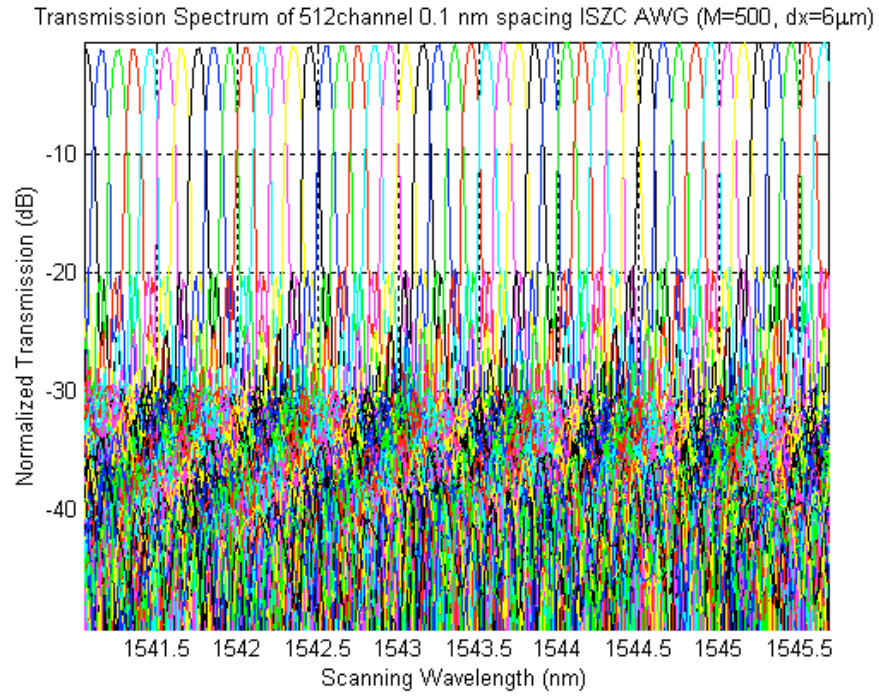


Figure 5.7.c. 512-Channel ISZC AWG with 500 waveguides, overall aperture size 3mm.

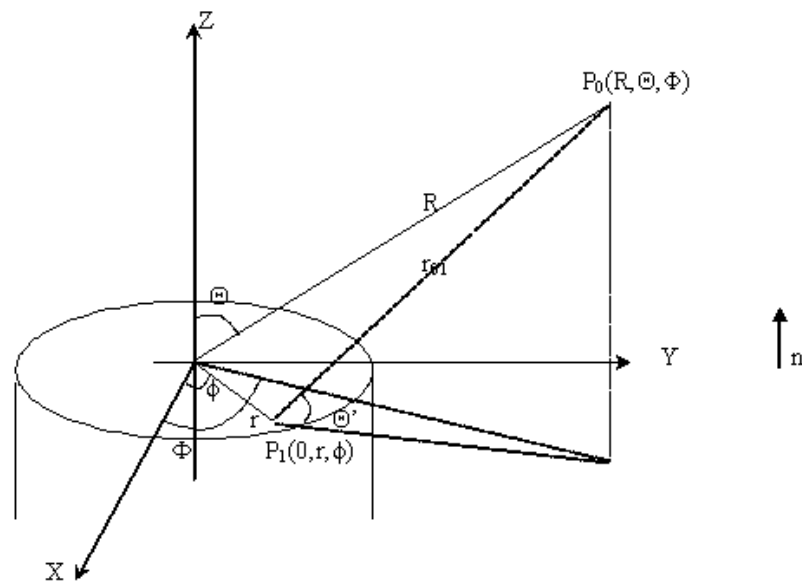


Figure 5.8. The coordinate systems for Gaussian beam diffraction process

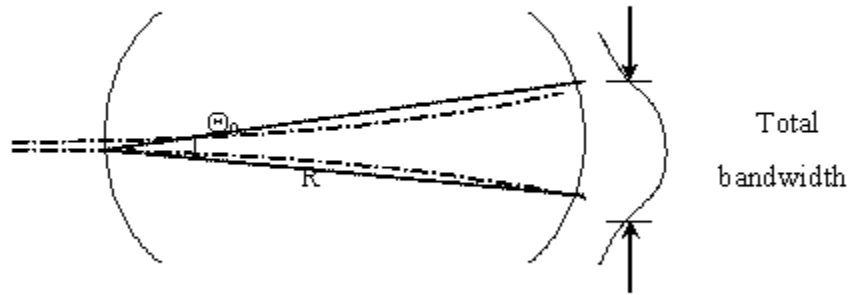


Figure 5.9. The overall Gaussian intensity profile at the coupler output.

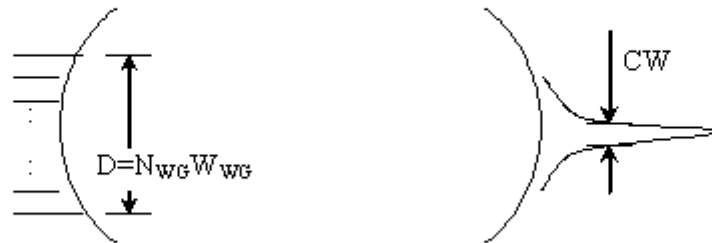


Figure 5.10. The line width of individual wavelength channels.

6. CONCLUSIONS AND FUTURE RESEARCH

6.1 The Need for Large Channel Count Wavelength Demultiplexers

As the internet and wireless based communications reach deeper into society, the telecommunication industry becomes more driven by consumer needs. These needs vary widely from low bandwidth applications of simple email or pager messages to intensely bandwidth demanding applications such as downloading movies on Internet, live video stream for high definition Internet broadcasting and so on. This and similar environments put pressure on the new generation of networks that are able to use available bandwidth efficiently. Dense Wavelength Division Multiplexing (DWDM) techniques can provide wavelength channels that are blind to data rates of different Time Division Multiplexing (TDM) formats. Nowadays data is routinely sent at 2.5Gbps (OC-48); more recently 10Gbps (OC-192) has become increasingly available, and current goal is to achieve 40Gbps (OC-768). Yet the cost and maintenance of new equipment is high. The approach of DWDM is to provide large number of smaller bandwidth channels; this may prove to be more economical. 0.4nm (25GHz) or even lower wavelength spacing (1GHz) are proposed [56]. This will provide DWDM extremely large number of wavelength channels (~500) even when only the C band (1530-1570nm) is considered. Multiplexing and demultiplexing such large number of wavelength channels would mostly accomplished by cascaded AWG devices. However, to avoid insertion loss occurring in multistage wavelength multiplexing and demultiplexing, large channel count AWG devices with tolerable insertion loss will be in urgent demand. Due to the limited number of waveguides to be fabricated on the semiconductor substrate, the FSR can not be made as wide as desired. We propose the MISZC method to be an attractive option.

As we have shown earlier, the number of maximum channel count is proportional to the number of waveguides available on the semiconductor substrate, $N_{ch} = N_{WG} / \rho$. ρ varies from 3~4 for regular AWG's, and is found to be 1.8 for ISZC AWG's using diffraction and waveguide analysis in the previous chapter. However, this is not an upper

bound. There is potential to further improve channel count. Lenses can also be incorporated to make wavelength channel width much smaller. Therefore, the fundamental limitation with regular AWG is its FSR.

6.2 Research Summary

The method of ISZC is based on the combined techniques of irregularly sampled phase array and zero crossing sampling. This approach is novel in the sense of its application in AWG design resulting in the removal of FSR of a regular AWG. Due to the coupling between the input wavefront and the physical shape of the input coupler, the input wavefront is coupled into the arrayed waveguide approximately as a plane wave. In the case of regular AWG, in order to provide linear dispersion and refocus the input image at the center of the receiving end of output coupler, the arrayed waveguide section has to generate $2m\pi$ phase shifts in successive arrayed waveguides at center frequency, which forces uniform spacing of the arrayed waveguides and constant waveguide length increment. As waves enter the output coupler, a spatial Fourier transform relation is formed by the output coupler geometry between the input and output fields. So at the end, repetitive diffraction orders appear at the output of the output coupler. This limits the number of maximum possible wavelength channels.

The zero crossing and the irregular phased array are the two underlying techniques used in ISZC AWG design. The zero crossing technique alters the lengths of arrayed waveguides in such a way as both to provide linear dispersion, and to simultaneously modulate the plane wave with a fast varying phasefront in the waveguide section. This enables the abundant zero crossing phase matching along all possible locations for placing the arrayed waveguides. This design enables the arrayed waveguides to be placed at semi-random locations to eliminate grating harmonics. Harmonics due to nonlinear encoding of phase is also eliminated due to special geometry provided by the spherical reference wave. Through simulation and theoretical analysis, we have shown ISZC is a viable approach to optical wavelength demultiplexing. ISZC AWG trades more wavelength channel for higher but tolerable noise. Noise is caused by harmonic images turning into noise. For the irregular phased array, given the fixed array of phase elements

placed on a circular arc, each emanating fields toward the center of the circle, for both regular and irregular placed arrays, a constructive interference pattern is formed at center of the arc. The power delivered to this focus is the same for both cases. If the elements are placed regularly, harmonics will appear, whereas for irregularly spaced elements the harmonic power is changed to background noise.

In Chapter 1, we set the context for the development of large channel count wavelength demultiplexers; it is one of the enabling technology in future optical networks. In Chapter 2, the description of MISZC is provided, and its capacity of wavelength demultiplexing and elimination of higher harmonic orders are derived. In Chapter 3, a scalar wave model of AWG device is described; day to day simulations of ISZC AWG design can be carried out using this model due to its speed and accuracy. The model and simulation results are tested satisfactorily against accepted AWG governing equations [32]. In Chapter 4, we describe implementation issues of ISZC AWG on BeamPROP optical design software. BeamPROP has features designed exclusively for regular AWG's. We discuss in depth ways to incorporate ISZC by altering layout generation codes provided Rsoft. The simulation results using BeamPROP are shown; the goal of eliminating FSR is clearly demonstrated. The elimination of FSR is at the cost of increased noise. In Chapter 5, we analyze issues of noise and channel capacity for ISZC AWG's. Using spatial Fourier transform framework, we show the properties of wavelength demultiplexing and describe noise in a compact form. More simulations are carried out to investigate the noise under high channel count conditions. It is shown the noise level is higher because of the increased noise in immediate vicinity of each wavelength channel. With limited crosstalk in far away channels, the noise increase is tolerable. Simulations also reveal influence of ISZC AWG parameter on the noise level.

A rigorous analysis of ISZC AWG is challenging because of the nonlinear manner the zero crossings are located and the random way the initial waveguide location is chosen. Due to the nonlinear nature of the zero crossings and irregular sampling, stochastic tools should be applied for further analysis of noise.

6.3 Future Research

For future research in ISZC AWG, the following issues that may provide opportunities for performance improvement and deeper understanding of noise in ISZC AWG design.

1. Optimization of zero crossings. The abundance of zero crossings should provide some ground for optimization. Based on stochastic analysis of noise, certain rules can be applied in the algorithm in selecting the zero crossings so that the overall noise level could be reduced.

2. Asymmetric layout of the arrayed waveguides. The placements of the arrayed waveguides on the interfaces with the input and output couplers are identical in the ISZC design that we discuss in this thesis. It is necessary to place the arrayed waveguides irregularly at their interface with the output coupler, but such placement is not necessary at their interface with the input coupler. The result of such design at the interface of the arrayed waveguides and the input coupler is the reduced coupling of the input wavefront. In regular AWG design, the tapered waveguides provide better coupling of input wavefront. Therefore, at the input coupler interface the arrayed waveguides can be spaced regularly. And irregular spacing is enforced at the output coupler interface with the arrayed waveguide.

3. Analysis of noise in depth. The noise formulation in autocorrelation in Chapter 5 Equation (11) could be turned to a random point problem in calculation of expected value. The probability of two randomly distributed points over the same line segment is dealt with by the classical Poisson random points problem. Then, their joint probability density function can be found once their probability function is known, and be used in computing the expectation value. The result may provide ways to understand the noise issue better.

4. Improve fault tolerance for regular AWG. Better understanding of ISZC AWG may help to better control noise in regular AWG design as phase error due to defects is unavoidable as in manufacturing process.

5. Fabricate the device on chip and characterize it. Empirical studies should help establish the theory on a firm foundation. BeamPROP has features to produce masks of

finished design. The fabrication of ISZC AWG should be a significant milestone in its development.

In conclusion, ISZC AWG design is a novel approach to wavelength demultiplexing design. It provides much expanded bandwidth for wavelength demultiplexers. Theoretical development and simulations have confirmed the capacity of ISZC AWG design method. The cost of eliminating FSR in regular AWG is higher noise floor is higher for ISZC AWG compared to regular AWG. As the further research is conducted, the noise may be better understood and controlled to improve the overall performance of the ISZC AWG.

REFERENCES

- [1]. T. Ono, Y. Yano, "Key technologies for terabits/second WDM systems with high spectral efficiency of over 1 bit/s/Hz", *IEEE J. of Quantum Electronics*, vol. 34, no. 11, Nov. 1998, pp. 2080-2088; (NEC)
- [2]. Y. Miymoto, K. Yonenagaet, A. Hirano, N. Shimizu, M. Yoneyama, H. Takara, K. Noguchi, K. Tsuzuki, "1.04-Tbit/s DWDM transmission experiment based on alternate-polarization 80-Gbit/s OTDM signals", 24th European Conference on Optical Communication, ECOC '98, Telefonica. Part vol.3, 1998, pp.53-7 vol.3. Madrid, Spain; (NTT)
- [3]. C. Chen, R. Sahara, R. Ranganathan, J. Dormail, R. Patterson, J. Coyne, S. Burroughs, H. Lu, "1.4-Tb/s (35 ch*40 Gb/s) WDM transmission experiment over 85 km standard single-mode fiber", 998 International Conference on Communication Technology Proceedings. Beijing, China. China Inst Commun. (CIC). Chinese Inst. Electron. (CIE). IEEE Commun. Soc. (IEEE COMSOC). 22-24 Oct. 1998; (Lucent)
- [4]. Lucent website, <http://www.lucent.com/press/1199/991110.bla.html>;
- [5]. Stocks L. F., "Optical-fiber filters for wavelength division multiplexing," *IEEE Circuits & Devices Magazine*, Vol.12, no.5, pp 49-50, Sept. 1996.
- [6]. S. Jin, H. Mavoori, J. Fricke, M. Matalla, K. Paschke, R. Guther, A. Knauer, F. Bugge, H. Wenzel, G. Erbert, "Magnetically Tunable Fiber Bragg Gratings," *Optical Fiber Communication Conference (OFC '99) Technical Digest*, San Diego, CA, Feb 21-26, 1999, paper THJ2;
- [7]. Giles C. R., "Lightwave Applications of Fiber Bragg Gratings," *IEEE J. Lightwave Technol.* Vol. 15, no 8, Aug. 1997, pp 1391-1404;
- [8]. Ersoy O. K. "One-image-only digital holography," *Optik*, vol. 53, no. 1, pp 47-62, 1979;
- [9]. Ersoy O. K. "Virtual holography: a method of source and channel encoding and decoding of information," *Appl. Opt.*, vol 18, pp2543, Aug 1979;

- [10]. Ersoy O. K. "Construction of point images with the scanning electron microscope: a simple algorithm," *Optik*, vol. 53, no. 1, pp 47-62, 1979;
- [11]. Smit M. K., "New focusing and dispersive planar component based on optical phased array," *Electronics Letters*, vol.24, no.7, 31 March 1988, pp.385-6.
- [12]. Dragone C., Edwards C.A., and Kistler R. C., "Integrated Optics N×N Multiplexer on Silicon," *IEEE Photonics Technology Letters*, vol.3, no.10, Oct. 1991, pp.896-9.
- [13]. Dragone C., "An N×N optical multiplexer using a planar arrangement of two star couplers" *IEEE Photon. Technol. Lett.*, pp 812-815, Sep 1991;
- [14]. Takahashi H. and et al, "Arrayed-waveguide grating for wavelength division multi/demultiplexer with nanometer resolution," *Electron. Lett.*, vol. 26, pp 87-88, 1990;
- [15]. Sarathy J, et al., "Polarization Insensitive Waveguide Grating Routers in InP," *IEEE Photonics Technol. Lett.* Vol. 10, no 12, Dec 1998, pp1763-1765;
- [16]. Takada K. Yamada H. Okamoto K, "480 channel 10GHz spaced multi/demultiplexer," *Electronics Letters*, Vol. 35 no. 22, Oct 1999, pp 1964-1966;
- [17]. Takada K. Okamoto K, "Multi/demultiplexer consisting of one parent 10GHz-spaced AWG and eight subsidiary 100GHz-spaced AWGs," *Electronics Letters*, Vol. 35 no. 16, Aug 1999, pp 1334-1935;
- [18]. H. Bissur, B. Martin, R. Mestric, and F. Gaborit, "Small-size polarization-independent phased array demultiplexers on InP," *Electron. Lett.*, Vol. 31, no. 24, pp 2118-2120, 1995;
- [19]. M. Kohtoku, H. Sanjoh, S. Oku, et al, "InP-based 64-channel arrayed waveguide grating with 50GHz channel spacing and up to -20 dB crosstalk," *Electron. Lett.*, vol. 33, no. 21, pp 1786-1787, 1997;
- [20]. J. B. D. Soole, et al, "Polarization-independent InP arrayed waveguide filter using square cross-section waveguides," *Electron. Lett.*, vol. 32, no. 4, pp 323-324, 1996.
- [21]. D. Gabor, "A New Microscope Principle," *Nature*, Vol. 161, pp 777, 1948.
- [22]. E. N. Leith and J. Upatnieks, "Wavefront Reconstruction and Communication Theory," *J. Opt. Soc. Am.* Vol. 52, pp 1123, 1962.
- [23]. J. W. Goodman, "Introduction to Fourier Optics," *McGraw Hill*, New York, 2nd edition, pp353, 1996.

- [24]. A. W. Lohman and D.P. Paris, "Binary Fraunhofer Holograms Generated by Computer," *Appl. Opt.*, vol. 6, 1739-1748, 1967.
- [25]. W. H. Lee, "Sampled Fourier Transform Hologram Generated by Computer," *Appl. Opt.*, vol. 9, pp 639-643, 1970;
- [26]. A. Ishimaru, "Theory of Unequally-Spaced Arrays," *IRE Trans. On Antennas And Propagation*, pp 691-702, Nov. 1962.
- [27]. B. Steinberg, "Comparison between the Peak Sidelobe of the Random Array and Algorithmically Designed Aperiodic Array," *IEEE Trans. on Antennas and Propagation*, pp 366-369, May 1973.
- [28]. A. Goffer, M. Kam, P. Herczfeld, "Design of Phased Arrays in Terms of Random Subarrays," *IEEE Trans. on Antennas and Propagation*, vol. 42, no. 6, pp 820-826, June 1994,
- [29]. Y. T. Lo, R. J. Simcoe, "An Experiment on Antenna Arrays with Randomly Spaced Elements," *IEEE Trans. on Antennas and Propagation*, pp 231-235, Mar. 1967.
- [30]. G. Lockwood, P. Li, M. O'Donnell, and F. S. Foster, "Optimizing the Radiation Pattern of Sparse Periodic Linear Arrays," *IEEE Trans. on Ultrasonics, Ferroelectrics, and Frequency control*, vol. 43, no. 1, pp 7-14, Jan. 1996.
- [31]. Y. T. Lo, "A Mathematical Theory of Antenna Arrays with Random Spaced Elements," *IEEE Trans. on Antennas and Propagation*, pp 257-268, May 1963.
- [32]. Okamoto K., "Recent progress of integrated optics planar lightwave circuits," *Optical & Quantum Electronics*, Vol.31, No.2, pp. 107-29, Feb. 1999.
- [33]. Meint K. Smit and Cor van Dam, "PHASAR-Based WDM-Devices: Principles, Design and Applications," *IEEE J. of Select. Topics in Quant. Electronics*. Vol. 2. No. 2, pp 236-250, June 1996.
- [34]. C. Dragone, "Efficiency of a Periodic Array with Nearly Ideal Element Pattern," *IEEE Photonics Tech. Lett.*, Vol. 1, No. 8, pp 238-240, August 1989.
- [35]. C. Dragone, "Efficient N X N Star Couplers Using Fourier Optics," *J. Lightwave Tech.* Vol. 7, No. 3, pp 479-489, March 1989.
- [36]. C. R. Doerr and C. Dragone, "Proposed Optical Cross Connect Using a Planar Arrangement of Beam Steerers," *IEEE Photonics Tech. Lett.* Vol. 11, No. 2, pp 179-199, Feb. 1999.

- [37]. C. Dragon, "Efficient Techniques for Widening the Passband of a Wavelength Router," *J. Lightwave Tech.* Vol. 16, No. 10, pp 1895-1906, October 1998.
- [38]. A. Kaneko, R. Goh, H. Yamada, T. Tanaka, and I. Ogawa, "Design and application of silica-based planar lightwave circuits," *IEEE J. Selected Topics in Quant. Elec.* Vol. 5, No. 5, Sep. 1999.
- [39]. P. Munoz, D. Pastor, and J. Capmany, "Modeling and Design of Arrayed Waveguide Gratings," *J. Lightwave Tech.*, Vol. 20, No. 4, pp 661-674, April 2002.
- [40]. Joseph T. Verdeyen, "Laser Electronics," Prentice Hall, 1992.
- [41]. H. G. Unger, "Planar Optical Waveguides and Fibers," Oxford, U. K., Clarendon Press, Oxford Engineering Science Series, 1997.
- [42]. M. C. Hutley, "Diffraction gratings," Academic Press, 1982.
- [43]. Y. P. Ho, H. Li, and Y. J. Chen, "Flat channel-passband-wavelength Multiplexing and demultiplexing devices by multiple-rowland-circle design," *IEEE Photonics Tech. Lett.* Vol. 9, No. 3, pp 342-344, March 1997.
- [44]. Kerstin Worhoff, Palul V. Lambeck, and Alfred Driessen, "Design, tolerance analysis, and Fabrication of Silicon Oxynitride Based Planar Optical Waveguides for communication devices," *IEEE J. Lightwave Technol.*, Vol. 17, No. 8. pp 1401-1407, Aug. 1999;
- [45]. *BeamPROP™* AWG Utility Version 2.1, RSoft, Inc. 2001.
- [46]. D. Yevick and B. Hermansson, "A split-step finite difference analysis of rib waveguides," *Electron. Lett.*, Vol. 25, pp. 461-462; 1989.
- [47]. D. Yevick and B. Hermansson, "Efficient beam propagation techniques," *IEEE J. of Quantum Electron.*, Vol. 26, No. 1, Jan. 1990.
- [48]. M. D. Feit and J. A. Fleck, "Light propagation in graded-index optical fibers," *Appl. Opt.*, Vol. 17, No. 24, pp. 3990-3998, Dec. 1978.
- [49]. D. Yevick, "A guide to electric field propagation technique for guided-wave optics," *Opt. Quantum Electron.*, Vol. 26, pp. 185-197, 1994;
- [50]. W. Huang, C. Xu, S. Chu, and S. Chaudhuri, "The finite-difference vector beam propagation method: analysis and assessment," *IEEE J. Lightwave Technol.*, Vol. 10, No. 3, pp. 295-305, Mar. 1992.

- [51]. R. Scarmozzino and R. M. Osgood, "Comparison of finite-difference and Fourier-transform solutions of the parabolic wave equation with emphasis on integrated-optics applications," *J. Opt. Am. A*, Vol. 8, No. 5, pp. 724-731, May 1991.
- [52]. G. R. Hadley, "Transparent boundary condition for the beam propagation method" *IEEE J. Quantum Electron.*, Vol. 28, No. 1, pp. 363-370, Jan. 1992.
- [53]. G. R. Hadley, "Wide-angle beam propagation using Padé approximant operators," *Opt. Lett.*, Vol. 17, No. 20, pp. 1426-1428, Oct. 1992.
- [54]. R. Clauberg and P. Von Allmen, "Vectorial beam propagation method for integrated optics," *Electron. Lett.*, Vol. 27, pp654, 1991.
- [55]. M. Kohtoku, et al. "InP-based 64-channel arrayed waveguide grating with 50 GHz channel spacing and up to -20dB crosstalk," *Electron. Lett.*, Vol. 33, no. 21, pp 1786-1787 October 1997.
- [56]. K. Takada, et al. "1-GHz-Spaced 16-Channel arrayed-waveguide grating for a wavelength reference standard in DWDM network systems," *IEEE J. Lightwave Technol.*, Vol. 20, pp 822-825, May 2002.
- [57]. H. Tsuda, H. Takenouchi, A. Hirano, T. Kurokawa, and K. Okamoto, "Performance analysis of a dispersion compensator using array-waveguide gratings," *IEEE J. Lightwave Technol.*, Vol. 18, pp 1139-1147, August 2000.

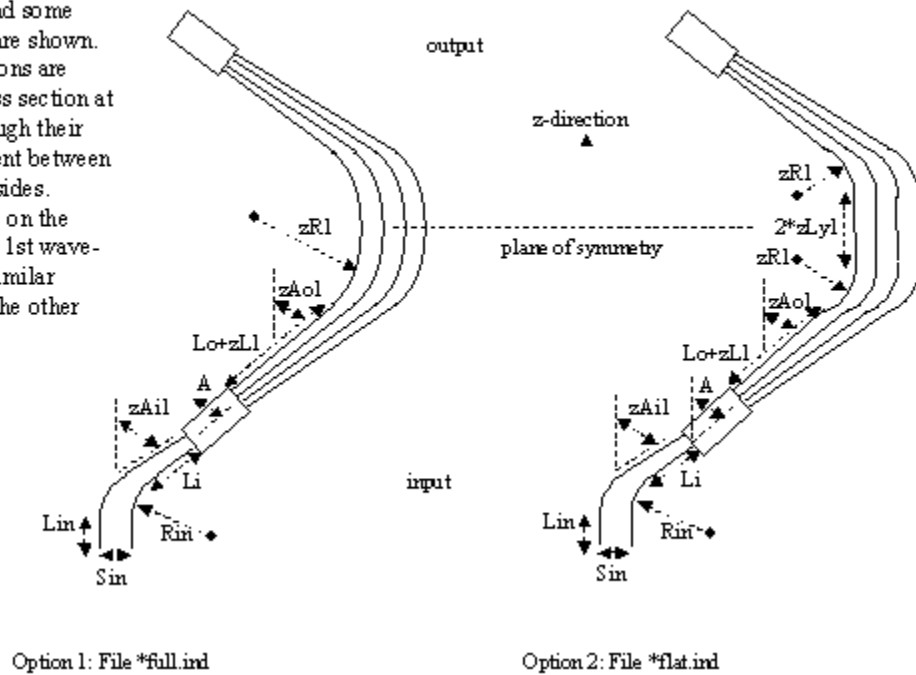
APPENDIX

An Example of an ISZC AWG Layout

An example of an ISZC AWG layout is presented with data on its physical dimensions. An ISZC AWG is based on modification of a regular AWG. In Figure A.1, two layout schemes of regular AWG's are shown. We used the full layout.

Arrayed Waveguides

Two constraint options are generated when the layout is specified. Design, and some internal, parameters are shown. Parameter specifications are symmetric about cross section at the z midpoint, although their values may be different between the input and output sides. Parameters with a '1' on the end apply to only the 1st waveguide in the array. Similar parameters exist for the other waveguides as well.



. Figure A.1. Layout options for AWG design [45].

Important constants are defined as following

A	central angle of star couplers with respect to z axis
Rin/Rout	radius of input/output waveguide bends (5000_m)
Rz	minimum radius of arrayed waveguide bends (5000_m)
Lg	length along z of arrayed waveguide structure
Lextra	additional length added to Lg (Lextra=0)
Lin/Lout	straight length of input/output waveguides (100_m)
Sin/Sout	lateral separation if input/output waveguides (23_m)

The constraint equations (4.10, 4.11) and waveguide length equation (A.1) for the full option (see Figures A.2 and A.3) are given as

$$zLi + (zAai * zRi) - (A0 * Rz) = (i-1) * dL/2 \quad (4.10)$$

$$zRi * \sin(zAai) + (Rend + zLi) * \cos(zAai) = Rz * \sin(A0) + Rend * \cos(A0) \quad (4.11)$$

$$Li = 2 * (Lo + zLi + zRi * zAai) \quad (A.1)$$

The parameters for the constraint equations are defined as

Lot	the length of out put taper (500_m)
Ro	the radius of confocal arc's for the IC/OC
zAai	the radial angle of the ith waveguide from the z-axis in degrees
zLi	the variable waveguide stretch generating zero crossings
zRi	the radius of the curvature used to control placement of waveguides
Lo	a constant used to satisfy layout constrains (1000_m)
Lom	internal geometry parameter (14.24_m)
Li	total length of the ith AW.

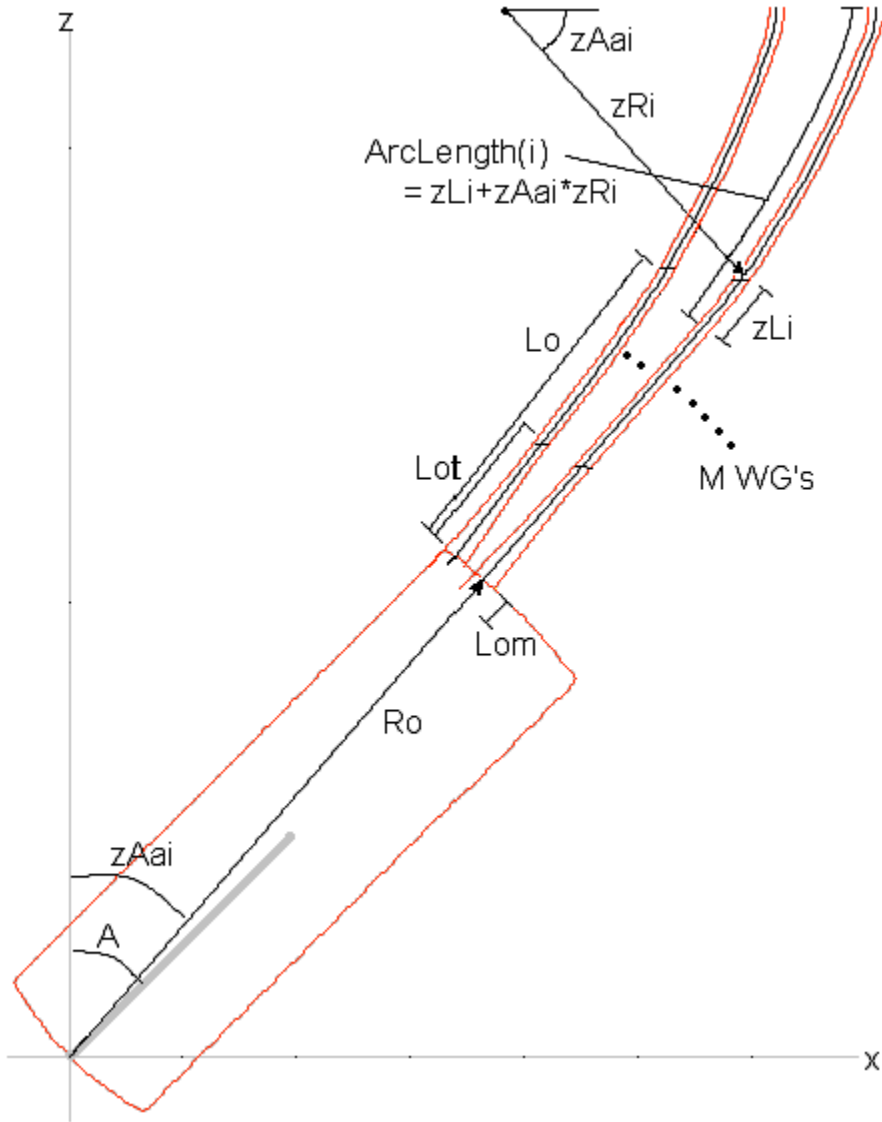


Figure A.2. Length constraint of array design for Full Layout [45].

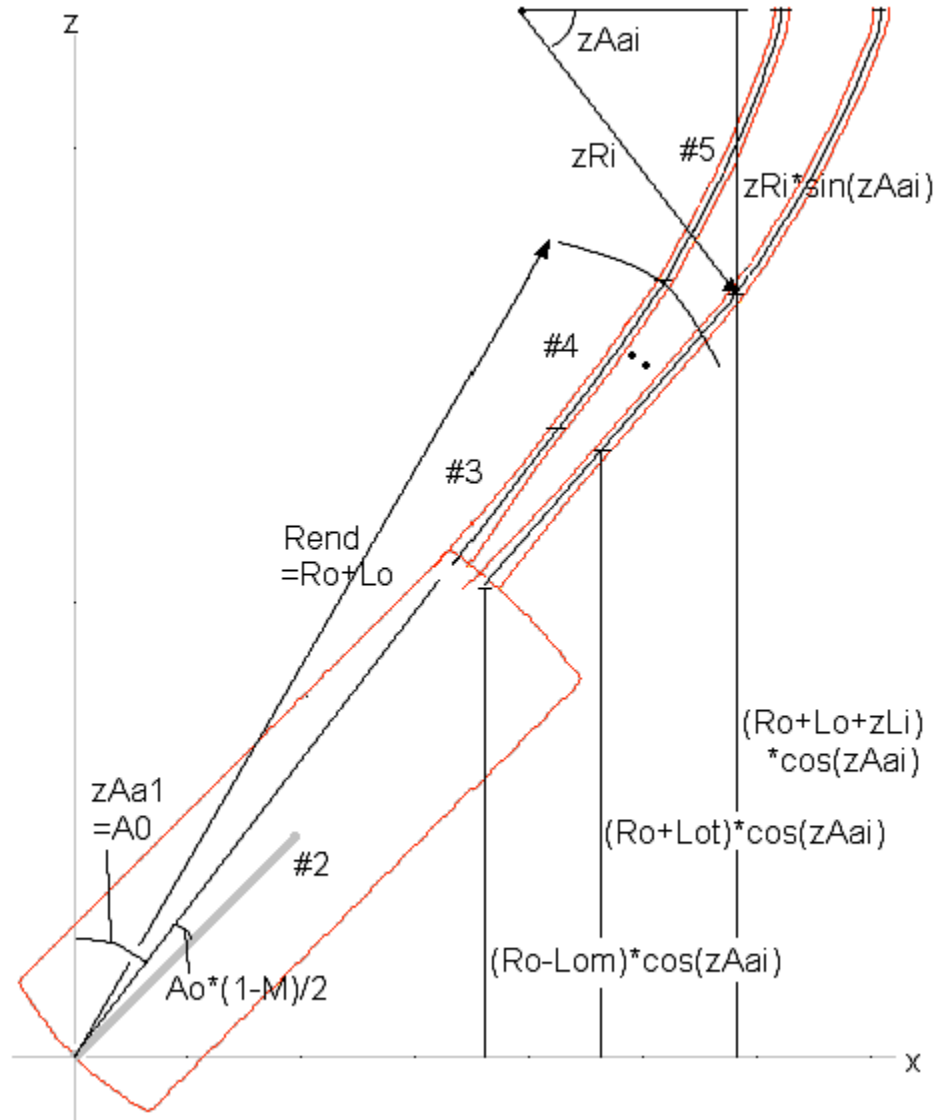


Figure A.3. Vertical constraint of array design for Full Layout [45].

For the full layout scheme, the index of the AW's starts from 0. The layout data for a 200-AW-128ch ISZC AWG is given as, $zAa0=A0=45$, $zR0=Rz=5000_m$, $dL=18.5_m$, $Ro=61802.75862_m$, $Rend=Ro+Lo=62802.75862_m$, $n_c=1.451293777$, $n_s=1.4532$. The rest of the data is listed below from 0-199 in columns, where Li , and zRi are in $_m$ and $zAai$ is in degrees.

Li

200304.67637418	201201.81166865	202065.83325126
200340.98370957	201210.35920841	202118.16577509
200368.75073406	201247.73164711	202127.77916527
200408.26860998	201279.78173531	202179.05009183
200427.50285557	201324.63529300	202191.86500098
200449.93941454	201329.96966417	202236.71790583
200502.26982777	201375.90113627	202263.42158966
200525.76524655	201410.07748342	202295.46294562
200540.70387198	201433.57756660	202321.09511784
200584.50164093	201458.13338310	202343.52113544
200625.08439391	201510.47287097	202379.83587172
200644.31372799	201543.57786663	202418.28028944
200683.81954014	201572.41762598	202437.50667549
200705.17484587	201586.29449078	202467.40956645
200742.57095020	201625.82056721	202510.13142479
200781.00549091	201652.51901195	202534.69853758
200792.76424198	201672.80839067	202560.33202211
200831.21043150	201705.91236733	202603.05237596
200857.90196291	201728.34974260	202629.75090306
200897.41870563	201758.24901775	202657.52064807
200918.79438769	201819.12758770	202708.78201886
200956.16733143	201843.68449135	202724.80488081
200986.07356760	201873.59483449	202749.37054321
201020.24939884	201907.76566310	202797.42773610
201025.58888551	201915.24933370	202812.38145755
201057.63689405	201945.15477530	202834.80944090
201101.41764483	201990.01367067	202895.68828926
201125.98987413	202003.89712831	202910.63968589
201147.33966886	202038.07207649	202944.81460679

202973.65290871	203913.50610313	204852.28865234
203018.50881099	203938.07288140	204873.64869552
203027.05342394	203957.29637463	204908.89243500
203070.84175313	203987.20192646	204936.66476319
203085.79428266	204024.58025022	204953.74881158
203124.24202123	204060.89357418	204987.92924312
203146.66984313	204086.52585402	205035.99228632
203184.05080168	204128.18019876	205054.15287371
203221.43153824	204136.72158073	205093.66818382
203236.38354077	204189.05199888	205113.95236453
203273.76460011	204221.09853983	205166.28771882
203310.07721392	204259.54062531	205185.51294975
203332.50553553	204272.36133326	205229.29936974
203373.09010353	204293.71833203	205246.38877379
203392.31431999	204334.30667338	205289.10489405
203452.12341068	204374.88712674	205299.79395251
203473.48397828	204406.93154104	205331.83352906
203502.32020419	204419.74267478	205384.16162131
203533.29283133	204477.41770989	205409.79152768
203570.67380717	204495.57529795	205449.31194146
203606.98533282	204538.29785984	205464.26819469
203620.87014343	204551.11111876	205504.84876210
203664.65870936	204594.90353175	205533.69004495
203681.74700622	204616.25697426	205545.43205137
203713.78683296	204663.25294317	205587.08297532
203759.71084011	204668.59265721	205609.52059429
203773.59562403	204705.97347443	205640.49040723
203818.45416883	204748.69211690	205693.89272320
203855.83298472	204781.79971396	205721.65385158
203880.39693866	204814.90764036	205749.43319956

205795.35853660	206047.40766571	206297.32150641
205806.02517024	206066.62696091	206327.22730513
205833.79164754	206104.01332616	206342.18634665
205877.57979239	206131.76745588	206392.38056313
205905.35736551	206165.95895771	206420.13391250
205934.20013287	206179.82884087	206432.94633724
205954.48781689	206219.35444974	206482.08218561
205996.13684035	206239.65446388	

zRi

5000.00000000	3769.97435133	3236.23454297
4918.13643955	3727.24520812	3222.47115477
4836.57739024	3686.69705473	3211.75464391
4762.17243259	3653.84169292	3198.32864264
4682.51818273	3615.67864279	3188.30303350
4613.05788605	3584.79980501	3177.48455436
4544.30108269	3550.63003999	3168.70023058
4471.67720115	3522.42956268	3160.96183519
4404.64283879	3492.99035462	3153.92748347
4332.13791907	3462.03114163	3147.18272286
4274.63016918	3434.94825370	3142.28787896
4221.05786911	3410.43622502	3137.07873784
4153.24826511	3387.94521019	3133.78923878
4103.62951775	3362.00833087	3130.11520712
4051.35687403	3341.07865859	3127.80981224
3993.82580320	3320.02120018	3126.18838090
3942.93895196	3304.33497306	3125.28381738
3897.86428938	3283.98013194	3125.10940929
3857.20872250	3267.07874407	3125.48586008
3808.66055282	3252.79953535	3126.51207199

3128.42050660	3414.39507903	3979.74160760
3130.50045491	3428.48958987	4001.47952475
3133.52874026	3444.78874611	4024.36230055
3137.64178471	3460.96285640	4044.16274780
3141.57748667	3478.65453718	4069.44181226
3146.62193022	3494.53298411	4088.31797091
3151.53355678	3511.06120689	4111.66379854
3156.66130794	3528.25550970	4134.51199675
3163.11950457	3545.67687817	4157.50611558
3170.69566849	3564.65861195	4179.41771571
3178.56230919	3580.29733794	4201.46676069
3185.03582613	3598.82382316	4226.34496644
3193.33681189	3616.18539896	4245.75278078
3202.84891484	3637.44944677	4269.08555309
3212.36614434	3656.61026578	4294.22336153
3221.58871391	3673.13410667	4318.24492746
3232.78255534	3692.17856828	4340.68980376
3242.77663409	3714.78494277	4362.11183555
3252.58579664	3732.74146468	4387.46963406
3265.08855413	3751.33784037	4410.05466612
3276.77622372	3770.06341282	4435.02172818
3289.48976144	3792.44679633	4457.72590191
3302.89324668	3810.97827369	4480.45720578
3314.07853948	3834.18112403	4506.15123896
3326.84476179	3852.49333285	4527.83667020
3342.38511435	3872.43573032	4550.10622737
3354.76608977	3897.15757435	4575.34326844
3370.67959707	3916.85545050	4599.41974169
3385.45318731	3939.26836809	4622.42675252
3397.89578715	3958.12434019	4647.18099683

4674.25939059	5086.67602866	5509.90549173
4697.29372695	5114.02341525	5534.77560820
4720.98586342	5138.51161063	5561.85655178
4742.95393556	5161.74936379	5584.95845207
4768.99750933	5190.29096038	5613.75862249
4791.55153290	5215.26024669	5636.82368055
4817.66702807	5239.11395359	5659.76868318
4843.72873801	5264.69587588	5688.54117948
4866.91454005	5287.36310211	5712.66896818
4890.20855431	5311.17246005	5735.61591507
4914.00267848	5337.83924253	5763.69390389
4939.55612676	5362.81589261	5788.86334687
4963.37952215	5386.60852064	5813.41348880
4989.56537150	5413.25254385	5836.25607107
5016.90157740	5437.55407192	5862.46842023
5038.42451568	5460.18044999	5885.86121343
5065.15187816	5486.16969783	

zAai in degrees

32.35252695	33.74890646	35.18262739
32.47715625	33.89960228	35.29650476
32.60516067	34.01508192	35.43435220
32.72588179	34.14089175	35.55136343
32.86060892	34.28396298	35.68540329
32.98097946	34.41636508	35.80210351
33.10471889	34.53814481	35.92893770
33.23886882	34.65281763	36.06928636
33.36929384	34.79509092	36.19918156
33.51359597	34.91290738	36.32207788
33.63308453	35.04786533	36.44140994

36.58781610	40.39998061	44.17253387
36.71021865	40.52120344	44.30896027
36.84264769	40.65210471	44.42940203
36.94778366	40.76978312	44.55289609
37.09004604	40.88080913	44.67943424
37.21858235	41.01128620	44.80584938
37.33344667	41.15137931	44.94160957
37.47515411	41.28479387	45.05200874
37.60319169	41.38881279	45.18121652
37.71088547	41.51545689	45.30085822
37.85541681	41.65168548	45.44554489
37.97290534	41.78127637	45.57437405
38.11371125	41.90101804	45.68425350
38.23759261	42.04002157	45.80972185
38.36132327	42.15949622	45.95700096
38.48490418	42.27240031	46.07283389
38.62167142	42.41096240	46.19169724
38.73495047	42.53649427	46.31045983
38.87803758	42.66832042	46.45097054
38.98439310	42.80321074	46.56639748
39.13045493	42.91229647	46.70977143
39.24980857	43.03409890	46.82187760
39.37895556	43.17818017	46.94322817
39.51125002	43.29012548	47.09244434
39.63347554	43.43071148	47.21046648
39.75226307	43.55837758	47.34390453
39.88080074	43.66360294	47.45552834
40.01905400	43.80058122	47.58255450
40.12755730	43.91514531	47.70947405
40.25564843	44.04549396	47.84247133

47.95681869	51.25105045	54.56794557
48.10194897	51.39344037	54.69035123
48.20993699	51.51454191	54.82761851
48.34250642	51.63859426	54.95587158
48.47188572	51.75350100	55.07810451
48.60116018	51.88949042	55.21518119
48.72418218	52.00727478	55.34028121
48.84711088	52.14309645	55.45639766
48.98529523	52.27882993	55.59032189
49.09269186	52.39940880	55.71229012
49.22147621	52.51991971	55.84015609
49.35934962	52.64337372	55.97985687
49.49099027	52.77578345	56.09870296
49.61335548	52.89909396	56.24719949
49.72952178	53.03435667	56.36594879
49.86698655	53.17554499	56.48465633
49.98908681	53.28663223	56.63298322
50.12329961	53.42466675	56.75752942
50.24522355	53.53563583	56.87610464
50.36706484	53.67652216	57.02130698
50.50403854	53.80235113	57.15164477
50.61962547	53.92212818	57.27897749
50.73817904	54.06877637	57.39738934
50.87184136	54.19739735	57.53351968
50.99933969	54.31997570	57.65481511
51.12068726	54.45145874	

